

17-00000-0000
118-29-0000
118P
98587

MODELLING DIRECTIONAL SOLIDIFICATION

NAG 8 - 541

Fourth Semi-annual Progress Report

1 March 1987 to 31 August 1987

CLARKSON UNIVERSITY

Potsdam, New York 13676

Principal Investigator:

**Dr. William R. Wilcox
School of Engineering
Center for Advanced Materials Processing
315-268-2336,6446**

Graduate Student Research Assistants:

Mr. Greg Neugebauer, Ph.D. Candidate in Chemical Engineering

Mr. Ross Gray, Ph.D. Candidate in Chemical Engineering

Mr. Mohsen Banan, Ph.D. Candidate in Materials Processing

**(NASA-CR-181337) MODELLING DIRECTIONAL
SOLIDIFICATION Semiannual Progress Report, 1
Mar. - 31 Aug. 1987 (Clarkson Coll. of
Technology) 118 p Avail: NTIS HC A06/MF
A01**

N87-28751

**Unclas
0098587**

CSCI 22A G3/29

SUMMARY

Goals and objectives

The longrange goal of this program is to develop an improved understanding of phenomena of importance to directional solidification, to enable explanation and prediction of differences in behavior between solidification on Earth and in space. Currently emphasis is on experimentally determining the influence of convection and freezing rate fluctuations on compositional homogeneity and crystalline perfection. Greg Neugebauer seeks to correlate heater temperature profiles, buoyancy - driven convection, and doping inhomogeneties using naphthalene doped with anthracene. Ross Gray aims to determine the influence of spin-up / spin-down on compositional homogeneity and microstructure of indium gallium antimonide. Mohsen Banan intends to determine the effect of imposed melting - freezing cycles on indium gallium antimonide. The combined work of Ross Gray and Mohsen Banan should clarify the mechanism behind the increase of grain size caused by using spin-up / spin-down in directional solidification of mercury cadmium telluride.

Progress and plans

No personnel changes occurred since the previous semi-annual progress report. Ross Gray passed his Ph.D. qualifying examination. He will serve as an instructor for the Chemical Engineering Department this academic year. While will not be paid from this grant, he will continue working on his research part time. Mohsen Banan has built his experimental apparatus and begun developing his techniques. He is preparing a research proposal for his Ph.D. qualifying examination, which will be taken before the end of this calendar year.

Greg Neugebauer's paper on "Convection in the Vertical Bridgman - Stockbarger Technique" received a favorable review from the Journal of Crystal Growth, with only minor changes required. Ross Gray submitted a paper on "Diffusional Decay of Striations" to JCG. A talk on "Convection in the Bridgman - Stockbarger Technique" was given at Queens University, the Gordon Conference on Crystal Growth, and the Santa Barbara Research Center. Papers on "Decay of Compositional Striations" and "Buoyancy - driven Convection in the Vertical Bridgman - Stockbarger Technique" were presented at the American Conference on Crystal Growth 7 in Monterey.

Greg Neugebauer deveoped techniques for reproducible growth of clear crystals of naphthalene from melts containing 0.1% anthracene. These crystals are free of entrapped gas and contain few stress - induced fractures. He developed techniques for removing the crystals from ampoules and sectioning them, and for accurately measuring cross - sectional variations of anthracene concentration in the naphthalene matrix. All necessary equipment and supplies have been acquired. In the next 6 months experiments will be run in the thermally stable configuration to minimize convection. Convection will be observed with streak photography of suspended particles, the interface shape will be determined by q quenching, and the anthracene concentration will be determined at many locations by UV absorption and fluorescence.

Ross Gray sealed indium, gallium and antimony together in ampoules. The metals were melted, mixed and slowly solidified in a vertical Bridgman - Stockbarger apparatus with spin-up / spin-down (accelerated crucible rotation technique). Difficulties were encountered with power failures during the lengthy runs. A method of measuring the

temperature gradient in the melt was developed. During the next six months the temperature gradient and interface shape will be determined for different heater - cooler settings, so that subsequent runs can be made without constitutional supercooling and with a slightly convex interface shape.

Mohsen Banan intends to use Peltier Interface Demarcation to cause periodic remelting during directional solidification of indium antimonide - gallium antimonide alloys. During the last 6 months the complete apparatus was constructed. Techniques were developed for fabricating ampoules containing PID electrodes. During the next 6 months he will perform solidification runs.

CONTENTS

Summary	i
I. Influence of convection on component segregation in the Bridgman - Stockbarger technique.	1
Summary	1
A. Introduction	1
B. Progress	2
C. Plans	4
D. References	6
II. Influence of spin-up / spin-down on compositional homogeneity and perfection of directionally solidified indium gallium antimonide.	11
Summary	11
A. Introduction	11
B. Progress	12
C. Plans	12
III. Influence of imposed freezing rate fluctuations on the microstructure and compositional homogeneity of indium gallium antimonide.	13
Summary	13
A. Introduction	13
B. Progress and methods	16
C. Plans	18
D. References	18
Appendix A. Influence of spin-up / spin-down on the compositional homogeneity and crystallographic perfection of alloy semiconductors	
Appendix B. Diffusional decay of striations	

I. INFLUENCE OF CONVECTION ON COMPONENT SEGREGATION IN THE BRIDGMAN - STOCKBARGER TECHNIQUE

Greg Neugebauer

Summary

The goal of this project is to determine the relationships between longitudinal and circumferential temperature profiles in the furnace, convection patterns, and cross sectional variations in impurity doping. This is being accomplished by fabrication of special furnaces, light streak photography, solidification of naphthalene doped with anthracene, and microchemical analysis for anthracene concentration throughout the resulting ingots.

Thus far the following have been achieved:

1. Techniques were developed for reproducible growth of clear crystals of naphthalene doped with approximately 0.1% anthracene. These crystals are free of entrapped gas and contain few stress - induced fractures.
2. Techniques were developed for removing the crystals from ampoules and sectioning them.
3. A technique was developed for accurately measuring cross - sectional variations of anthracene concentration in the naphthalene matrix.
4. All necessary equipment and supplies have been acquired.
5. The referee for the Journal of Crystal Growth has recommended publication of the paper "Convection In The Bridgman-Stockbarger Technique" upon completion of requested changes.

During the next 6 months experiments will be run in the thermally stable configuration, so as to produce gentle convection. The convection will be measured by streak photography of floating particles. The interface shape will be determined by quenching the melt after about half of it has frozen. The anthracene concentration will be determined at many locations throughout the ingot.

I.A. Introduction

Bridgman's original technique for growing single crystals consisted of a single furnace out of which a cylindrical, pointed-bottom container holding the charge was lowered. The Bridgman-Stockbarger technique was created when Stockbarger added a second furnace which functioned as a cooler. He separated the upper and lower furnaces with a polished platinum thermal screen designed to promote a steep axial temperature gradient (1-3). This method of directional solidification is used today to grow single crystals of metals, organics, dielectric oxides, fluorides, sulfides, and halides (3).

The need in recent years to produce more homogeneous crystals has made directional solidification a topic of intensive research. Theoretical studies were made on the

effect of heat transfer on the shape of the melt / solid interface, an important parameter in controlling thermal stress, grain selection, component homogeneity, etc. (4,5).

Most models have assumed that heat transfer within the melt occurs only by conduction. While this may be a valid assumption for low Prandtl number fluids, the effect of convection on compositional homogeneity is significant for all melts. The microscopic distribution of components at the interface may be extremely sensitive to small changes in convective flow patterns (6). Because the response of most electronic devices is strongly related to their composition, convective transport in melt growth systems has been actively investigated in recent years.

The segregation created by buoyancy - driven convection can be largely eliminated by growth in space, although under some conditions the residual accelerations may cause enough convection to cause compositional variations. Reviewers have often suggested that it may be possible to eliminate the effects of buoyancy - driven convection on earth. While it seems likely that convection in metallic melts can be reduced to any desired level by the use of a sufficiently strong magnetic field, this is not possible for non - conducting melts.

Recently we found (7) that the temperature profile of the heater in the Bridgman - Stockbarger configuration can be adjusted so as to nearly eliminate convection near the solid - liquid interface of organic materials. The convective flow field was usually asymmetrical. For the vertically stabilized condition (temperature increasing with height), very gentle convection, on the order of 10 microns / sec, can persist. This very slow convection was difficult to resolve, especially near the interface. If convection this slow is always present in the vertically stabilized condition, component segregation is expected to be large when the flow velocity is of the same order of magnitude as the crystal growth velocity, which is likely to be common.

The objective of the current research is to observe the convective flow field and measure the segregation it induces in the crystal for a series of convective flow regimes. Of particular interest is the gentle convection associated with the vertically stabilized condition, since this is expected to produce the greatest doping inhomogeneity. The effect of the crystal's interfacial curvature in the vertically stabilized condition will be investigated. Even under diffusion controlled conditions in a symmetrical temperature field, large radial variations in doping are expected if the interface is either very convex or very concave (6). The variation of doping produced with vigorous convection also will be examined.

When a short booster heater is added between the main heater and the cooler, an axial temperature gradient can be created in the melt near the interface that promotes buoyancy driven convection. It is known that this changes the axial doping profile completely, but it will be interesting to see how a well - stirred melt changes the cross - sectional doping patterns in the crystal.

I.B. Progress

In this project the vertical Bridgman-Stockbarger technique is being used to grow naphthalene crystals doped with anthracene. Two photographs of the set-up are shown in Figure I.1. The heater is constructed of a polycarbonate tube around which is wound nichrome resistance heating wire. Below the main heater is a short booster heater. Above the main heater is a short heater designed to control temperature roll-off at the top of

the furnace. An annular Pyrex jacket serves as the cooler. Between the furnace and the cooler is a thin layer of insulation. The pedestal upon which the sample ampoule rests can be seen emerging from the bottom of the cooler.

The diameter of the ampoule is 16 mm. It is constricted to approximately 5 mm ID for 1 to 2 cm near its bottom. As the sample is solidified, grains whose growth directions are non-parallel to the ampoule's translation are grown out in the constriction. The ingots produced by this method appeared to be single crystals; no grain boundaries were observed. The ingots were also "crystal clear." Rarely was an ingot produced that was clearly composed of two grains. In those cases, an opaque grain boundary that runs parallel to the ampoule wall along the entire length of the ingot was easily distinguished.

Crystals were grown free of entrapped gas bubbles and stress-induced fractures. Gases were removed from the naphthalene by applying a vacuum of approximately 25 mm Hg to the melted naphthalene prior to solidification. The temperature gradient near the interface was determined by measuring the temperature at the outer wall of the sample ampoule with a moveable thermocouple. A temperature gradient of approximately 15 to 20 °C / cm with a growth rate of 1.5 microns / sec was typically employed. A larger temperature gradient could not be applied because thermal stresses in the crystal caused it to break into several pieces while still in the ampoule.

In order to remove the crystal from the ampoule the ends of the ampoule are first removed by scratching rings around the ampoule and touching the rings with a hot glass rod. The remaining ampoule is held vertically and heat is applied with a hot air gun, causing the crystal to slide out of the ampoule. The crystal is then cleaved with a sharp blade. If the cleavage plane is not oriented properly with the plane in the crystal that is to be analyzed (normally perpendicular to the ampoule axis), the cleaved surface is shaved to the desired direction using the blade.

To measure cross - sectional variations in doping, samples must be taken from the surface of the cross sectional slice. Approximately 0.200 mg is removed from each desired location on the surface of the slice by lightly scratching it with a small razor blade. With care, 6 to 8 nearly equally spaced samples can be obtained across one diameter. The exact radial location of the sample is determined by measuring the location of the scratch on surface afterwards. The material removed from the surface is dissolved in 5 ml of 2,2,4-trimethylpentane (iso-octane), and its composition is determined using fluorescence spectroscopy.

Fluorescence spectroscopy works very well for this system because naphthalene and anthracene fluoresce very strongly. Naphthalene absorbs and fluoresces entirely in the UV region, while anthracene absorbs in the UV and fluoresces in the visible region. The ultraviolet absorption spectra of anthracene and naphthalene in iso-octane are shown in Figures I.2 and I.3. Figure I.2 shows that anthracene has an absorption peak at 365 nm.

When excited at 365 nm, anthracene has a maximum in the fluorescence spectrum at 400 nm.

(The emission spectra are not shown.) Figure I.3 shows that naphthalene has a broad absorption peak at 275 nm. When excited at 275 nm, naphthalene has a maximum in the fluorescence spectrum at 325 nm.

The procedure for determining the relative distribution of anthracene in the crystal is straightforward. A series of naphthalene and anthracene standards are prepared and fluorescence vs. concentration curves are drawn for each. The fluorescence of the samples dissolved in iso-octane is measured at 325 nm and 400 nm. Under these conditions, the measured fluorescence of naphthalene and anthracene is such that it is the

same as if they were both dissolved in separate solutions. Therefore, the concentration of each in the iso-octane is found directly from the fluorescence vs. concentration curves for the pure standards.

The distribution of the anthracene in the crystal can be characterized in terms of the ratio of its concentration in the iso-octane solution to the concentration of naphthalene. Alternatively its mass fraction in the crystal can be calculated. Note that 0.2 mg of naphthalene dissolved in 5 ml of iso-octane produces a solution that is on the order of 10 ppmw naphthalene. Figure I.4 is a plot of the fluorescence of anthracene vs. its concentration in the presence of 10 ppm naphthalene. Note that the data in this figure are linear with a correlation coefficient of 0.9999.

Comparison of Figures I.2 and I.3 indicates that there are constraints (although slight) on the usefulness on this spectroscopic procedure. Figure I.2 shows that anthracene absorbs at 325 nm, the wavelength at which the emission from the naphthalene is being monitored; i.e. anthracene quenches the fluorescence of naphthalene. If the concentration of anthracene is on the same order as that of naphthalene, no fluorescence of naphthalene would be observed and its concentration could not be determined. However, in the present experiments this error is insignificant because the concentration of anthracene is approximately 1000 times less than that of naphthalene (when a dopant level of 0.1% is used). The absorbance at 325 nm by the anthracene is negligible because there isn't enough anthracene present to absorb a significant amount of the light emitted by naphthalene. Also, Figure I.2 shows that the molar absorptivity of anthracene is very low at this wavelength. In fact, if the dopant level is changed by 100%, the error induced in the concentration of naphthalene is less than 1%.

The experimental error associated with the above analytical procedure is less than 2.8%. Therefore concentration variations larger than 2.8% can be determined. The experimental error associated with this technique can be reduced further by repetition of measurements, by using higher purity iso-octane, and by storing the concentration standards in glass. In the preliminary work described above, the concentration standards were stored in Nalgene bottles. This caused significant contamination problems. For this reason glass storage bottles were ordered last month.

I.C. Plans

First on the agenda for the next six months is to finish the corrections to the paper "Convection In The Bridgman-Stockbarger Technique" for the Journal of Crystal Growth.

Investigations of doping inhomogeneity will be made on anthracene - doped naphthalene solidified in the vertically stabilized condition. Doping variations will be examined for crystals solidified under both thermally symmetrical and asymmetrical conditions. From this we hope to find to what degree the thermal symmetry of the Bridgman - Stockbarger furnace causes cross - sectional variations in doping. The effects of interfacial curvature, both convex and concave, for the vertically stabilized condition will be examined as well.

In order to determine the convection pattern and its magnitude, when about half of the melt has been solidified tracer particles will be added to the melt and a time exposure photograph taken with laser slit illumination as in (7). Immediately after the photo is taken the ampoule will be rapidly removed from the heater allowing the melt to solidify dendritically. In this way, the location of the interface at the time the convection was photographed will be clearly demarcated.

After studying convection and segregation under thermally stable conditions, doping inhomogeneity under well mixed conditions will be investigated. The booster heater will be used to create a destabilizing temperature gradient near the interface. (This creates vigorous convection throughout the entire melt.) Forced convection may be generated by a transient rotation of the ampoule as well. Since rotating the ampoule should produce a more symmetrical temperature field at the ampoule's wall, it will be interesting to compare the usefulness of ampoule rotation with a destabilizing temperature gradient in producing more homogeneous crystals.

I.D. References

1. D. C. Stockbarger, Rev. Sci. Instr., 7, 133-136 (1939).
2. H. Potts, M.S. Thesis, Clarkson University, Potsdam, NY (1984).
3. A. A. Chernov, Modern Crystallography III, Springer-Verlag, New York, 429 (1984).
4. C. E. Chang and W. R. Wilcox, J. Crystal Growth, 21, 134-140 (1974).
5. T. Fu and W. R. Wilcox, J. Crystal Growth, 48, 416-424 (1980).
6. C. J. Chang and R. A. Brown, J. Crystal Growth, 63, 343-364 (1983).
7. G. Neugebauer, M.S. Thesis, Clarkson University, Potsdam, NY (1986).

ORIGINAL PAGE IS
OF POOR QUALITY

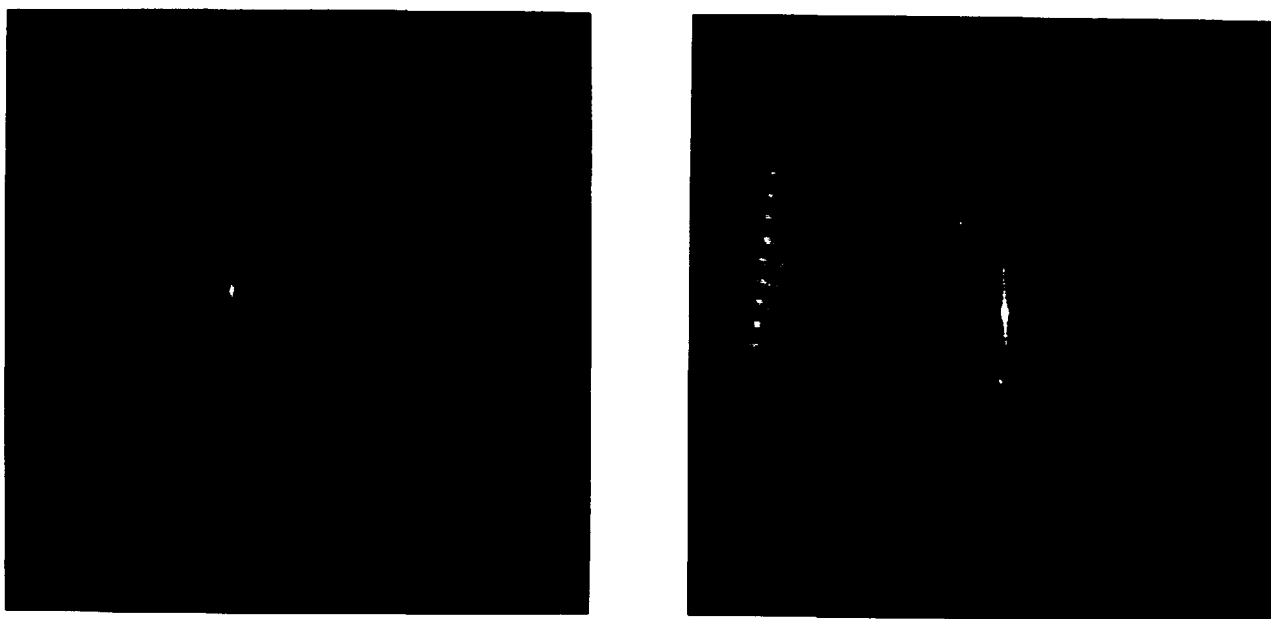


Figure I.1. Photographs of the Bridgman - Stockbarger apparatus. On top is a clear three zone heater. Beneath the heater is an annular circulating cooler. Between the heater and the cooler is a thin layer of insulation.

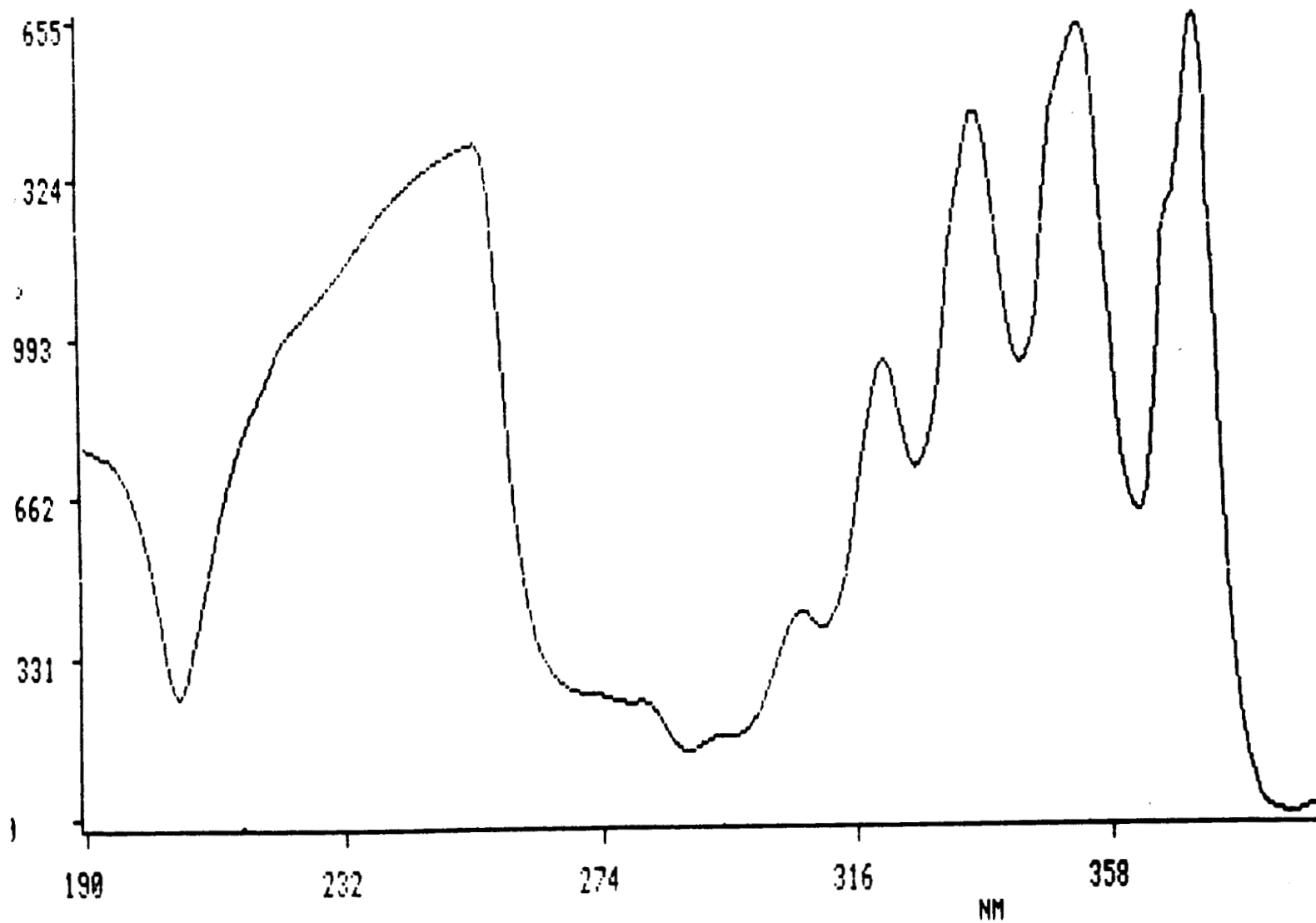


Figure 1.2. Ultraviolet absorption spectrum of anthracene dissolved in iso-octane.

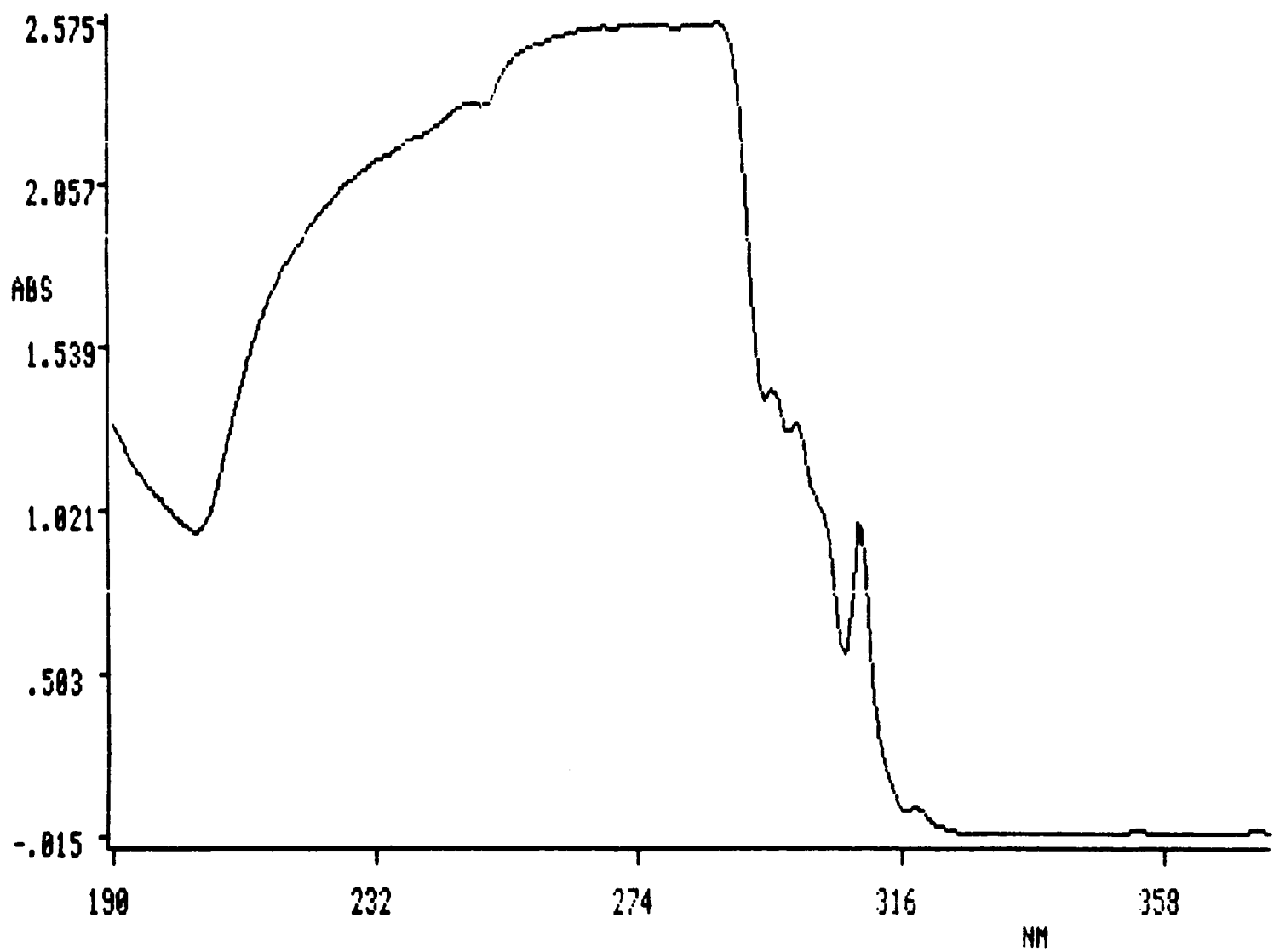


Figure I.3. Ultraviolet absorption spectrum of naphthalene dissolved in iso-octane.

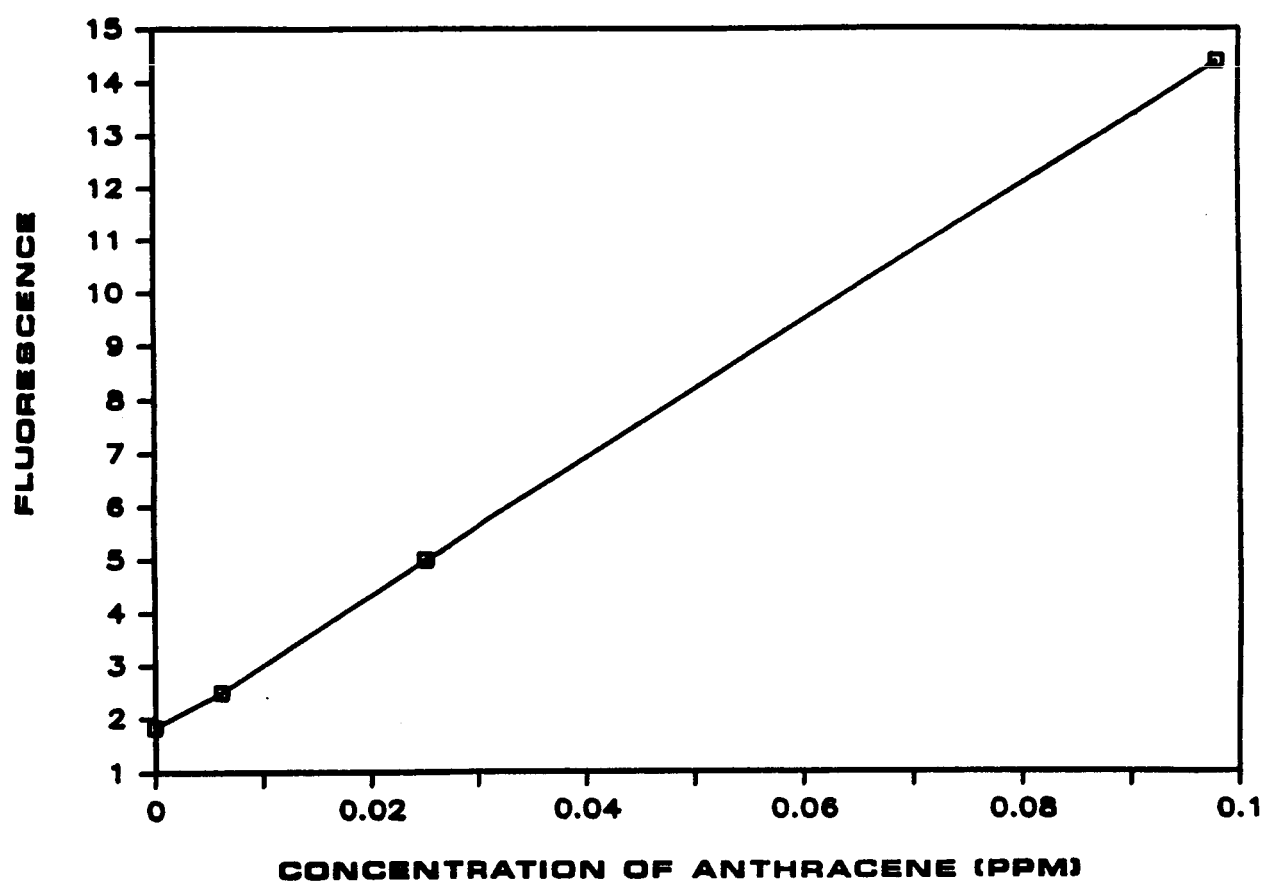


Figure I.4. Fluorescence of anthracene vs. its concentration with a naphthalene concentration of 10 ppm.

II. INFLUENCE OF SPIN-UP / SPIN-DOWN ON COMPOSITIONAL HOMOGENEITY AND PERFECTION OF DIRECTIONALLY SOLIDIFIED

INDIUM GALLIUM ANTIMONIDE

Ross Gray

Summary

Appendix A is the research proposal prepared for Ross Gray's Ph.D. qualifying examination, which he passed during this reporting period. It includes a review of the literature on the effect of solidification conditions on compositional homogeneity, twinning, grain boundary formation and dislocations, especially in compound semiconductors.

Appendix B is a manuscript resulting from a theoretical study of the influence of solid state diffusion on the decay of compositional striations formed during solidification. Under many conditions striations decay to negligible magnitude long before the crystal cools to room temperature and is examined.

Indium, gallium and antimony have been sealed together in ampoules, melted, mixed and slowly solidified in a vertical Bridgman - Stockbarger apparatus with spin-up / spin-down (accelerated crucible rotation technique). Difficulties have been encountered with power failures during the lengthy runs. A method of measuring the temperature gradient in the melt was developed.

II.A. Introduction

The planned research, including background and literature review, is covered in detail in Appendix A. The most pertinent observation is that made by workers at Mullard in Southampton, England. Use of spin-up / spin-down in directional solidification of mercury cadmium telluride not only produced homogeneous ingots, but also unexpectedly increased the grain size. A primary objective of the present research is to determine the mechanism for this phenomenon. Indium gallium antimonide was chosen as a model substance, in that it has a phase diagram similar to mercury cadmium telluride, exhibits the same sort of solidification problems (twinning and grain boundary formation), and yet is non-volatile. Thus equipment has been built and techniques developed for directionally solidifying indium gallium antimonide with spin-up / spin-down. Correlations will be sought between the solidification conditions, compositional homogeneity and crystal defects (twins, grain boundaries and possibly dislocations).

Recent research by Larrousse at Clarkson showed that spin-up / spin-down leads to large fluctuations in freezing rate and segregation. In fact meltback is expected during each spin-up / spin-down cycle. It may be that this periodic melting and freezing enhances grain selection and elimination of twins in solidification of mercury cadmium telluride at Mullard. To differentiate between the stirring effects of spin-up / spin-down and remelting effects, another doctoral student is planning experiments that will produce periodic melting and freezing without added convection. This will be accomplished by passing large currents through the material during solidification, as described in detail in

Section III.

II.B. Progress

A research proposal on the compositional homogeneity and crystallographic perfection of alloy semiconductors was written. A copy of the proposal is included in this report as Appendix A. The PhD qualifying examination was taken and passed.

After repeated attempts, a method of measuring the temperature gradient inside a melt of $\text{In}_x\text{Ga}_{1-x}\text{Sb}$ was devised. A thin K-type thermocouple probe is placed in a two-hole ceramic insulator and this is inserted into a quartz capillary that is fused in the bottom of the growth ampoule. This allows the measurement of temperature at a height of 4 cm above the bottom of the ampoule, while it is being translated through the heater - cooler assembly. A temperature gradient measurement is currently being taken with the heater temperature at 850°C , the cooler at 10°C , and the translation rate at 4 mm / day.

In addition to the work reported previously on analysis of solid state diffusional decay of striations, an analytical solution was obtained for an isothermal ingot. This agrees well with the prior numerical calculations for the initial portion of the ingot, and is conservative in predicting survival of striations to room temperature. A paper entitled "Diffusional Decay of Striations" by Gray, Larrousse and Wilcox was submitted to the Journal of Crystal Growth. A copy of the paper is enclosed in this report as Appendix B.

II.C. Plans

Over the next six months, temperature gradient measurements with different heater and cooler temperature combinations will be taken until a proper gradient for the avoidance of constitutional supercooling is achieved. Also, the interface should lie in the upper part of the insulating region or the lower furnace region so that a slightly convex interface is obtained. The furnace will be shut down for a time sufficient to cause a demarcation of the interface in a separate experiment. Once the proper heater and cooler temperatures are chosen, the set of experiments in Table 1 of the research proposal (Appendix A) will be started.

III. INFLUENCE OF IMPOSED FREEZING RATE FLUCTUATIONS ON THE MICROSTRUCTURE AND COMPOSITIONAL HOMOGENEITY OF INDIUM GALLIUM ANTIMONIDE

Mohsen Banan

Summary

The objective of this project is to determine the influence of imposed freezing rate fluctuations on compositional homogeneity, twinning, and grain size of directionally solidified indium gallium antimonide. This research will complement that described in Section II above, to enable us to determine the mechanism by which spin-up / spin-down reduces polycrystallinity in solidification of mercury cadmium telluride. Passage of current pulses through the material during solidification will produce alternate melting - freezing cycles without significantly influencing convection in the melt.

A literature review is nearly complete. A research proposal is being written in preparation for the Ph.D. qualifying examination. A Bridgman - Stockbarger furnace and a Peltier Interface Demarcation apparatus were constructed. Techniques were developed for fabricating ampoules containing PID electrodes.

III.A. Introduction

Solid solutions of semiconducting III-V and II-VI systems, such as indium gallium antimonide and mercury cadmium telluride, exhibit the advantage of composition - dependent properties. By varying composition, the material's properties can be selected to suit different purposes and applications, such as optoelectronic and infrared sensing devices. For example, a solid solution of indium antimonide and gallium antimonide is a promising material for photodetectors, Gunn devices, and three level oscillators (1-4). However, bulk growth of these crystals has been mostly limited to exploratory investigation due to two basic problems associated with alloy growth, i.e. compositional inhomogeneity and polycrystallinity. The origins of these problems are not yet completely understood despite extensive research done in this field.

When concentrated alloy melts are frozen, extensive segregation readily occurs, commonly resulting in an inhomogeneous solid and morphological breakdown due to constitutional supercooling (5-7). Such growth behavior may be the cause of twin and grain formation, inclusions, dislocations, etc. While constitutional supercooling may be avoided by use of a low growth rate and a large temperature gradient at the freezing interface, twinning and polycrystallinity persist nonetheless. It has been speculated that freezing rate fluctuations may lead to momentary constitutional supercooling with accompanying nucleation of twins and grains even when the average freezing rate is sufficiently low that constitutional supercooling is not expected.

Buoyancy - induced convection is always present in the melt during solidification on Earth because of unavoidable thermal and compositional gradients. This convection often oscillates or fluctuates, causing variations in the rate of crystal growth, compositional variations, and perhaps nucleating grains and twins.

To study the effect of microgravity on microstructure, InSb-GaSb ingots were directionally solidified on the Skylab III and IV missions (8-10). The numbers of grain and twin boundaries were substantially reduced in the space - processed crystals as compared with corresponding ingots solidified on earth under otherwise identical conditions. A similar reduction in the number of twins was observed in InSb-GaSb solidified with a magnetic field applied to the melt to inhibit free convection (11).

Mechanical twins are formed in some crystal systems when stress causes the crystal to dislocate through a distance which is not a multiple of the unit cell dimensions. Thermal stress during solidification might be responsible for some twinning, since high temperature gradients and low freezing rates (i.e. solid remains at high temperature for a long time) are needed to avoid constitutional supercooling. Stress - annealing of indium gallium antimonide ingots resulted in a slight modification in the geometry of grains and twins, but no change in their numbers (12). These observations suggest that the presence of stress during solidification of these alloys probably does not cause generation of twins or grains, but may cause significant modification of their shapes.

As noted in Section II above, the effect of ACRT on the compositional homogeneity and crystallographic perfection of $\text{In}_x\text{Ga}_{1-x}\text{Sb}$ ingots is now being studied in our laboratory (13).

The goal of the present project is to determine the effect of controlled freezing rate fluctuations on the formation and annihilation of twins and grains in indium gallium antimonide crystals directionally solidified by the vertical Bridgman-Stockbarger method. The freezing rate will be varied rapidly by a technique commonly called Peltier Interface Demarcation (PID), because it was developed for revealing the shape and position of the solid - liquid interface at selected time intervals.

The PID technique (14) utilizes a current pulse passing through a directionally solidified crystal to create a rapid thermal perturbation at the solid - liquid interface due to the Peltier effect (15). Some joule heating of the solid and liquid also occurs. These combined thermal perturbations cause a rapid change in freezing rate and may even lead to remelting. If a current pulse is applied periodically the freezing rate varies periodically. Alternate freezing and melting can be achieved as well.

The periodic melting and regrowth during crystal growth have been shown to improve the quality of the resultant crystals. For example, periodic vapor phase etching and regrowth has resulted in a higher quality crystals of Fe_2O_3 (16) and mercuric iodide (17).

The dislocation density of GaP was reduced by a factor of 3 as a result of one meltback cycle during LPE (18). Periodic melting and regrowth greatly accelerated grain selection during solidification of films of salol under the microscope (18).

III.A.1. Background on Peltier effect

The Peltier effect refers to liberation or consumption of heat at a boundary between two conductors when electric current is passed through the boundary. Reversal of current direction causes heat liberation to become heat consumption and vice versa. The solid and liquid phases of a given material act as different conductors, so that when current is passed through a solid - liquid interface the Peltier effect occurs. PID has unique advantages for interface control in crystal growth:

- (i) There is no time lag between stimulus and response, because the heat is produced directly at the interface.

(ii) The effect is reversed by reversing the direction of the applied current.

The Peltier heat, absorbed or evolved at the interface is given by:

$$Q = P I \quad (1)$$

where P is the Peltier coefficient and I is the current density. The Peltier effect is related to other thermoelectric effects, i.e. Joule, Seebeck, and Thomson effects, and they can occur simultaneously (15).

Ioffe (20) was one of the first to draw attention to the existence of the Peltier heat between a solid metal and its own melt, and suggested its use in solidification phenomena such as zone refining and crystal growth. An expression was derived (21,22) for the interface velocity due to the Peltier effect the heat balance at the interface:

$$V = (PI + (K_s G_s - K_l G_l))/H \quad (2)$$

where K_s and K_l are the thermal conductivities of the solid and melt, respectively, G_s and G_l are the thermal gradients at the interface in the solid and melt, H is the latent heat of fusion per unit volume, P is the Peltier coefficient, and I is the current density. Equation (1) shows that appropriate changes in the current density can cause the interface to accelerate, stop, or reverse direction. Corresponding fluctuations in the instantaneous growth rate are incorporated in the growing crystal as impurity striations (14).

Peltier interface demarcation lines (intercepts of the periodically delineated interface with a plane parallel to the growth axis) can be used as:

- (i) "Rate striations" for determination of microscopic growth rate.
- (ii) Locators for the identification of simultaneously grown areas in the core and off-core regions.
- (iii) Time "reference markers" for the correlation of growth and segregation behavior vs. time in directionally solidified semiconductor crystals (23-27).

The Peltier effect has been used in liquid phase electro-epitaxial growth (28,29). In this method, the two main mechanisms responsible for crystal growth are:

- (i) Peltier cooling at the substrate-solution interface leads to a change in the interface temperature, which supercools the solution in direct proximity to the substrate.
- (ii) Electromigration of solute towards the substrate results in a steady state solute flux which sustains growth.

The Peltier effect was also used in experiments aimed at gaining an improved understanding of the atomic mechanism of solidification (30), based upon the relationship between the microscopic growth velocity and the undercooling at the interface. It was used to form p-n and more complex junctions (21,31) by controlling solute segregation through varying the growth rate.

III.B. Progress

A literature search was performed. A research proposal is being written in preparation for the doctoral qualifying examination. The equipment and materials required for growth of crystals were purchased. A vertical Bridgman - Stockbarger furnace was designed and constructed. A PID growth ampoule was designed and fabricated.

III.B.1. Experimental Apparatus

The experimental set-up consists of the vertical Bridgman - Stockbarger (VBS) apparatus and the PID system shown in Figure III.1. The translation unit is a model 202 zone refiner manufactured by Crystal Specialties of Oregon. It is held in a vertical position and was already available in our laboratory. Modifications, i.e. replacing pulleys and belts, were performed to achieve a translation rate of 4 mm/day to enable us to avoid constitutional supercooling in the InSb-GaSb system (11).

A two zone VBS furnace was designed and constructed as shown in Figure III.2. It consists of a hot zone and a cold zone separated by an insulating layer to achieve a more planar interface (32). The hot zone is made of Kanthal heating element embedded in a Fibrothal tubular insulation. The heating element is sandwiched between two zirconia insulation disks and copper sheets. For better thermal insulation, a robok insulating blanket is wrapped around the heating element. The complete unit is surrounded by an aluminum cover for better protection. A quartz tubing, 20 mm. I.D., 25 mm. O.D., and 6.5 in. long, is used as the furnace liner. The diameter of the opening for the ampoule in the furnace is 1.5 cm. Several holes are made on top of the furnace for insertion of thermocouples. The cold zone is a copper double-pipe heat exchanger. It is connected to a Lauda thermostatted water-bath for allow coolant circulation.

A k-type thermocouple is located in the furnace between the heating element and the liner. It is connected to an Omega model 6000 microprocessor - based on - off temperature controller. The output voltage from the controller is stepped down to a proper voltage using a Powerstat variable autotransformer, and then connected to the heating element. With fine tuning of the controller, the temperature of the furnace can be controlled to within 1 C.

The Peltier Interface Demarcation system consists of a pulse generator, strip chart recorder, and the PID growth ampoule. A Keithley model 228 voltage-current source is utilized as a pulse generator. This unit features a maximum output current of 10 A / 100 W with a dwell time ranging from 25 ms to 1000 s. Up to 100 channels can be programmed for current pulses of various amplitudes and frequencies. A strip-chart recorder will be used to monitor and record the voltage across the electrodes during the growth period.

For designing the PID growth ampoule, the following concepts were considered:

- (i) The ampoule should be vacuum-sealed.
- (ii) The electrode materials should have high electrical conductivity and high melting temperature, and exhibit no chemical reaction with the growth materials.

After a literature search, two materials were selected for the electrode lead; molybdenum and tungsten. Corrosion and solubility tests were performed on these materials. A piece Mo or W wire was placed in a vacuum-sealed quartz ampoule containing

the growth materials, $\text{In}_x\text{Ga}_{1-x}\text{Sb}$ ($x=.2$). The ampoule was attached to a motor and placed inside a furnace which was set at 900 C. The growth materials were homogenized by rotating the ampoule in a reciprocating fashion. After 72 hours, ingots were rapidly solidified by removing the ampoule from the furnace. The ingots were removed by breaking the quartz ampoules, and cut radially using a diamond saw. The samples were cast in an epoxy resin, lapped, and polished to reveal the cross section of embedded wires. The prepared samples were examined under an optical microscope equipped with a video camera connected to a TV monitor. Figures III.3 and III.4 show photomicrographs of the cross sections of embedded wires. The diameters of the wires were measured before and after the tests. No drastic change was observed either case.

Figures III.5 and 6 are schematic diagrams of PID growth ampoules. The ampoules are made of quartz tubing, 7 mm I.D., 9 mm O.D., and 20 in. total length. The electrodes are made of tungsten or molybdenum, 1 mm in diameter, inserted through graphite cylinders. The graphite is used for better material - electrode contact. The electrodes are passed through the quartz capillary tubing, 1 mm ID, 6 mm OD, and 2 cm long, at both ends of the ampoules. This is done to secure the position of the electrode leads and to minimize the openings at the end of ampoule.

To seal the ampoule, two designs were considered. In design PID-GA1, a Pyrex graded seal quartz (Corning Glass), 7 mm ID, 9 mm OD, 2 in. long, is fused to the quartz capillaries. (Pyrex and tungsten are supposed to make a good seal (33).) In design PID-GA2, a quartz cup, 7 mm ID, 9 mm OD, and 2 cm long, is fused to the capillary tubing. The cups are filled with high temperature ceramic cement (Cerabond 556 manufactured by Aremco Products) of 1% porosity. The cement is allowed to cure at 100 C for 2 hours. The growth ampoules also feature access for growth materials and tubing connection to the vacuum line. Schematic diagrams of loaded and sealed ampoules are shown in Figures III.5 and 6.

Several prototypes of PID-GA2 were fabricated. A vacuum of 10^{-3} torr was achieved. The Pyrex graded seal quartz has not yet been received. The aluminum ampoule holder shown in Figure III.7 was designed and fabricated. It features sections movable in both horizontal and longitudinal directions for the exact alignment of the growth ampoule with the furnace liner. The ampoule holder is attached to moving platform of the translation unit.

III.B.2. Experimental Procedure

Following are the general tasks which will be performed during each growth run. The growth materials (20 % or 40 % InSb initial melt composition) will be homogenized and transferred into a precleaned PID growth ampoule. The ampoule will be sealed under a vacuum of 10^{-3} torr. The loaded ampoule will be attached to the ampoule holder and placed inside the VBS furnace. The electrode leads will be connected to the pulse generator and the strip chart recorder.

By programming the temperature controller, the furnace temperature will be gradually increased up to the required value (melting temperature). The pulse generator will be programmed for a current pulse with proper amplitude and frequency. The translation unit controller will be set on desired lowering rate (4 mm/day or 8 mm/day). The growth will be initiated by translating the ampoule from the hot zone to the cold zone. The pulsing will be started after solidification of the crystal for about 1 cm. The amplitude and duration of pulses will be monitored and recorded on a strip-chart recorder for future correlation between the growth observations and pulsing effect.

After termination of the growth run, the furnace will be allowed to cool down slowly to avoid any thermal shock. After removing the ingot from the ampoule, it will be cut axially and radially into several pieces. These samples will be cast in epoxy resin, lapped, and polished. The polished samples will be etched to reveal the microstructure or the striations. The microstructure will be examined under an optical microscope and a scanning electron microscope. A compositional analysis of the ingots will be also performed using EDEX.

III.C. Plans

The research proposal will be completed and the Ph.D. qualifying exam will be taken. The temperature profile of the furnace will be determined by inserting a k-type thermocouple inside the furnace liner and measuring the temperature at different positions. The translation unit will be calibrated for growth rates of 4 mm/day and 8 mm/day. The PID growth ampoules will be optimized for a firm vacuum seal. An ampoule design (i.e. thermocouple electrode arrangements) will be considered and fabricated for measurement of the thermal transients at the solid/melt interface during periodic growth.

The first $\text{In}_x\text{Ga}_{1-x}\text{Sb}$ ($x = 0.2$) ingot will be grown at an average rate of 8 mm/day and current pulses of 5 A with 30 min. off and 30 s on periods.

III.D. References

1. T.S. Plaskett and J.F. Woods, J. Crystal Growth 11, 341 (1971).
2. A. Joullies, J. Allegre, and G. Bougnot, Mat. Res. Bull. 7, 1101 (1972).
3. J.C. McGoody, M.R. Lorenz, and T.S. Plaskett, Solid State Comm. 7, 901 (1961).
4. G. Hilsum, H.D. Rees, Electron. Lett. -6, 277 (1970).
5. W.A. Tiller, K.A. Jackson, J.W. Rutter and B. Chalmers, Acta Met. 1, 428 (1953).
6. J.W. Rutter and B. Chalmers, Can. J. Phys. 31, 15 (1953).
7. W.W. Mullins and R.F. Sekerka, J. Applied Phys. 34, 323 (1963).
8. J.F. Yee, M. Lin, K. Sarma and W.R. Wilcox, J. Crystal Growth 30, 185 (1975).
9. K. Sarma, Ph.D. Thesis, Univ. of Southern California (1978).
10. R.A. Lefever, W.R. Wilcox and K. Sarma, Mat. Res. Bull. 13, 1175 (1978).
11. S. Sen, Ph.D. Thesis, USC (1976).
12. S. Sen, W.R. Wilcox and R.A. Lefever, Met. Trans. 9A, 462 (1978).
13. R. Gray, Private Communication, Clarkson Univ. (1987).

14. R. Singh, A.F. Witt and H.C. Gatos, J. Electrochem. Soc. 112 (1968).
15. R.D. Barnard, Thermoelectricity in Metals and Alloys, John Wiley and Sons, New York (1973) Ch.1.
16. H. Scholz and L. Kluckow in Crystal Growth, Ed. H.S. Peiser, Pergamon (1976) p. 475.
17. M. Schieber in Crystal Growth and Materials, Eds. E. Kaldis and H. J. Scheel, North Holland, Amsterdam (1977) p. 279.
18. R.H. Saul, J. Electrochem. Soc. 118, 793 (1971).
19. K.A. Jackson and C.E. Miller, J. Crystal Growth 42, 364 (1977).
20. A.F. Ioffe, Zhur. Tekh. Fiz. 26, 478 (1956).
21. W.G. Pfann, K.E. Benson and J.H. Wernick, J. Electronics 2, 597 (1957) 597.
22. J.M. Bardeen and B.S. Chandrasekhar, J. Appl. Phys. 29, 1372 (1958).
23. H.C. Gatos, A.F. Herman and A.F. Witt, ASTP Summary Science Report, NASA, vol. 1, sec.5 (1977).
24. A.F. Witt, M. Lichtensteiger and H.C. Gatos, J. Electrochem. Soc. 120, 1119 (1973).
25. A. Muragai, H.C. Gatos and A.F. Witt, J. Electrochem. Soc. 123, 224 (1976).
26. M. Kumaguwa, Jap. J. Appl. Phy. 24, 166 (1985).
27. M. Kumaguwa, J. Crystal Growth 41, 245 (1977).
28. T. Bryskienrg, C.F. Boucher and H.C. Gatos, J. Crystal Growth 82, 279 (1987).
29. L. Jastrzchski, H.C. Gatos and A.F. Witt, J. Appl. Phys. 49, 5909 (1978).
30. R.J. Schaefer and M.E. Glicksman, Acta. Met. A16, 1009 (1968).
31. C.A. Domenicali, J. Appl. Phys. 28, 749 (1957).
32. T.W. Fu and W.R. Wilcox, J. Crystal Growth 48, 416 (1980).
33. B. Duran, Private Communication, Clarkson Univ. (1987).

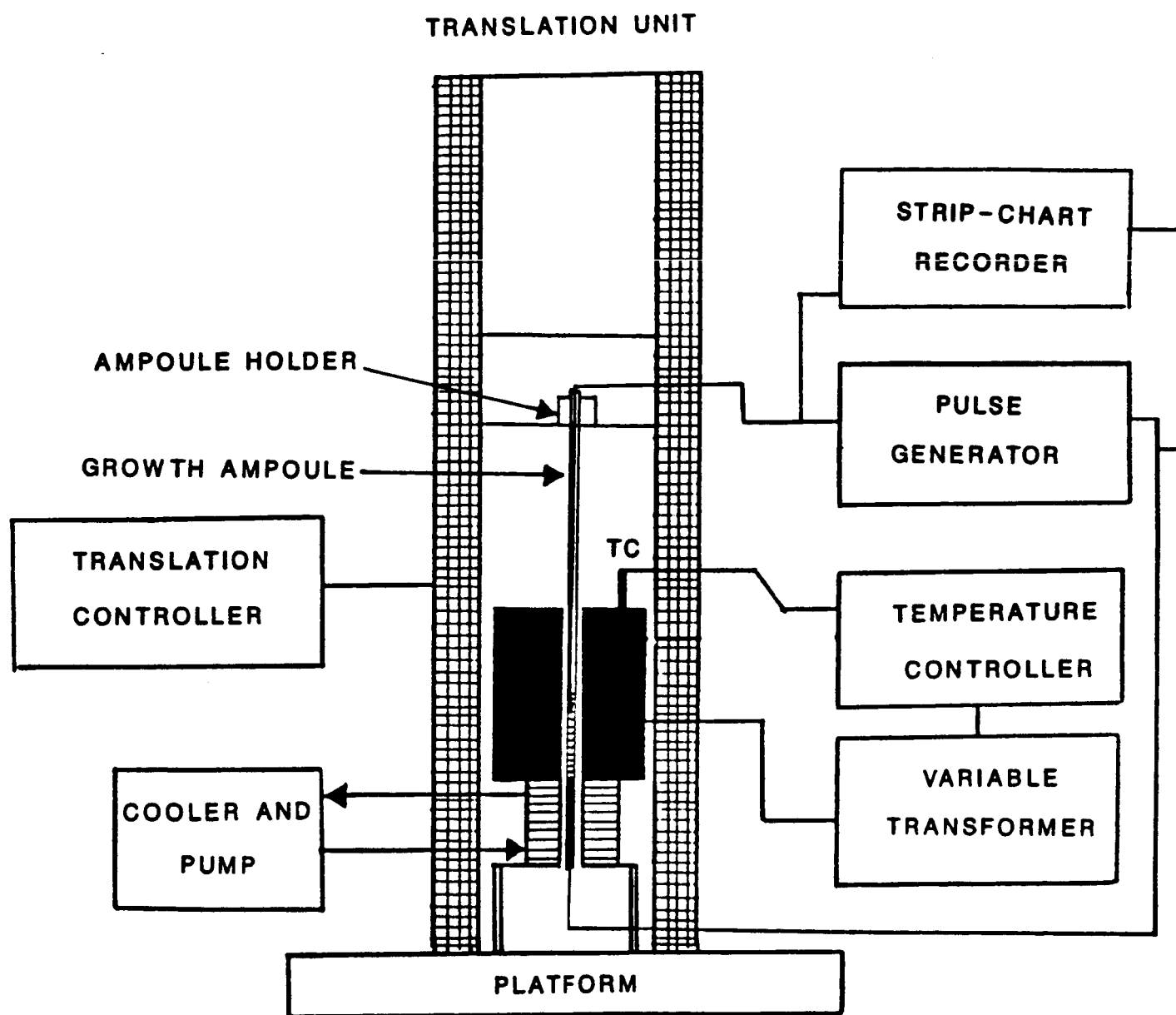


Figure III.1. Vertical Bridgman-Stockbarger apparatus with Peltier Interface Demarcation system.

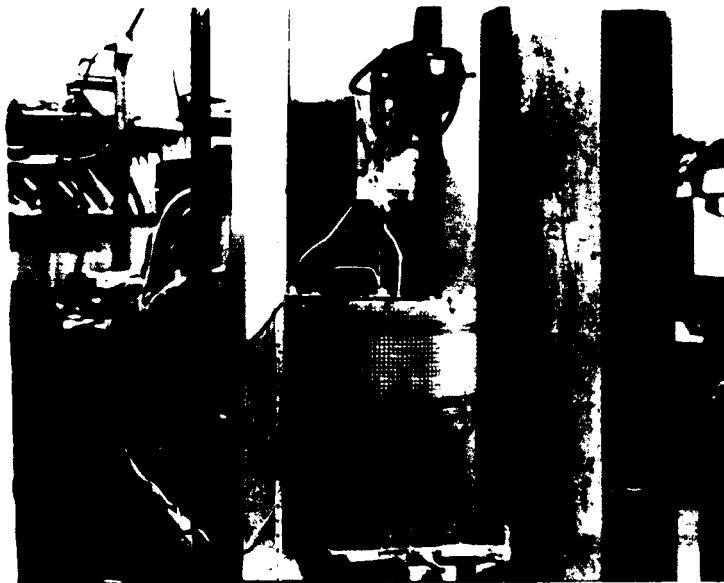
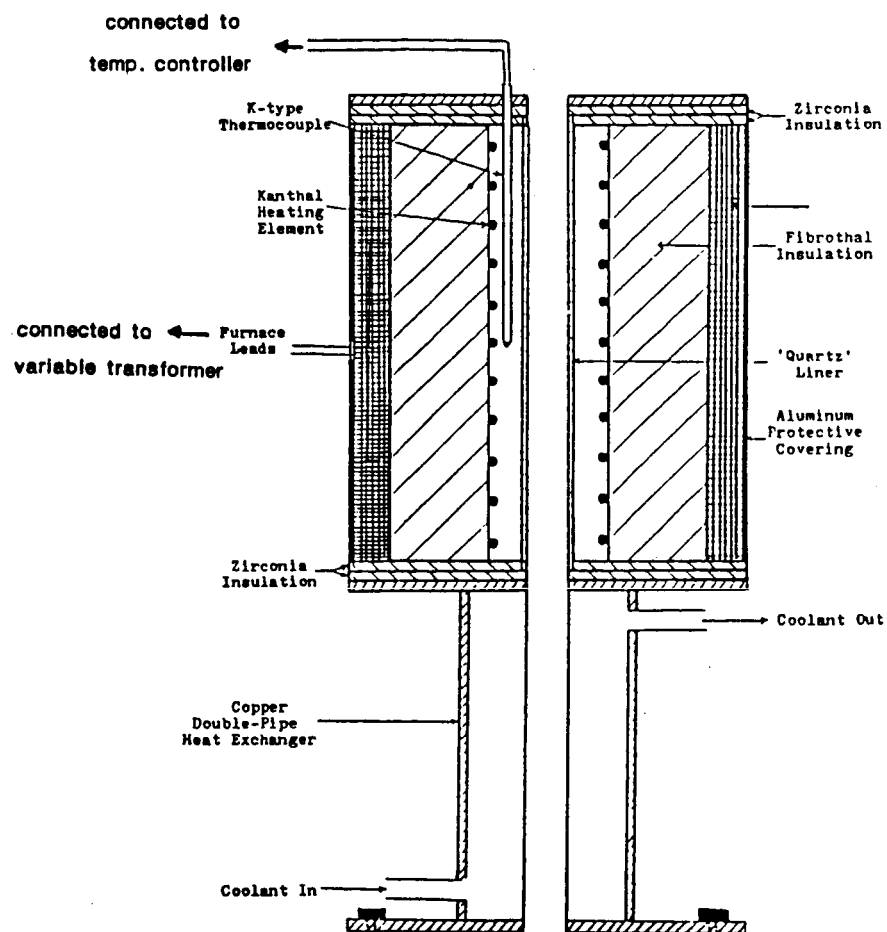


Figure III.2. Bridgman-Stockbarger furnace.

ORIGINAL PAGE IS
OF POOR QUALITY

ORIGINAL PAGE IS
OF POOR QUALITY

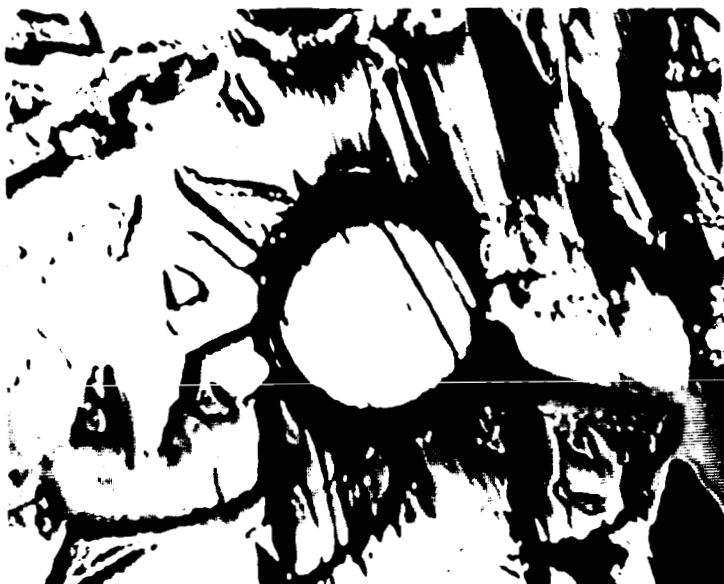


Figure III.3. 7 mm tungsten wire embedded in indium gallium antimonide.



Figure III.4. 1 mm molybdenum wire embedded in indium gallium antimonide.

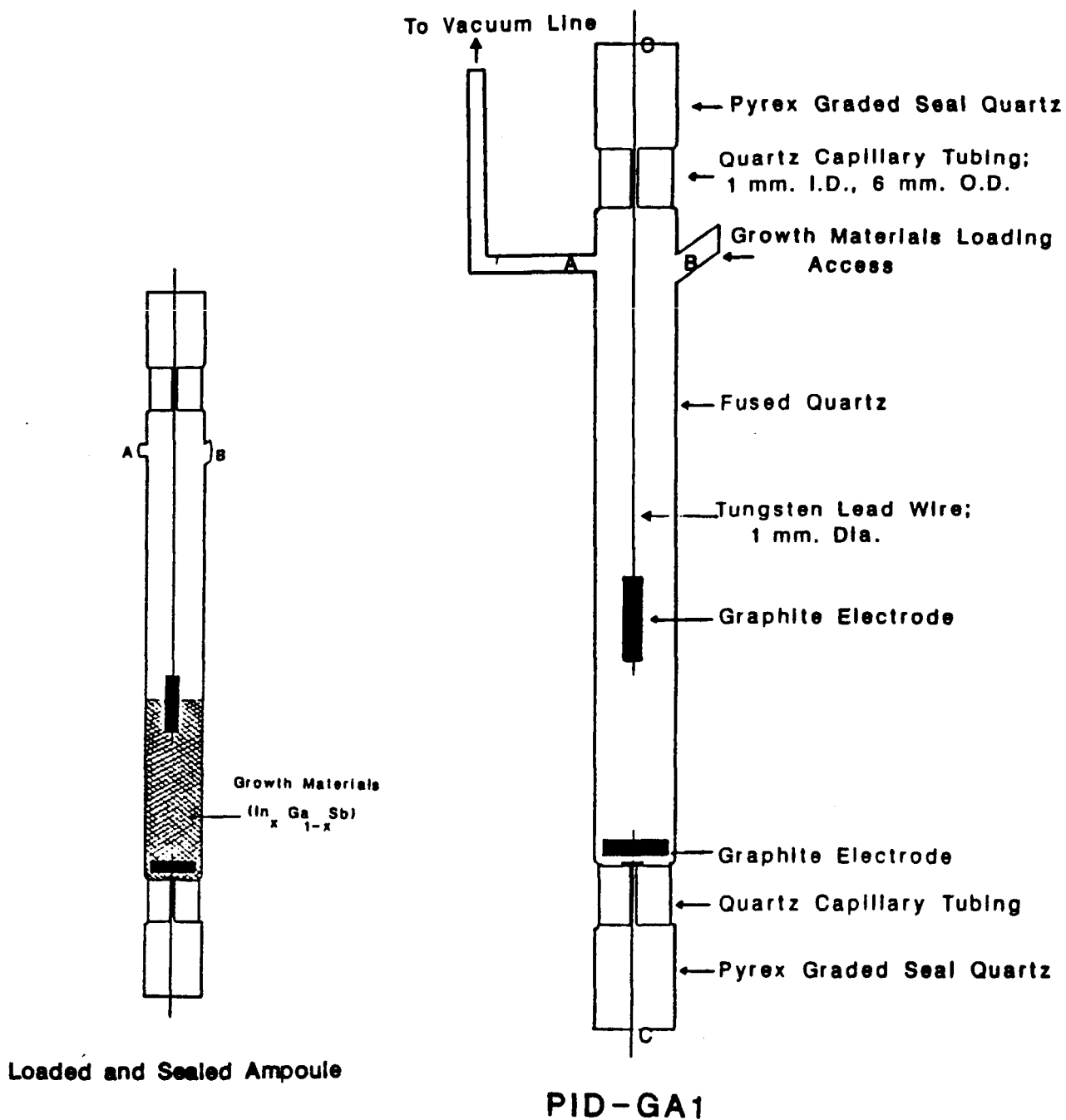
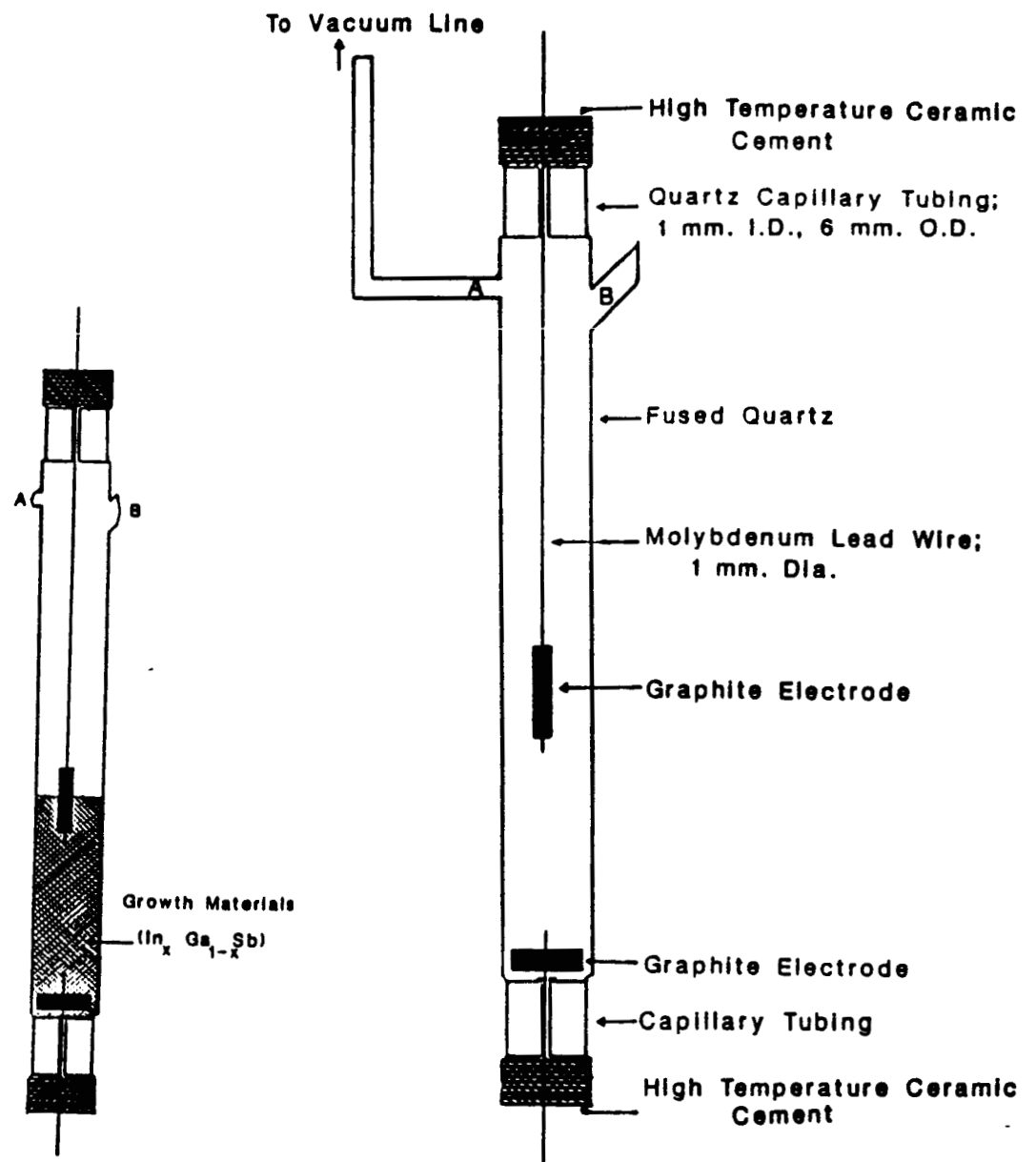


Figure III.5. Growth ampoule with Peltier Interface Demarcation.



PID-GA2

Figure III.4. Growth ampoule with Peltier Interface Demarcation.

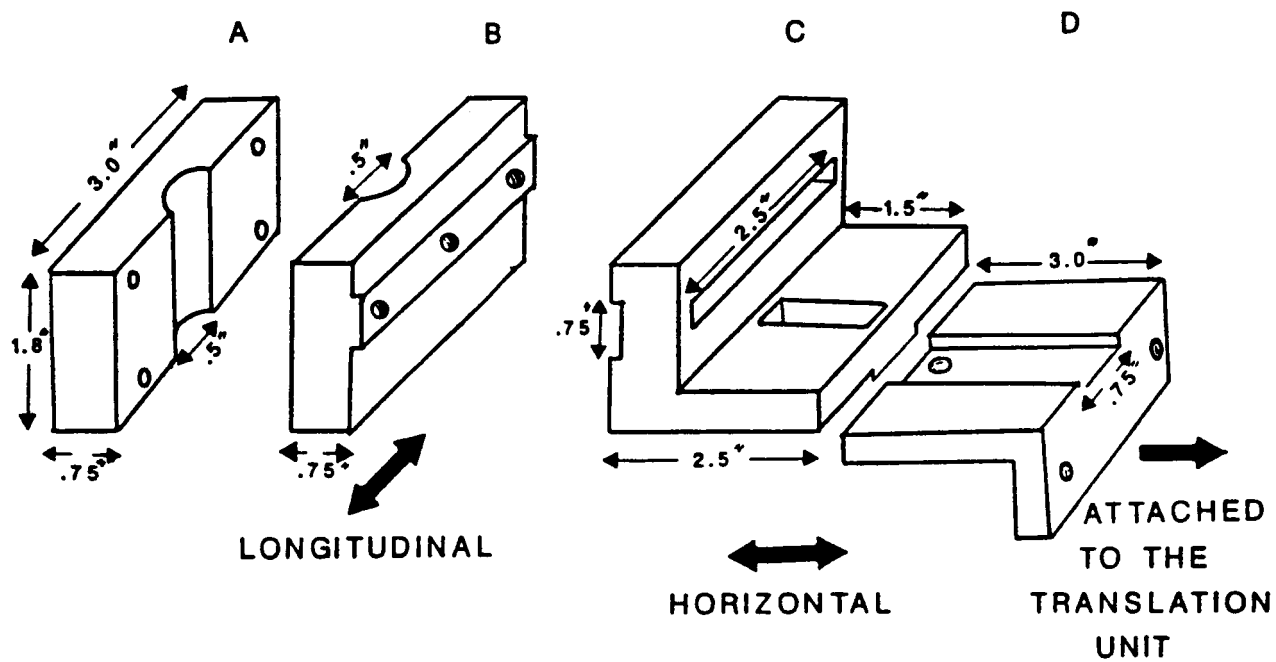


Figure III.5. Ampoule holder.

A P P E N D I C E S

APPENDIX A

Influence of Spin-up/Spin-down on the Compositional
Homogeneity and Crystallographic Perfection of Alloy
Semiconductors

A Doctoral Research Proposal

by

Ross T. Gray

May 1987

Contents

1	INTRODUCTION	5
1.1	Background and Introduction	5
1.1.1	Constitutional Supercooling	5
1.1.2	Convection	10
1.2	Objectives	13
2	LITERATURE REVIEW	14
2.1	The Growth of Indium Gallium Antimonide	14
2.1.1	Application of a Magnetic Field	14
2.1.2	Space Processing	16
2.1.3	Early Growth Experiments	18
2.2	Modeling of Vertical Bridgman-Stockbarger Growth	20
2.2.1	Heat Transfer	20
2.2.2	Heat, Mass, and Momentum Transport	24
2.2.3	Heat and Momentum Transport	26
2.2.4	Stress Distribution in Bridgman Crystals	27
2.2.5	Summary	27
2.3	Spin-up/Spin-down	29
2.3.1	General Review	29
2.3.2	Crystal Growth Using Spin-up/Spin-down	32
2.3.3	Modeling of Striations Induced by Spin-up/Spin-down	33
2.4	Twinning	44
3	EXPERIMENTAL	47
3.1	Equipment	47
3.2	Experimental Design	52

3.3	Experimental Procedure	55
------------	-----------------------------------------	-----------

List of Figures

1	The InSb-GaSb pseudo-binary phase diagram.	6
2	Schematic representation of constitutional supercooling.	9
3	Critical G/V ratio for $In_{1-x}Ga_xSb$	11
4	Differential slice of solidified ingot used in the model development. .	36
5	Striation damping for $t_c = 60\text{ s}$ and $D_o = 1.2E - 7 \frac{cm^2}{s}$	37
6	Striation damping for $t_c = 60\text{ s}$ and $D_o = 1.2E - 7 \frac{cm^2}{s}$	37
7	Striation damping for $t_c = 60\text{ s}$ and $D_o = 1.2E - 7 \frac{cm^2}{s}$	38
8	Striation damping for $t_c = 6\text{ s}$ and $D_o = 1.2E - 7 \frac{cm^2}{s}$	38
9	Striation damping for $t_c = 100\text{ s}$ and $D_o = 1.2E - 7 \frac{cm^2}{s}$	41
10	Striation damping for $t_c = 60\text{ s}$ and $D_o = 1.2E - 6 \frac{cm^2}{s}$	41
11	Striation damping for $t_c = 60\text{ s}$ and $D_o = 1.2E - 8 \frac{cm^2}{s}$	43
12	Striation damping for $t_c = 60\text{ s}$ and $D_o = 1.2E - 9 \frac{cm^2}{s}$	43
13	VBS growth furnace and cooler.	48
14	Block diagram of experimental apparatus.	50
15	Sectioning of grown ingot for analysis.	57

List of Tables

1	First experimental block.	54
2	Second experimental block.	54
3	List of successful etchants.	58

1 INTRODUCTION

1.1 Background and Introduction

1.1.1 Constitutional Supercooling

Bulk, single crystals of $In_xGa_{1-x}Sb$ have possible applications as microwave oscillators due to the observance of the Gunn effect in this alloy [1,2,3]. Alloy systems offer the advantage of having a composition dependent band structure which allows one to vary the crystal properties in order to suit different applications. The optimum substrate composition for operating optoelectronic devices is about 80% GaSb. However, the necessary electrical properties have not yet been met at this composition. The material should be n-type with a carrier concentration less than $10^{15} \frac{\text{electrons}}{\text{cm}^3}$, but when grown it is p-type [2]. $In_xGa_{1-x}Sb$ only becomes n-type when $x > 0.46$.

For bulk substrate applications, homogeneous, single crystals with low defect densities are required. Experimenters have tried many different methods of growing bulk crystals of III-V alloys and almost all attempts have resulted in either polycrystalline and/or compositionally inhomogeneous crystals which are not suitable for any devices. A major cause for the lack of success in growing bulk alloys is the extensive segregation that often occurs due to the breadth of the two-phase region. The pseudo-binary, equilibrium phase diagram for the InSb-GaSb system is shown in figure 1 [4].

As $In_xGa_{1-x}Sb$ solidifies, InSb is rejected from the solid and accumulates in a solute-rich layer adjacent to the growth interface. Tiller et al. [5] described the concentration profile of impurity in the melt as a function of the growth rate, diffusivity of impurity in the melt, the interface concentration of impurity, and the

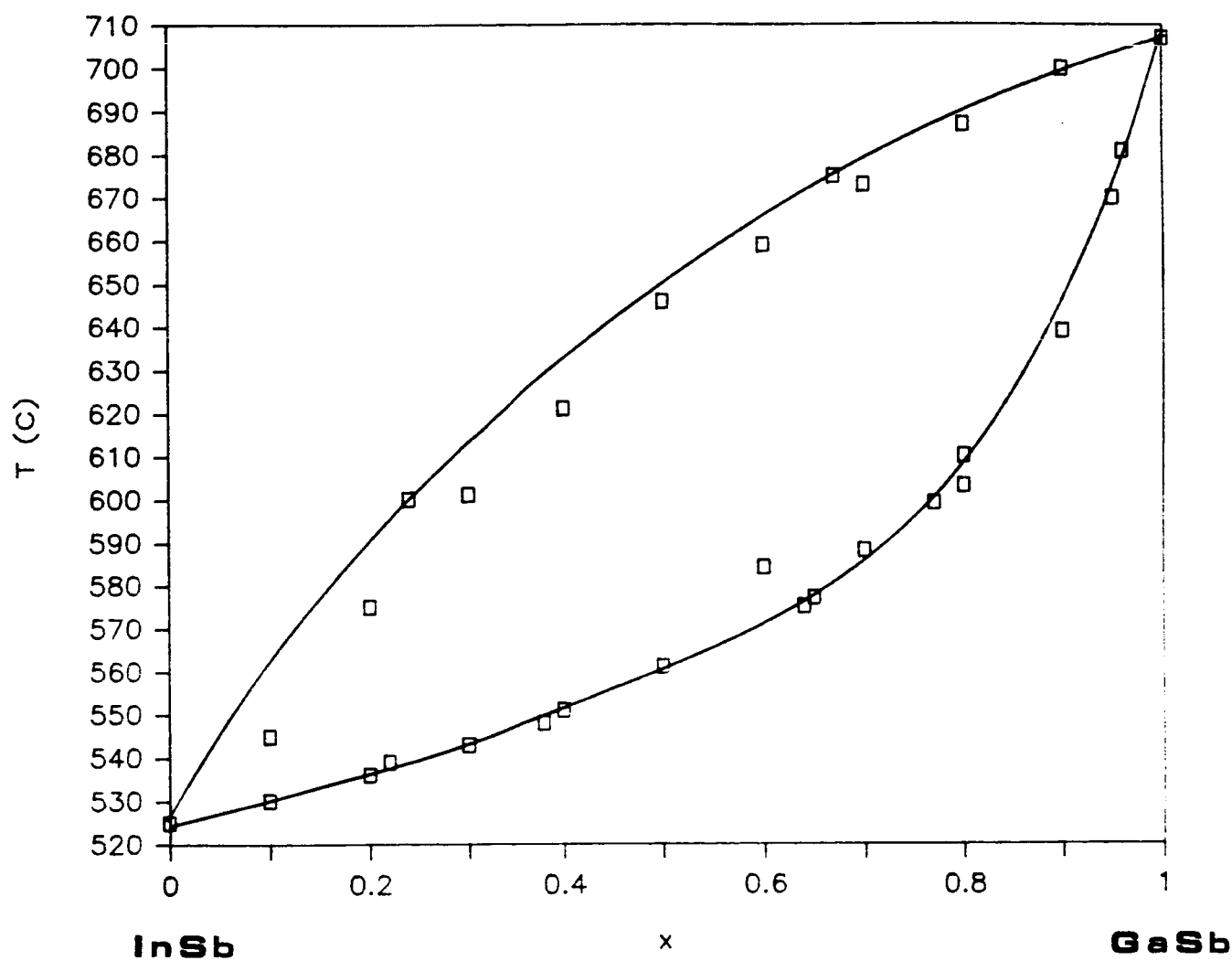


Figure 1: The InSb-GaSb pseudo-binary phase diagram [4].

bulk concentration of impurity in the melt. This profile is given by,

$$C_L = (C_i - C_o) \exp\left(-\frac{Vx}{D}\right) + C_o, \quad (1.1)$$

where C_L is the concentration of impurity in the melt at a distance x from the interface, C_i is the concentration of impurity in the melt at the interface, C_o is the concentration of the bulk melt, V is the flow velocity in the melt created by solidification (a result of fixing the coordinate system with respect to the interface position), D is the diffusivity of impurity in the melt, and x is the distance into the melt from the interface. This equation assumes that:

- solid-state diffusion is negligible.
- steady-state.
- the interface is planar.
- there is no convection in the melt.

Severe component segregation readily leads to the condition of constitutional supercooling in the melt.

Constitutional supercooling was formulated by Rutter and Chalmers [6] to explain the breakdown of a planar growth interface to a cellular one. The basic concepts and results are presented here. A more rigorous theory based on the growth or decay of sinusoidal perturbations of the growth interface is developed in references [7,8,9].

When a melt of bulk concentration C_o solidifies at a constant freezing rate V from the melt under an imposed temperature gradient G , the lower melting component (InSb) becomes enriched in the liquid adjacent to the solid. This causes a gradient in the equilibrium melting temperature as shown in figure 2. Constitutional

supercooling exists when the imposed temperature gradient in the melt is exceeded by the gradient in equilibrium melting temperature at the interface. A mass balance at the interface leads to the following condition for the avoidance of constitutional supercooling:

$$\frac{G}{V} > \frac{m}{D} \left(\frac{V_{cr} C_i}{V} - C_s \right), \quad (1.2)$$

where m is the slope of the equilibrium liquidus curve and C_s is the concentration of impurity in the solid at the interface. The crystallization flow velocity V_{cr} is the flow of melt into the interface as a result of solidification. The term was coined by Wilcox [10] and will be equal to the crystal growth rate V when the solid and liquid volumetric properties are the same. This equation uses the assumptions listed for equation (1.1). It can be seen that a high imposed temperature gradient and/or a low growth rate will help prevent the onset of constitutional supercooling.

At steady-state with no mixing in the melt, $C_s = C_o$ and $C_i = \frac{C_o}{k}$ (if the units of concentration are mole or mass fraction and not $\frac{g \text{ or } g\text{-mol}}{cm^3}$), where k (assumed constant) is the equilibrium distribution coefficient at the interface and has been defined as $\frac{C_s}{C_i}$ in this paper. These conditions reduce equation (1.2) to the form,

$$\frac{G}{V} > \frac{m C_o}{D} \left(\frac{V_{cr}}{V k} - 1 \right). \quad (1.3)$$

For the case of complete mixing in the melt, $C_i = C_o$, $C_s = k C_o$, and equation (1.2) becomes,

$$\frac{G}{V} > \frac{m C_o}{D} \left(\frac{V_{cr}}{V} - k \right). \quad (1.4)$$

A schematic representation of constitutional supercooling is shown in figure 2 for the case of no mixing in the melt.

Constitutional supercooling results in the transition of a planar interface to a cellular one. The solute laterally segregates into the cell boundaries in an attempt to relieve the conditions of constitutional supercooling. If the conditions are

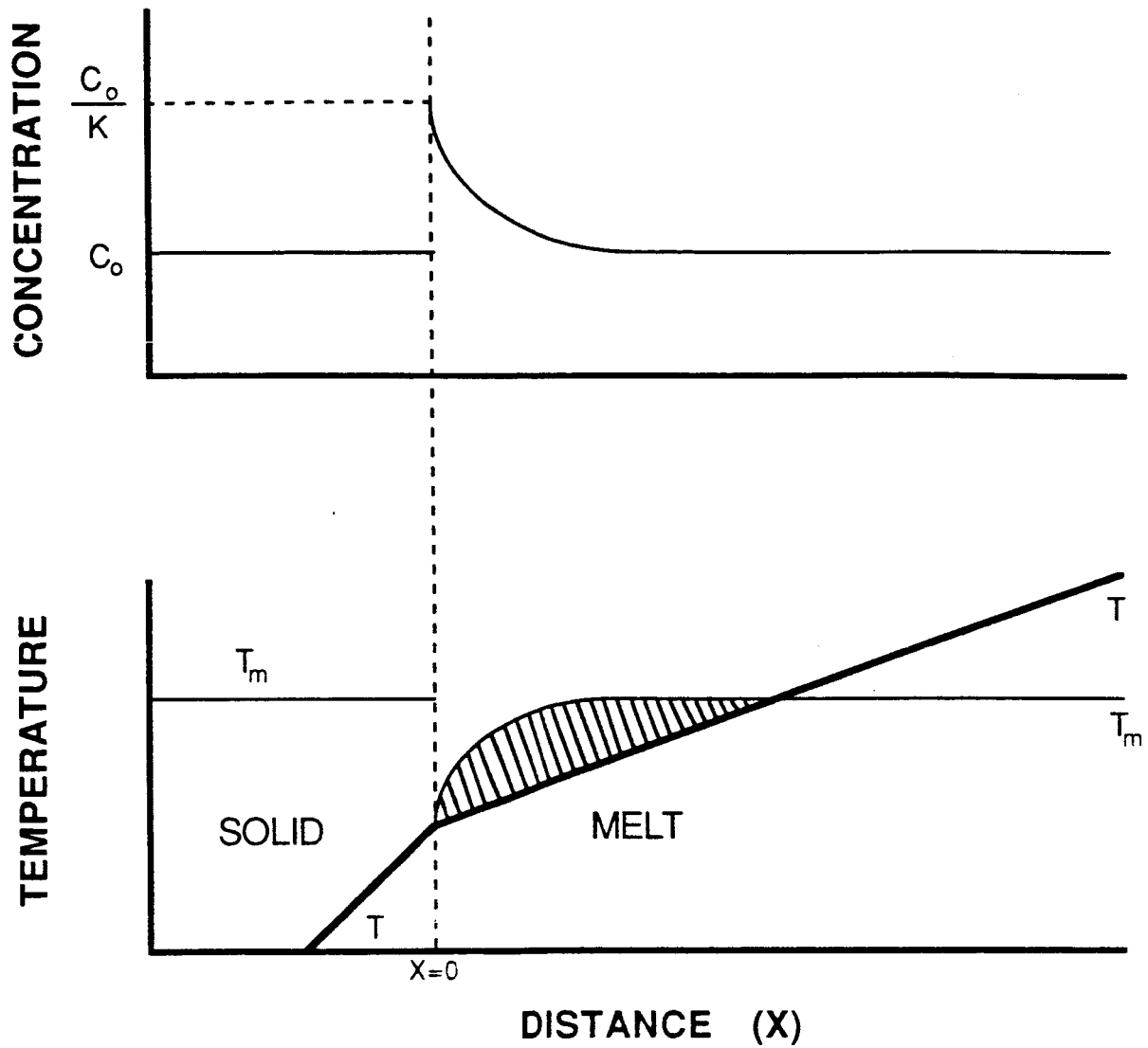


Figure 2: Schematic representation of constitutional supercooling for steady-state freezing when $k < 1.0$. Shaded portion is region of constitutionally supercooled liquid.

extreme, dendritic growth will result. Most of the solute will be trapped in the interdendritic regions causing a microsegregation problem. Inclusions, dislocations, grain boundaries, and possibly twin boundaries are a result of this type of rapid growth.

Sen [11] plotted the critical $\frac{G}{V}$ ratio from equation (1.3) versus the mole fraction of GaSb in the melt. The diffusion coefficient D was assumed to be $2 \times 10^{-5} \frac{\text{cm}^2}{\text{s}}$. This is shown in figure 3. A large region of instability exists. Sen [11] also found that increasing the imposed temperature gradient in the melt to $40^\circ\text{C}/\text{cm}$ caused increased thermal stress in the $\text{In}_x\text{Ga}_{1-x}\text{Sb}$ ingots. This resulted in microcracks and other defects. Extremely low translation rates are limited by the smoothness of mechanical motion that is available.

1.1.2 Convection

In the vertical Bridgman-Stockbarger (VBS) growth technique, the charge of metals is sealed in a growth ampoule. This ampoule is then lowered at a slow rate down through a temperature gradient created by a furnace on top of a cooler. This set-up allows one to independently control the interface shape, growth rate, and temperature gradient. This system, with the heater on top, is said to be thermally stable. However, natural convection will always be present on earth due to unavoidable radial temperature gradients and variations in composition. This convection can often be slow, time-dependent, and chaotic [12]. The result is variations in temperature and flow velocity near the interface, causing growth rate fluctuations. An inhomogeneous composition profile with striations parallel to the interface can develop.

One possible way to eliminate the problems associated with time-dependent

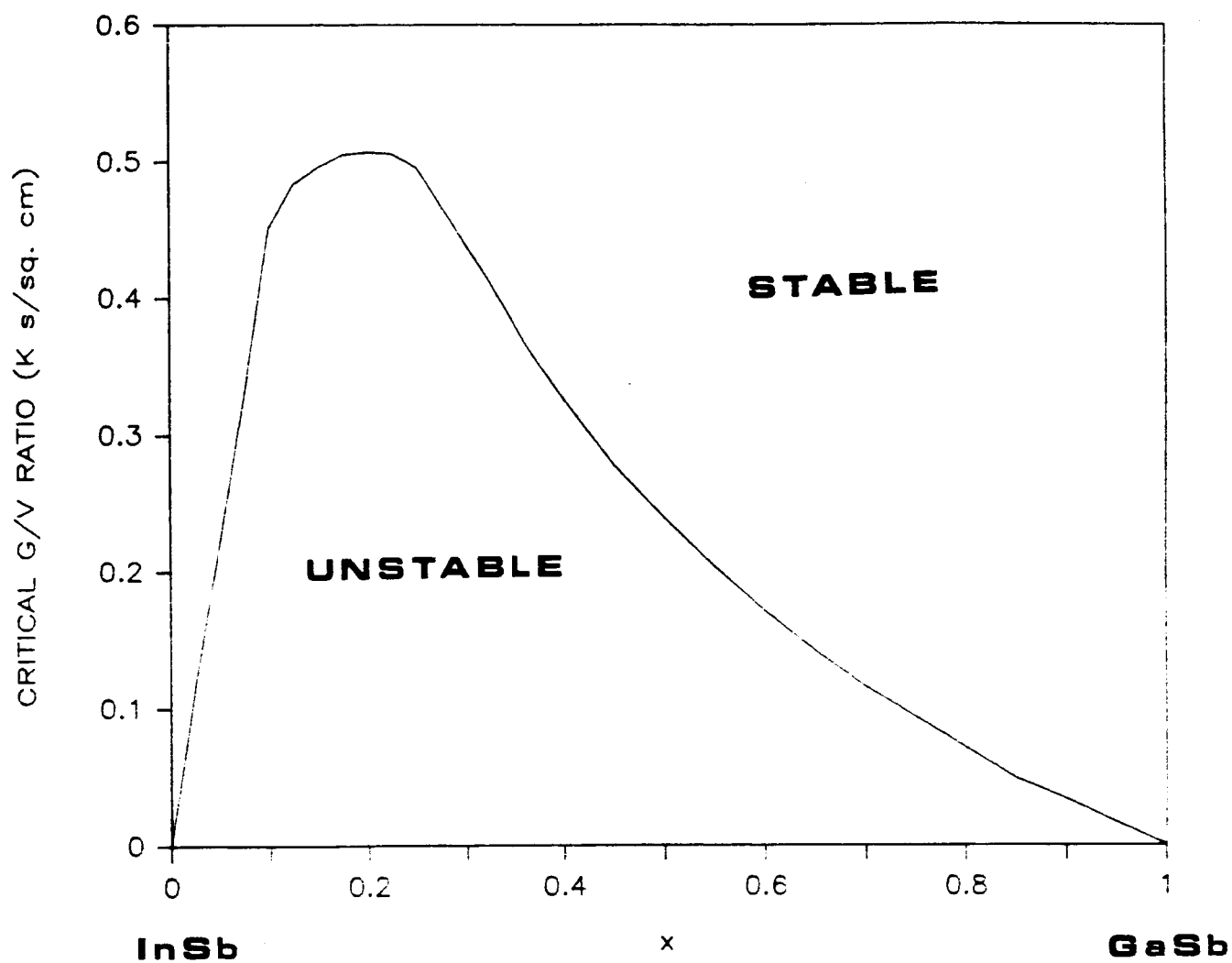


Figure 3: Critical G/V ratio for $In_{1-x}Ga_xSb$ assuming no mixing in the melt (x is the mole fraction of GaSb in the bulk melt) [11].

free convection is to attempt to suppress the convection. This could be accomplished by applying a transverse magnetic field across the melt [11] or by carrying out the solidification in space [13,14,15,16]. Another approach is to introduce regular, forced convection on a scale that will overwhelm any natural convective effects. Using forced convection offers the advantage of keeping the melt well-mixed and, consequently, damping the effects of a non-axisymmetric furnace. The major obstacle to achieving stirring evolves from the inability to place a mechanical stirring device inside the growth ampoule. A stirrer would be a source of impurities. Also, the crystal must be totally sealed in an inert atmosphere to prevent escape of volatile components and to keep the melt from reacting with the ambient atmosphere.

Spin-up/spin-down, often referred to as the accelerated crucible rotation technique (ACRT) when applied to crystal growth, is a method by which effective mixing can be achieved without making physical contact with the melt. The entire ampoule is rotated for a period of time (spin-up), motion is stopped for another period (spin-down), and this cycle is continuously repeated.

1.2 Objectives

The objective of this project is to determine the effects of ACRT on the radial and axial compositional homogeneity of $In_xGa_{1-x}Sb$ grown by the VBS technique. The effect of ACRT on twin and grain boundary formation will also be determined. Ingots will be grown with different ACRT cycle times, with different ACRT rotation rates, and with and without the application of the ACRT. The knowledge gained by determining these effects can then be used to help in understanding the growth of alloy systems from the melt.

2 LITERATURE REVIEW

2.1 The Growth of Indium Gallium Antimonide

2.1.1 Application of a Magnetic Field

Sen [11] grew bulk ingots of $In_xGa_{1-x}Sb$ by the VBS technique. She used initial compositions of $x = 0.1, 0.3$, and 0.5 and growth rates of 4 and $8 \frac{mm}{day}$. The number of grain boundaries increased by about 30% as the composition of InSb in the initial feed increased. The average number of twins was less dependent on composition.

Sen applied a transverse magnetic field across the melt during the growth of some ingots. This reduced the number of twins considerably. She attributed this to the suppression of temperature fluctuations in the melt caused by the magnetic field inhibiting natural convection. If transients in temperature occurred near an interface that was close to constitutional supercooling, a momentary drop in temperature would cause a supercooled region in front of the interface. This could possibly cause nucleation and attachment of new grains and twins before interface breakdown has time to occur [11].

Sen also found that new grains often nucleated shortly after the nucleation of twins, but in smaller quantities. Twins are geometry dominated (their shape is determined by crystallographic orientation) and, consequently, grew out quickly. Grains grew out slowly, suggesting the presence of only a slightly convex interface. A convex interface is desirable because it causes grains to grow out by propagating into the ampoule wall due to the tendency of grain boundaries to align themselves perpendicular to the melt-solid interface. This leads to the least amount of grain boundary area at the interface and, thus, is a form of energy minimization.

She grew one ingot of $In_xGa_{1-x}Sb$ with an increased temperature gradient of $40 - 50^\circ C/cm$. The ingot showed no sign of directional solidification. It contained many voids and microcracks. This indicates that constitutional supercooling is not the sole source of grains and twins [11]. The fine grain structure suggests that too steep a temperature gradient increases thermal stress and produces cracking and dislocations.

The ingots showed no significant radial composition gradients except for a slight variation after turning on the magnetic field. The mole fraction of InSb gradually increased down the length of the ingot and rose sharply at the end. In some samples, the InSb mole fraction showed much scatter at the end of the ingot. This was probably due to constitutional supercooling.

In order to investigate the suggestion that thermal stress during solidification might be the cause of grain and twin boundary formation, some of the directionally solidified $In_xGa_{1-x}Sb$ ingots were annealed with and without an applied stress [11,17]. The annealing was carried out at over 80% of the Kelvin melting point for 10 days.

With no load applied, annealing had no effect on the microstructure. Some changes did occur when a 66 g stainless steel plug was placed on top of the ingots during annealing. Annealing decreased the number of curved boundaries and increased the number of straight boundaries. The total number of boundaries did not show a statistically significant change. The influence of stress annealing increased with increasing InSb content of the ingots. No grain or twin boundaries were generated in a section of an ingot which was originally a single crystal.

These results suggest that the presence of stress during solidification probably does not cause generation of grains or twins, but may cause significant modification

of their shape while the solid is cooling [17].

Sen solidified some ingots by the vertical gradient freeze technique. In this method, no mechanical motion is necessary. Instead, the temperature of the furnace is programmed down at a slow rate to provide for crystal growth. Many more grains and twins were generated with this method. For this reason, no quantitative studies were made. One problem that occurred was that as the interface progressed further and further up into the furnace, the effect of the cooler was felt less and less. This resulted in a reduced interfacial temperature gradient, which favors constitutional supercooling.

2.1.2 Space Processing

A directional freeze experiment was performed on $In_xGa_{1-x}Sb$ samples on earth and in space [13,14,15,16]. The purpose of this was to provide information on the influence of gravity on the microstructure of the ingots. The ingots were grown by the gradient freeze method on earth and in space under otherwise identical conditions. Three ingots were grown vertically on earth, three horizontally on earth, and six in two different Skylab missions.

In the original analysis of the directionally solidified ingots, straight boundaries were taken to be twin boundaries and curved boundaries as grain boundaries [14]. After careful observation under a high magnification optical microscope, many of the curved boundaries were seen to consist of short, straight segments. Even those boundaries that appeared curved under this high magnification were found to consist of short, straight segments by scanning electron microscopic studies. It was determined by electron diffraction patterns that the short, straight segments were (111) twin boundaries [15].

The grains were dendritic in the original cast material and in the last portions to refreeze. The number of straight twin boundaries in the Skylab processed ingots was dramatically less than in those processed either vertically or horizontally on earth. The number of straight twin boundaries decreased slightly with increasing InSb composition in the feed. There were less curved boundaries (curved twin boundaries plus grain boundaries) in the Skylab processed ingots and the number of curved boundaries was found to be independent of composition.

The "curving" of many of the twin boundaries suggests energy minimization by alignment perpendicular to the growth interface in a manner commonly observed for grain boundaries [15]. Lefever et al. [15] determined that the source of the twins was the dendrites in the original cast material. There was little generation of twins in the space processed ingots, but new twins were generated frequently during solidification on earth. The mechanism for the generation of these twins is possibly the one discussed by Yee et al. [13] below.

Ingots with a higher feed composition of InSb tended to form more microcracks. This result showed no dependence on gravity. There was less volume of voids in the ingots processed vertically. The voids in the earth processed ingots were concentrated at the initial remelt interface, while they were more uniformly distributed in the Skylab processed ingots. The voids tended to be near the melt-vapor interface in the horizontally processed ingots.

According to Yee et al. [13], foreign particles were probably responsible for the differences between defect densities in earth processed and space processed ingots. This theory is based on the belief that particles at a growing interface can cause nucleation of gas bubbles, twins, and grains. Gravity would cause particles to settle on the interface where a convective stream could cause it to repeatedly impact

the interface. In space, particles would not settle and convective streams would not be present in the bulk of the melt. Thus, more twins would be generated on earth by small particles which interact more frequently with the interface. Large particles that could cause gas bubble nucleation would be concentrated in the initial portion to freeze in a vertical configuration on earth, while the gas bubbles would be randomly dispersed throughout the length of the ingot if it were processed in space.

2.1.3 Early Growth Experiments

Joullie, Allegre, and Bougnot [3] directionally solidified $In_xGa_{1-x}Sb$ by a vertical Bridgman method. The ampoule travel rates were 1.0, 0.45, and $0.25 \frac{mm}{h}$. The ingots grown at $0.25 \frac{mm}{h}$ had large grains. At a freezing rate of $1.0 \frac{mm}{h}$, a second phase arose in the form of inclusions. The ingots grown at 0.25 and $0.45 \frac{mm}{h}$ were radially homogeneous.

Woolley and Smith [18] used zone leveling to solidify an $In_{0.5}Ga_{0.5}Sb$ ingot with one pass. The zone travel rate was $2.5 \frac{mm}{h}$ in the first experiment and $1.0 \frac{mm}{h}$ in a second experiment. Neither resulted in an equilibrium solid solution (single phase condition), but the slower travel rate gave better results. They also directionally solidified an $In_{0.5}Ga_{0.5}Sb$ ingot by lowering the furnace temperature by $30^\circ C/day$ for 14 days. In each cross section, there was an inhomogeneity in composition of about $\pm 4mol\%$ [19].

Woolley, Evans, and Gillett [19] tried to improve upon this by lowering the rate of cooling so that the freezing of the entire ingot took 5 weeks. They grew two ingots, one with initial composition of 30 mol% GaSb and one with an initial composition of 70 mol% GaSb. The radial homogeneity was improved.

Ivanov-Omskii and Kolomiets [20] produced bulk ingots of $In_xGa_{1-x}Sb$ by zone leveling. They found that they were able to form equilibrium solid solutions at zone travel rates of about $1.0 \frac{mm}{h}$. At higher travel rates the structure was dendritic with many fine grains and vacancies.

2.2 Modeling of Vertical Bridgman-Stockbarger Growth

2.2.1 Heat Transfer

The vertical Bridgman-Stockbarger growth process is a method of directional solidification that has received much attention in the literature recently. Extensive theoretical modeling of heat transfer in the typical VBS apparatus has been carried out. A smaller amount of the literature has included the influence of free convection.

Chang and Wilcox [21] derived analytical solutions for the location of the isotherms within an ampoule. These solutions were achieved at the expense of many simplifying assumptions. They used a two-dimensional model which neglected the release of latent heat of fusion at the interface, free convection, and end effects (infinitely long cylinder). They assumed constant, isotropic properties that do not change upon solidification, steady-state growth conditions, and that the thermal conductivity of the crucible is the same as the solid and melt. The temperature of the heater and cooler were assumed to be constant with a step change in between (no adiabatic region). A Newton's law of cooling boundary condition (heat transfer to surroundings are modeled by a heat transfer coefficient times a temperature difference) was used at the outer surface of the ampoule. This boundary condition employed a constant heat transfer coefficient which was the same for the heater and cooler.

It was determined that the interface will be concave when it lies within the cooler and convex when it lies in the heater. Also, the sensitivity of the interface position to thermal conditions increases as the heat transfer coefficient between the ampoule and surroundings decreases, as the ampoule diameter decreases, and as the thermal conductivity increases. The dependence of interface shape on interface

position is insensitive to these parameters. The effect of increasing the ampoule translation rate is to move the isotherms toward the cooler, making them more concave.

A one-dimensional approximation was made in order to get an analytical solution which allowed for the release of latent heat at the interface. The results of this model were that an increase in latent heat moves the interface deeper into the cooler and the effect of latent heat is more pronounced at low Biot numbers $\frac{hr}{K}$ (ratio of heat loss from surface to heat conduction), where h is the heat transfer coefficient between the ampoule and surroundings, r is the radius of the ampoule, and K is the thermal conductivity of the melt (and ampoule in this case).

Chang and Wilcox suggested that a layer of insulation between the heater and cooler would force the heat transfer to be nearly axial over a much larger distance. This would decrease the dependence of interface shape on thermal conditions.

Fu and Wilcox [22] investigated the influence of an insulation layer on the stability and position of the interface in the VBS technique. Their model was based on the same assumptions as that of Chang and Wilcox [21], except that the heat transfer coefficient in the heater and the heat transfer coefficient in the cooler were different. A finite-difference technique was used to solve the two-dimensional model of the temperature field. They determined that the shape of the isotherms are more sensitive to the heat transfer coefficient in the cooler than that in the heater. The presence of insulation substantially decreases the sensitivity of the interface to changes in the heater and/or cooler temperatures. Also, the temperature gradient at the interface decreases with increasing insulation thickness, but not significantly at low growth rates.

Jasinski, Rohsenow, and Witt [23] derived an analytical solution to the one-

dimensional heat equation. They used a finite length ampoule, but neglected heat loss out the ends. They also included the release of latent heat and provided for the difference in thermal conductivity between the solid and melt. It was determined that the axial temperature gradient in the melt near the interface is adversely affected by a large thermal conductivity of the charge, large release of latent heat, and a large ratio of melt thermal conductivity to crystal thermal conductivity. Large axial temperature gradients can be obtained by increasing the heater and cooler heat transfer coefficients.

Jasinski, Rohsenow, and Witt agreed with Chang and Wilcox [21] in concluding that the effects of latent heat are felt more at low Biot numbers. They give an equation for the conditions under which latent heat effects can be reasonably neglected.

Naumann and Lehoczky [24] discuss the effects of a different thermal conductivity in the melt and solid on the shape of the isotherms in Bridgman growth. Their model is simplified greatly by using an infinite ingot and assuming that there is a zero growth rate. They also assumed a specified temperature on the boundary of the crucible that is constant in the heater and cooler and varies linearly in the adiabatic region. However, the qualitative conclusions drawn should still be valid. It was found that severe distortions of isotherms can occur due to the change in thermal conductivity upon freezing in cases where the thermal conductivity of the crucible is greater than that of the solid. This conclusion was reinforced by Horowitz and Horowitz [25]. They stressed the need to find crucible materials with lower thermal conductivity than the crystals which are being grown. Naumann and Lehoczky also concluded that a crystal thermal conductivity less than that of the melt will cause the interface to become more concave.

Sukanek [26,27] modelled heat transfer in a VBS ampoule in order to compare the freezing rate to the translation rate at different stages during growth. He used an approximate analytical solution to the one-dimensional, transient problem for very low translation rates [26] and also for moderate translation rates [27]. The freezing rate approaches the translation rate if the interface is sufficiently far from the ampoule ends. The length of ampoule required to achieve this condition increases with increasing ampoule diameter, decreasing heat transfer coefficients between the ampoule and surroundings in the heater and cooler, increasing thermal conductivity of the charge, and increasing insulation thickness. This length shows a minimum versus heater temperature when the cooler temperature is fixed.

Sukanek [27] showed that moderate ampoule velocities increase the freezing rate near the bottom of the ampoule and decrease the freezing rate at the top of the ampoule compared to the case of very low ampoule velocities. The difference between freezing rate and translation rate increases with increasing translation rate and decreasing temperature difference between the heater and cooler. The minimum deviation of freezing rate from translation rate occurs when the ampoule is centered in the VBS apparatus.

Fu and Wilcox [28] used a one-dimensional, transient heat transfer analysis to investigate the change in growth rate as a function of time after a step change in the ampoule translation rate. This model assumes that the growth rate is initially equal to the translation rate before the step change is initiated. It also assumes that there are no end effects, the properties in the liquid and solid do not vary with temperature, and that the interface temperature is fixed. After an increase in translation rate, the interface asymptotically approaches a new steady-state position deeper in the cooler. This approach to steady-state takes longer for increasing insulation thickness, decreasing Biot number, and increasing release of latent heat.

The approach to steady-state is almost unaffected by the dimensionless interface temperature $\frac{T_i - T_c}{T_h - T_c}$ where T is the temperature and the subscripts i , c , and h refer to the interface, cooler, and heater, respectively, different combinations of dimensionless ampoule moving rates ($Pe^L = \frac{VC_p r}{K^L}$ where Pe^L is the Peclet number, V is the interface velocity, ρ is the density, C_p is the heat capacity, r is the ampoule radius, and K^L is the thermal conductivity of the melt at the melting point) before and after the sudden change, and different ratios of the thermal conductivity in the liquid to that in the solid.

At very low translation rates, stiction is often a problem in the gear mechanism of the drive unit. This can cause fluctuation of the freezing rate. Fu and Wilcox [29] analyzed the response of the solid-liquid interface to this type of motion. The amplitude of the freezing rate fluctuations decrease as the frequency of the mechanical drive rate fluctuations increases. The damping of the amplitude of the growth rate fluctuations increases as the heat transfer coefficient decreases, the ampoule diameter increases, the difference between the heater and cooler temperature decreases, and the insulation thickness increases. Fu and Wilcox concluded that a completely start-stop drive mechanism can be suitable if the frequency is greater than approximately 100 hertz for the system that they investigated.

2.2.2 Heat, Mass, and Momentum Transport

Chang and Brown [30] included free convection in their analysis of radial segregation during Bridgman growth. However, they had to compromise the validity of their model by making several simplifying assumptions. The ampoule was assumed to have negligible thermal mass and the temperature of the wall of the ampoule was assumed to constant. (The importance of finite heat transfer between the furnace and the ampoule and the effect of the thermal mass of the ampoule has been shown

to be important in many of the papers already discussed.) Chang and Brown also ignored the variation of density with temperature in every term but the body force term of the Navier-Stokes equations (Boussinesq approximation). Without including the temperature dependence of density in the body force terms, there would be no driving force for convection from axial or radial temperature gradients. Steady growth conditions are assumed along with perfectly insulated ampoule ends.

Chang and Brown simultaneously solved for the velocity field in the melt, the shape of the solidification isotherm, and the temperature distribution in both phases. Only the results for the vertically stabilized, heater-on-top, arrangement are discussed here. At Rayleigh numbers between about 0 and 10^3 , the flow was primarily rectilinear. For intermediate Rayleigh numbers (10^3 to 10^6) a cellular flow developed which was driven by radial temperature gradients. The flow moved upward along the walls of the ampoule and downward at the center. The center of the cell tended to locate at the edge of the insulation zone. It moved downward and toward the wall of the ampoule with increasing Rayleigh number. A second cell developed at a Rayleigh number of a little over 10^6 . This cell moved in the opposite direction to the first and positioned itself within the insulation layer. It caused the original cell to move upwards in the melt. For Rayleigh numbers between 0 and 10^4 , the isotherms were virtually unaffected by the convection. This was determined by comparison with the convection-free results of Fu and Wilcox [22] and is a consequence of the low Prandtl number associated with liquid metals. Increasing the Rayleigh number beyond 10^4 caused the isotherms to be compressed toward the melt solid interface and some to be concave in the center.

Once the velocity field was calculated, Chang and Brown solved for the dopant concentrations in the melt. In reality, dopant concentration should be solved for simultaneously with the temperature and velocity distributions. However, Chang

and Brown considered the case of very dilute dopants with no convection caused by the density difference between the solute and solvent and no change in melting point with solute concentration. From this analysis, it was determined that the percent radial segregation increases as the distribution coefficient goes to zero and as the Schmidt number increases. Weak convection decreases radial segregation by stripping away the dopant peak caused by interface curvature when the liquid thermal conductivity is twice that of the solid. An increased thickness of insulation decreases the level of radial segregation.

2.2.3 Heat and Momentum Transport

Carlson, Fripp, and Crouch [31] also used a numerical technique to simultaneously solve for the velocity and temperature distributions in the melt. They restricted their study to a single component melt in which the density does not vary with concentration. (Although Chang and Brown [30] used a two-component system, they also used this assumption.) They assumed the shape of the interface instead of solving for it and assumed steady-state growth conditions along with steady-state laminar flow prevailed. They used a Newton's law of cooling boundary condition on the top and sides of the ampoule, but neglected the thermal mass of the ampoule. The variation of density with temperature was again neglected in every term but the body force term of the Navier-Stokes equations.

Carlson et al. found that flow persists as long as radial temperature gradients are present. A single cell exists when the interface is convex. This cell flows up along the wall and down in the center of the ampoule. Multiple, counter-rotating cells occur when the interface is concave. The cells are well-mixed, but mixing between cells occurs only by diffusion. Mixing (quantified by the value of the streamfunction) in the upper cell was found to increase with an increasing Biot number, while

the mixing in the lower cell decreases with an increasing Biot number. Mixing increases with increasing Grashof number. In the bottom cell, mixing increases with increasing insulation thickness when the interface is concave. The opposite effect is observed for a convex interface. An increase in the Prandtl number causes mixing to increase in the lower cell and decrease in the upper cell.

2.2.4 Stress Distribution in Bridgman Crystals

Huang, Elwell, and Fiegelson [32] used finite-element analysis to study factors determining the stress distribution in Bridgman crystals. These stresses can result in dislocations, cracking, and possibly twin formation. They concluded that the temperature gradient determines the stress and that interface shape is a secondary factor. In a uniform temperature gradient, a concave interface will yield the highest stress, but high stress can be associated with a convex interface when it is located in a steep temperature gradient. The maximum stress occurs at the outer portions of the ingot and is particularly high near a discontinuity in the temperature gradient (caused by a discontinuity in thermal conductivity). The least amount of stress usually occurs when the interface is planar. The applied stress from the crucible wall was found to be roughly additive with the thermal stress. In this analysis, the applied stress by the crucible wall was assumed to be a particular value. On the other hand, Horowitz and Horowitz [25] claimed that this stress does not exist on the crystal as a whole. They considered the expansion of semiconductors upon freezing to be directed upwards, not against the crucible wall.

2.2.5 Summary

All of the preceding articles contain useful information to aid in the understanding of the complex phenomena present in VBS growth. However, each analysis is limited

by certain assumptions. Care should be taken when using the information for anything more than gaining a qualitative understanding of VBS growth. The usefulness of quantitative relationships to improve the design of VBS apparatus is hindered by the lack of knowledge of the important physical properties, the oversimplification of the boundary conditions used in the models, and the lack of comparisons made between theory and experiment.

2.3 Spin-up/Spin-down

2.3.1 General Review

Uniform crucible rotation does not lead to adequate mixing in the melt. For a fluid of constant density, the crucible and the melt rotate at the same angular velocity (rigid-body rotation). Periodically bringing a crucible from rest to rotation leads to effective stirring of the melt. Fluid near the walls tends to follow changes in crucible rotation with little delay, while the interior fluid tends to continue its previous motion due to inertia.

The pattern of flow in spin-up/spin-down, often referred to as the accelerated crucible rotation technique (ACRT) when applied to crystal growth, was characterized in a classic analysis of the topic by Greenspan [33]. Benton and Clark [34] provided an excellent review of Greenspan along with the work on the subject between 1963 and 1973. These two works provide a fundamental description of the important types of fluid flow mechanisms present in spin-up.

The Ekman number is a dimensionless group used to characterize the spin-up process:

$$E = \frac{\nu}{L^2 \Omega}, \quad (2.5)$$

where L is a characteristic dimension, ν is the kinematic viscosity, and Ω is the angular rotation rate. For Ekman numbers of about one and greater, the spin-up process proceeds by viscous diffusion of vorticity from the cylinder wall. The characteristic time for vorticity to reach the midplane is,

$$t_\nu = \frac{L^2}{\nu}. \quad (2.6)$$

Ekman numbers much less than one provide for the more interesting process of convective spin-up.

The Rossby number is used to characterize the "linearity" of the spin-up or spin-down process:

$$\epsilon = \frac{\Delta\Omega}{\Omega}, \quad (2.7)$$

where Ω is the larger of Ω_o and Ω_1 . Linear spin-up or spin-down corresponds to $|\epsilon| \ll 1$. Spin-up from rest results in $\epsilon = +1$ and spin-down to rest results in $\epsilon = -1$. These cases are referred to as non-linear.

For $E \ll 1$, rigid-body rotation is established much more quickly than viscous diffusion suggests. The characteristic time for spin-up is,

$$t_E = \frac{L}{(\nu\Omega)^{1/2}} = \frac{1}{E^{1/2}\Omega}. \quad (2.8)$$

This is called the Ekman spin-up time.

Whenever a solid boundary is approximately perpendicular to the rotation axis, a radial flow is established within a narrow horizontal layer. This occurs above the solid-melt interface when the ACRT is applied to crystal growth. This type of flow is referred to as Ekman-layer flow. Immediately after an impulsive increase in the rotation rate, a viscous Rayleigh shear layer forms near the walls and grows as $(\nu t)^{1/2}$. This modifies the centrifugal forces. A pressure gradient force is impressed upon the boundary-layer by the unmodified interior flow and remains unchanged. The resulting imbalance in forces causes a radial outflow that establishes itself within about 2 radians of rotation after spin-up begins. During spin-down, the resulting radial flow is inward.

The Ekman-layer flow provides for transport of fluid near the crystal surface. This is exactly where mixing is needed most during crystal growth. The Ekman layer may be considered as an accelerating mechanism [35]. Stagnant fluid from the center of the container is pumped down into the Ekman layer where it moves out

closer to the side wall and gains angular momentum during spin-up. Continuity requires that a slow vertical mass flux exist in the center of the cylinder. This supplies the Ekman layer with fluid. There is an equally weak radial inflow of fluid in this interior region above the Ekman layer. This slow, induced Ekman secondary circulation causes columnar rings of fluid to contract slightly. The Taylor-Proudman constraint of columnar motion is satisfied in the interior flow. This is strictly valid only for inviscid fluid, but the effects of viscosity on the interior motion is negligible over the time scale t_E for $E \ll 1$. The Taylor-Proudman theorem states that all three components of the fluid velocity and the dynamic pressure do not depend on the vertical coordinates.

Schulz-DuBois [35] gave a good pictorial description of the type of flow described above. Assume that a flexible “pencil” of the same density as the fluid is suspended vertically in the fluid. The permitted flow patterns are those which leave the pencil straight and vertical. A set of two vertical shear layers form along the side walls. These are referred to as Stewartson layers. The inside layer of thickness $E^{1/4}L$ actively turns the radially outward Ekman-layer flow into the vertical direction [34]. It is a layer of enhanced viscous activity. This layer propagates inward as spin-up progresses for the case of spin-up from rest. The existence of this front and the details of the flow were confirmed by Hyun et al. [36]. They simulated axisymmetric spin-up flow from rest in a right circular cylinder with an aspect ratio close to one-half. The following is a list of conclusions from Hyun et al. In the vicinity of the front, the inward radial flow is a maximum. No spin-up occurs in the interior flow until the arrival of this front. The azimuthal acceleration of fluid has its maximum value just to the rear of the front as it travels inward. An outer Stewartson layer of thickness $E^{1/3}L$ remains at the sidewall. This layer reduces the vertical velocity to zero.

Capper et al. [37] described the flow patterns specific to spin-down in the upper portions of a cylinder. During spin-down to rest, a form of Couette instability can arise. Liquid close to the container wall decelerates faster than in the bulk. This causes a centrifugal imbalance which results in the formation of tight, horizontal vortices or Couette cells. These cells alternate in their direction of flow and occur in the upper two-thirds of the cylinder.

2.3.2 Crystal Growth Using Spin-up/Spin-down

Scheel and Schulz-DuBois [38] applied the ACRT to the high-temperature flux growth of $GdAlO_3$ from a $PbO - Pb_2 - B_2O_3$ solution. They grew a crystal 1000 times greater in weight than had previously been grown without the ACRT. Scheel concluded [39] that the ACRT suppresses the adverse effects of constitutional supercooling by suppressing the formation of localized pockets of supercooled solution.

Horowitz et al. [40] used the ACRT in the Bridgman growth of incongruently melting Rb_2MnCl_4 from non-stoichiometric melts. They concluded that the application of the ACRT allowed a reduction in constitutional supercooling and an increase of the growth rates by at least a factor of four. They estimated that the ACRT increased the flow velocities along the growing crystal face by at least a factor of sixteen and decreased the thickness of the solute diffusion boundary layer by at least a factor of four.

Capper et al. [37] applied the ACRT to the Bridgman growth of $Cd_xHg_{1-x}Te$. They used a maximum rotation rate of 60 *rpm* and employed rotation reversal. Different spin-up and spin-down times were used. One crystal was grown with a run time of 120 s and a stop time of 30 s (sequence A), a second crystal was grown with a run time of 120 s and a stop time of 1 s (sequence B), and a third crystal was

grown with a run time of 8 s and a stop time of 1 s (sequence C). The crystal grown with sequence C exhibited the best radial and axial homogeneity. This crystal had a section about 8 cm in length with an axial and radial compositional homogeneity of better than plus or minus one percent. This is a significant improvement over crystals grown without the ACRT and led Capper et al. to conclude that the ACRT induced mixing is strong enough to overwhelm the effects due to density differences in the melt caused by mercury segregation. Crystals grown with the ACRT had fewer major grains when compared to crystals grown without the ACRT.

2.3.3 Modeling of Striations Induced by Spin-up/Spin-down

Concern has been expressed [35,41] over the cyclic nature of the spin-up/spin-down process and the possibility of this producing a periodic variation in the mixing adjacent to the growing interface. This could cause striations to be grown into the crystal. Recently, electrochemical experiments done by Mark Larrousse at Clarkson University have confirmed the periodic nature of the mixing resulting from spin-up/spin-down [42]. This implies that the composition of impurity in the grown solid would also fluctuate, producing striations. However, the high temperature present in the solid near the interface could cause these striations to damp out and never be seen.

In order to determine if striations would be locked into a grown ingot, a one-dimensional, time-dependent model was developed and a paper prepared for publication [43]. The model was developed by considering a volume element of differential thickness and unit area in a solidifying ingot, as shown in figure 4. A material balance around this element gives:

$$\frac{\partial}{\partial x} \left(D(x) \frac{\partial C}{\partial x} \right) - V \frac{\partial C}{\partial x} = \frac{\partial C}{\partial t}, \text{ where} \quad (2.9)$$

$$D(x) = D_o \exp \left(-\frac{Q}{R(T_m + G_s x)} \right) \quad (2.10)$$

D_o = diffusion pre-exponential

Q = activation energy for diffusion

T_m = equilibrium melting temperature of solid

G_s = temperature gradient in solid

x = distance into ingot from interface

C = impurity concentration

R = gas constant

t = time

V = crystal growth rate.

The diffusivity varies exponentially with temperature and, consequently, varies exponentially with distance along the ingot (x). This is due to the temperature gradient in the solid, which is assumed to be constant.

The boundary conditions are:

$$C(0, t) = C_a + A \sin \left(\frac{2\pi t}{t_c} \right) \quad (2.11)$$

$$C(\infty, t) = \text{bounded}, \quad (2.12)$$

where t_c = ACRT cycle time and A = the amplitude of the concentration variations at the interface. The initial condition is:

$$C(x, 0) = C_a. \quad (2.13)$$

The problem was non-dimensionalized as follows:

$$\bar{C} = \frac{C - C_a}{A} \quad (2.14)$$

$$\bar{x} = \frac{x}{V t_c} \quad (2.15)$$

$$\bar{t} = \frac{D_o t}{t_c^2 V^2}. \quad (2.16)$$

Bars denote dimensionless quantities. The boundary conditions changed to:

$$\bar{C}(0, \bar{t}) = \sin \left(\frac{2\pi t_c V^2 \bar{t}}{D_o} \right) \quad (2.17)$$

$$\bar{C}(\infty, \bar{t}) = \text{bounded}. \quad (2.18)$$

The initial condition became:

$$\bar{C}(\bar{x}, 0) = 0. \quad (2.19)$$

The essential assumptions in the model are:

- a 1-D system (i.e. a planar interface)
- a constant temperature gradient
- a constant growth rate
- a semi-infinite ingot
- a sinusoidal variation in composition at the melt-solid interface.

The model was solved by a finite-difference method on the Z-200 microcomputer. The parameters of the model were chosen to simulate the VBS growth of $In_xGa_{1-x}Sb$. The value of the pre-exponential factor D_o in the diffusivity was varied along with the ACRT cycle period. The value for the activation energy for diffusion and D_o used to generate figures 5, 6, and 7 were taken from Kendall [44] and correspond to the diffusion of In in GaSb. For all simulations, Q was taken to be $12217 \frac{\text{cal}}{\text{mol}}$ and the growth rate was $4.63 \times 10^{-6} \frac{\text{cm}}{\text{s}}$. This growth rate corresponds to $4 \frac{\text{mm}}{\text{day}}$. A very high temperature gradient in the solidified ingot was used since this will reduce the damping of the striations. It is, therefore, a conservative assumption.

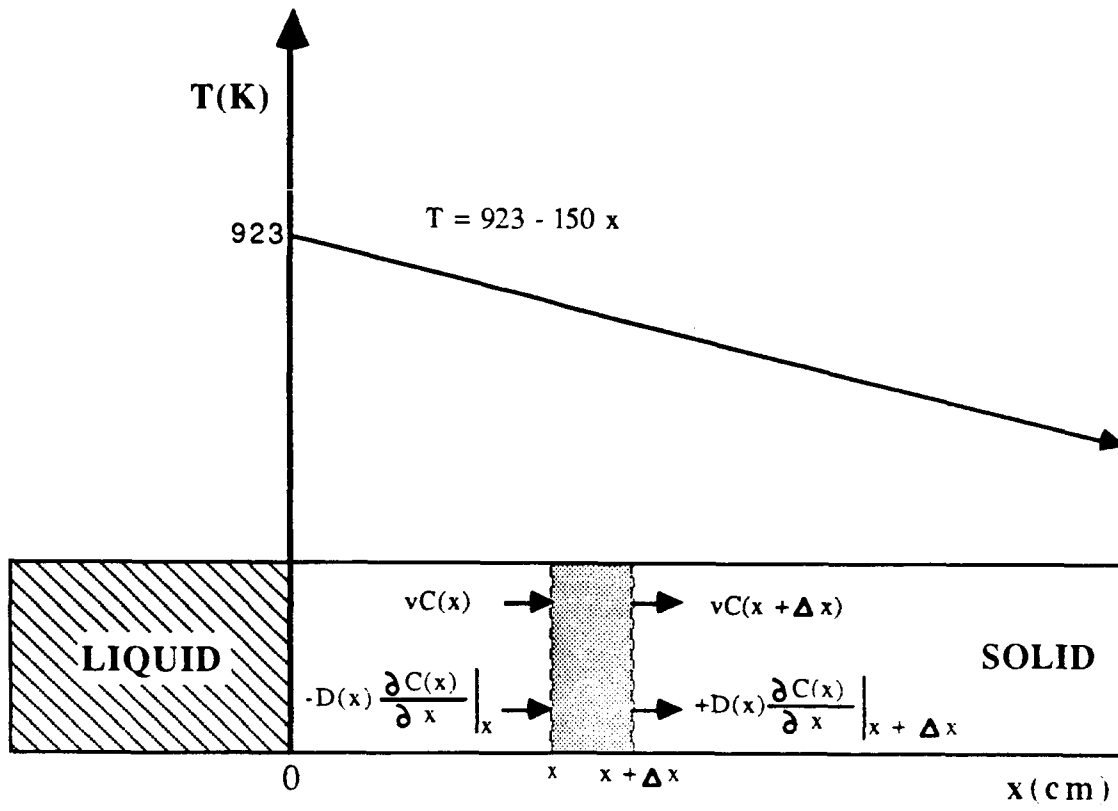


Figure 4: Differential slice of solidified ingot used in the model development.

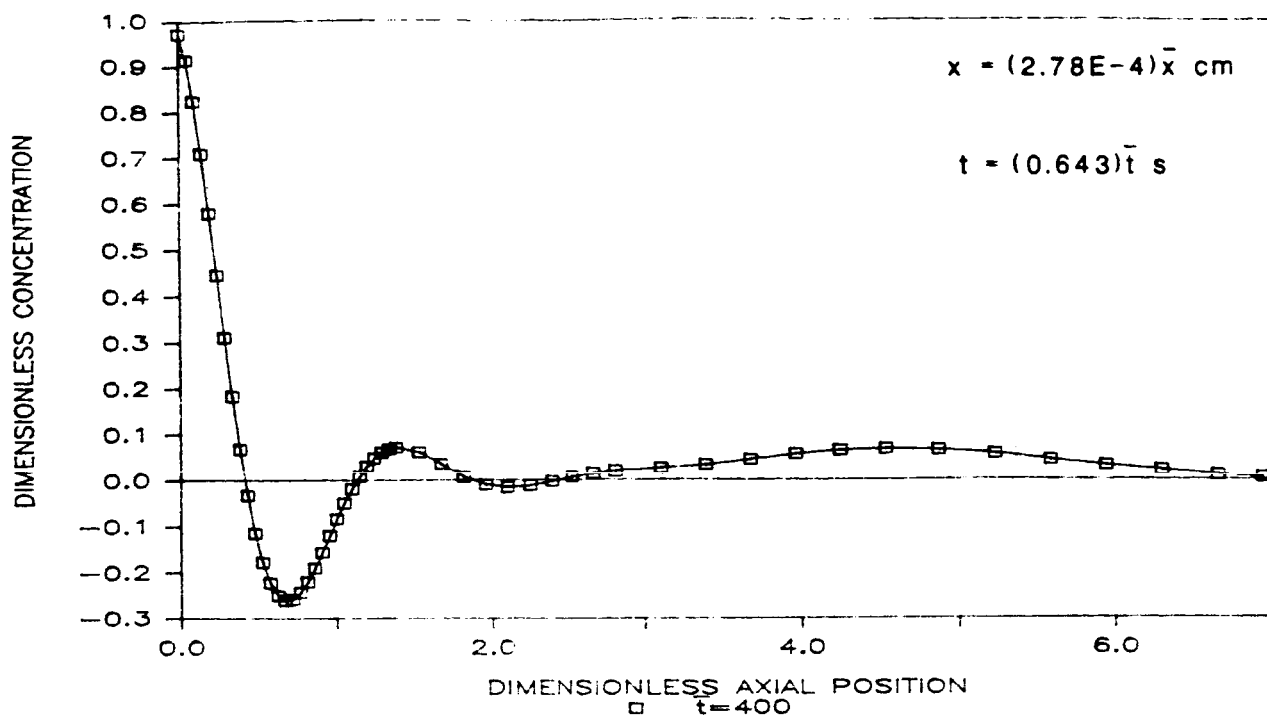


Figure 5: Striation damping for $t_c = 60 \text{ s}$ and $D_o = 1.2E - 7 \frac{\text{cm}^2}{\text{s}}$.

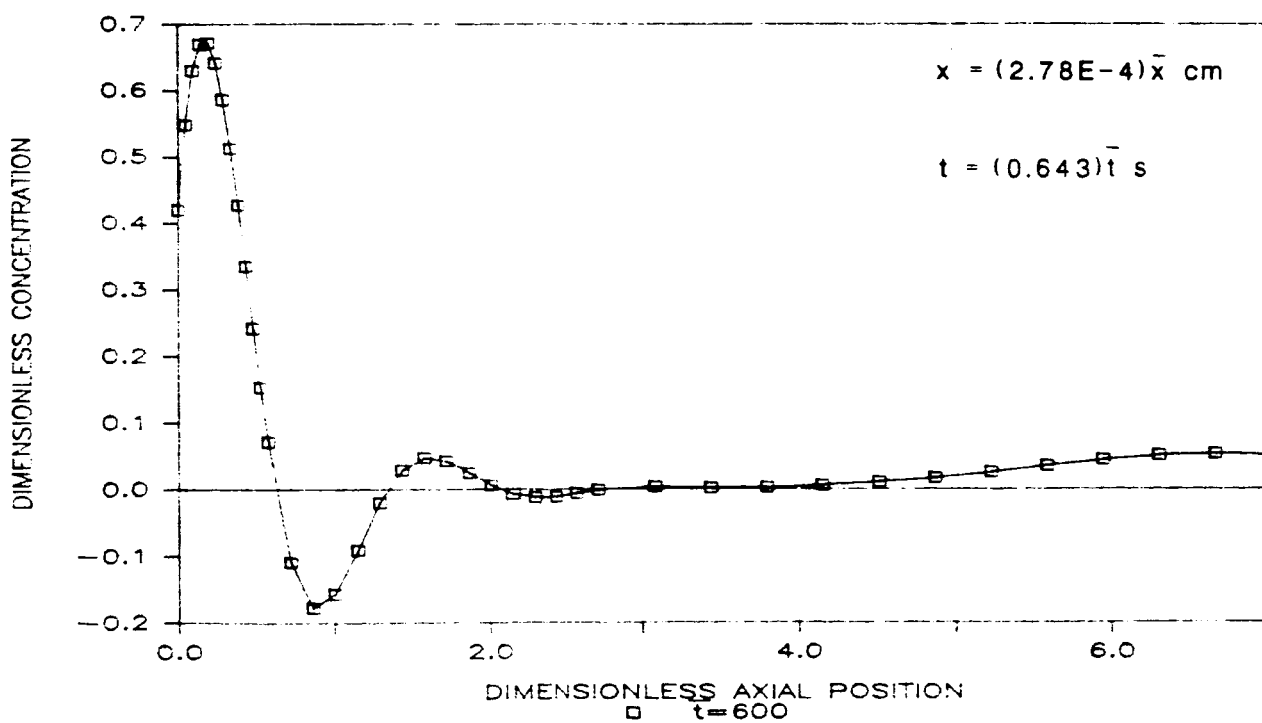


Figure 6: Striation damping for $t_c = 60 \text{ s}$ and $D_o = 1.2E - 7 \frac{\text{cm}^2}{\text{s}}$.

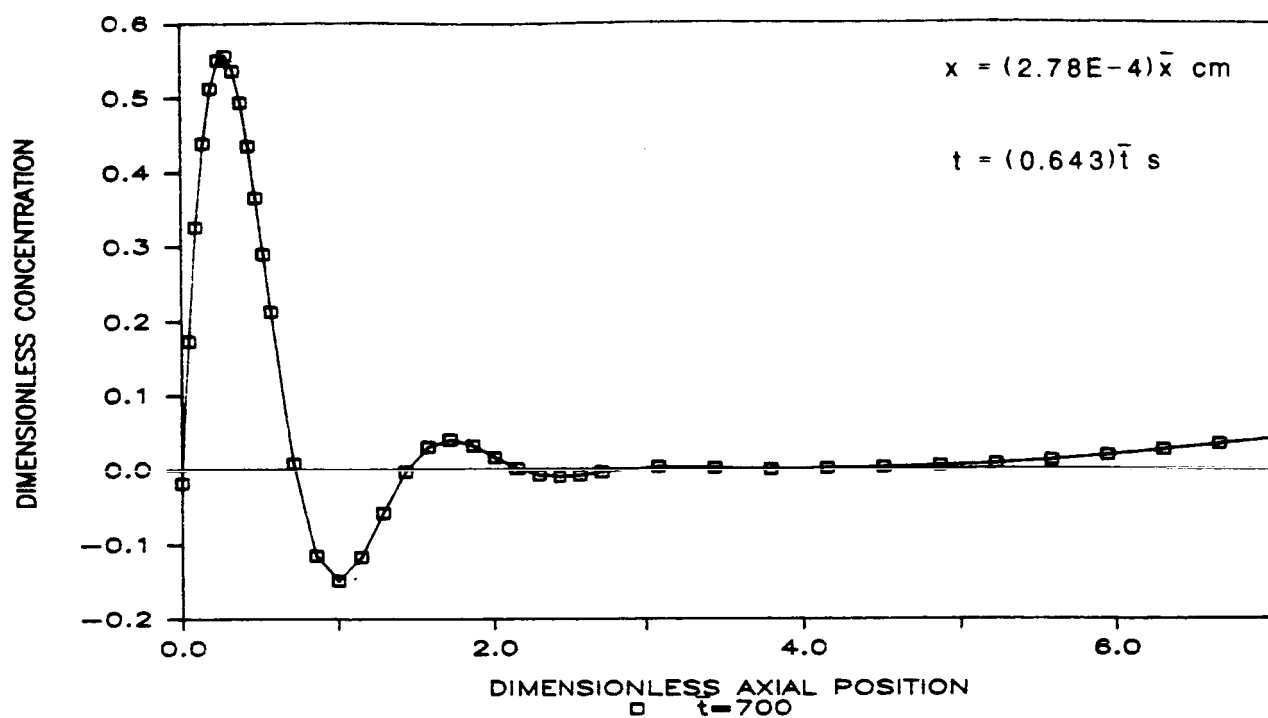


Figure 7: Striation damping for $t_c = 60 \text{ s}$ and $D_o = 1.2E - 7 \frac{\text{cm}^2}{\text{s}}$.

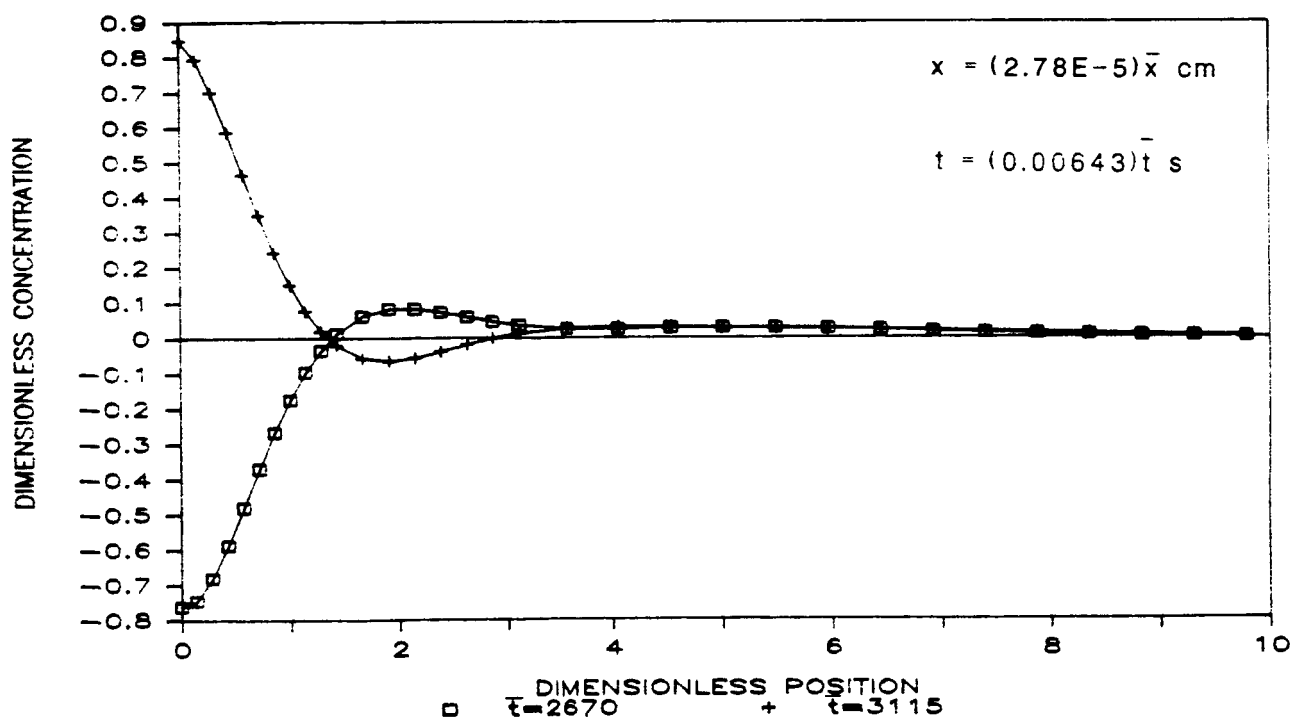


Figure 8: Striation damping for $t_c = 6 \text{ s}$ and $D_o = 1.2E - 7 \frac{\text{cm}^2}{\text{s}}$.

Figure 5 depicts the results for $In_xGa_{1-x}Sb$ at an early time. At a dimensionless time of 400, about 4.3 full cycles have had time to grow in. It is evident that considerable damping has occurred since not all cycles remain. The peak at the far right suffers from a lack of driving force on its right-hand side. This "start-up" peak is the only one that is not surrounded by negative peaks on each side.

Figures 6 and 7 represent dimensionless times of 600 and 700, respectively. By comparing figures 4, 5, and 6, it can be seen that all striations except the start-up peak are completely damped by a dimensionless position of 3. This corresponds to about 8.3 micrometers. Also, comparison of these figures reveals that no further time needs to be investigated. It is evident that a "quasi" steady-state has been attained in which the position of the final peak does not penetrate deeper into the ingot as time progresses. The start-up peak is ignored for this purpose since its nature prevents it from completely decaying until much longer times.

It is useful to recognize that a dimensionless distance of 1 unit represents the wavelength of the striation if no damping were present. Using this information, it can be seen that the striations spread considerably while damping.

Figure 8 was prepared by using an ACRT period of only 6s. This decreased cycle time caused the striations to be closer together in the ingot. Results are shown for dimensionless times of 2670 and 3115. These times are sufficient for about 2.9 and 3.3 cycles to grow in. Computing limitations prevented the acquisition of meaningful data at longer times. However, all of the cycles are not present and it should be correct to assume that almost complete damping will occur within a dimensionless position of about 5, after the start-up peak moves further into the ingot. This represents a distance of $1.4 \mu m$. The striations have spread out to a greater extent than those resulting from a 60 s ACRT period. This is a result

of the increased driving force for diffusion present as the striations grow in. For these short times, the start-up peak has only reached a dimensionless position of about 3.2. A large amount of diffusion has spread this peak to a great extent and it appears to have "swallowed" the peak behind it.

An ACRT cycle period of 100 s was used to construct figure 9. This longer period causes the striations to grow in farther apart and, thus, reduces the concentration gradient present as they grow in. The result of this reduction in driving force is a decrease in the axial spreading of the striations. More cycles remain before they damp out. The dimensionless times shown in figure 8 correspond to the times necessary for 7.5 and 10 cycles to grow in. Complete damping has occurred within 18.5 μm .

Figure 10 shows the effect of raising the value of D_o by a factor of 10. This increase in diffusivity has an effect similar to decreasing the ACRT cycle time. The dimensionless times pictured correspond to the times necessary for 5.4, 6.4, and 7.5 cycles to penetrate the ingot. The effect of the start-up peak has propagated back as it did in figure 8 for a 6 s ACRT cycle period. The result is that the striations decay to a dimensionless concentration of about 0.02 instead of zero. This occurs in a distance of 11.1 μm , a longer distance than was necessary for decay with a D_o 10 times smaller (figures 5, 6, and 7). A possible explanation for this is that the increased diffusivity caused the peak to broaden significantly immediately after growing in. This decreased the concentration gradient to such an extent that damping of the striations took longer due to the greatly reduced driving force for diffusion. The only wave remaining in figure 10 has a wavelength of about 4 dimensionless units while that of figure 6 is about 1.5 dimensionless units. This comparison confirms the argument above.

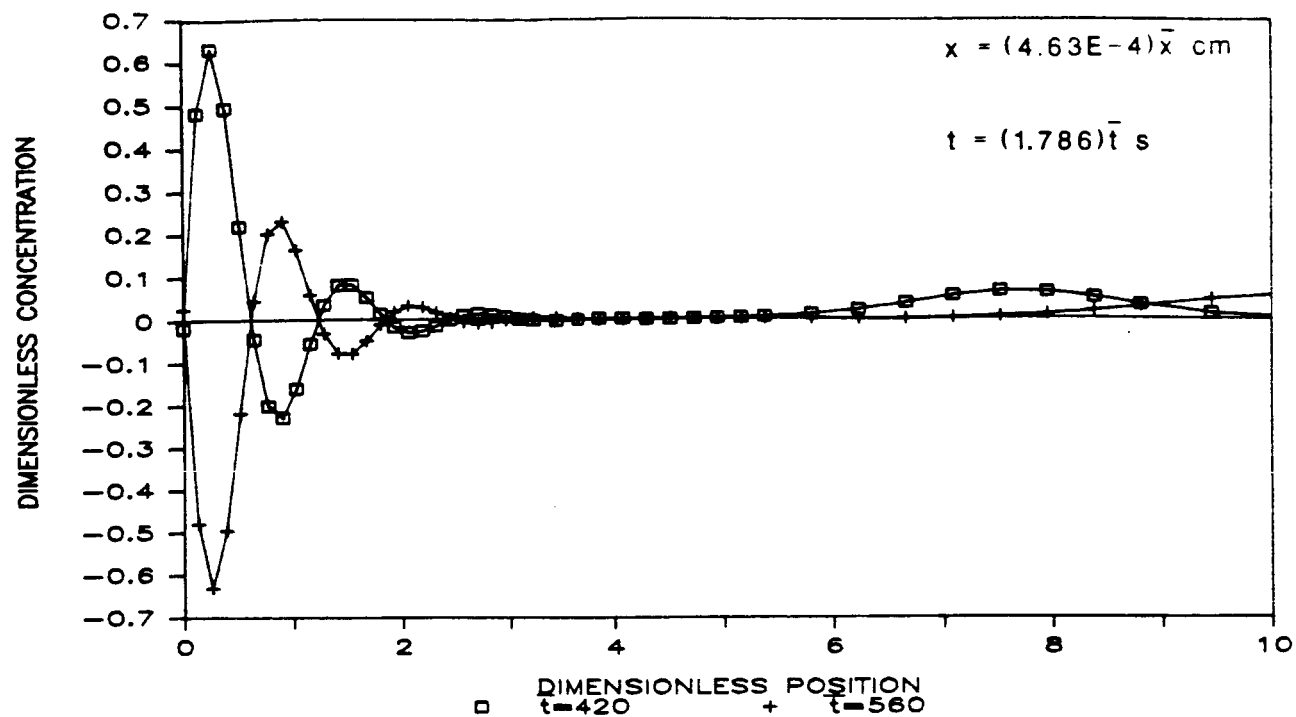


Figure 9: Striation damping for $t_c = 100$ s and $D_o = 1.2E - 7 \frac{cm^2}{s}$.

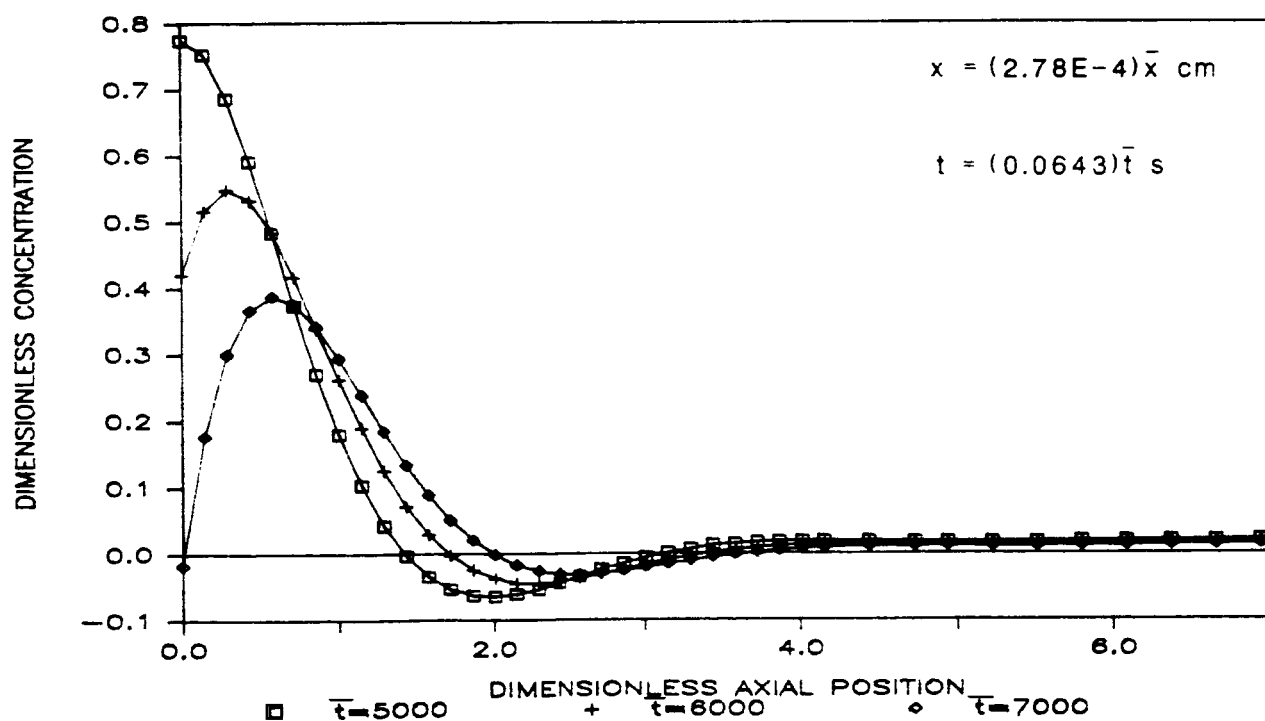


Figure 10: Striation damping for $t_c = 60$ s and $D_o = 1.2E - 6 \frac{cm^2}{s}$.

The value of D_0 used to prepare figure 11 was 10 times lower than that used for figures 5, 6, and 7. The dimensionless times shown correspond to the times necessary for 4.5 and 5.2 cycles to grow in. Every cycle still exists in the figure. This is due to the decrease in diffusivity. However, it is apparent that total damping will occur in a distance much less than 1 cm. Computer limitations prohibited the examination of times long enough to witness this. The same is also true in figure 12. This was prepared using a value of D_0 10 times less than that used in figure 11.

It is evident from figures 11 and 12 that when no striations decay or merge with the start-up peak, the wavelength of the striations will not change. Thus, if striations are seen in an ingot, they will be of the same wavelength as that at which they were grown in. Even though little damping has occurred in figure 12, it is not clear whether striations will damp in a reasonable distance. This is because only $17 \mu m$ are shown on the graph.

It is unlikely that the application of the ACRT to the VBS growth of $In_xGa_{1-x}Sb$ alloys will result in striations being locked into the solidified ingot. The growth parameters necessary for solidifying high-melting alloys are conducive to the complete damping of the striations. The large amount of segregation accompanying the solidification of non-dilute alloy systems with large liquidus regions requires that an extremely low growth rate be utilized in order to avoid the onset of constitutional supercooling. A low growth rate aids the damping of striations in two ways. At a fixed ACRT cycle time, lowering the growth rate causes the peaks of the striations to be closer together. This increases the driving force for diffusion. Also, a low growth rate allows the grown-in striation to remain at a temperature close to the melting temperature for a long time. The diffusivity of the solute is greater at these higher temperatures.

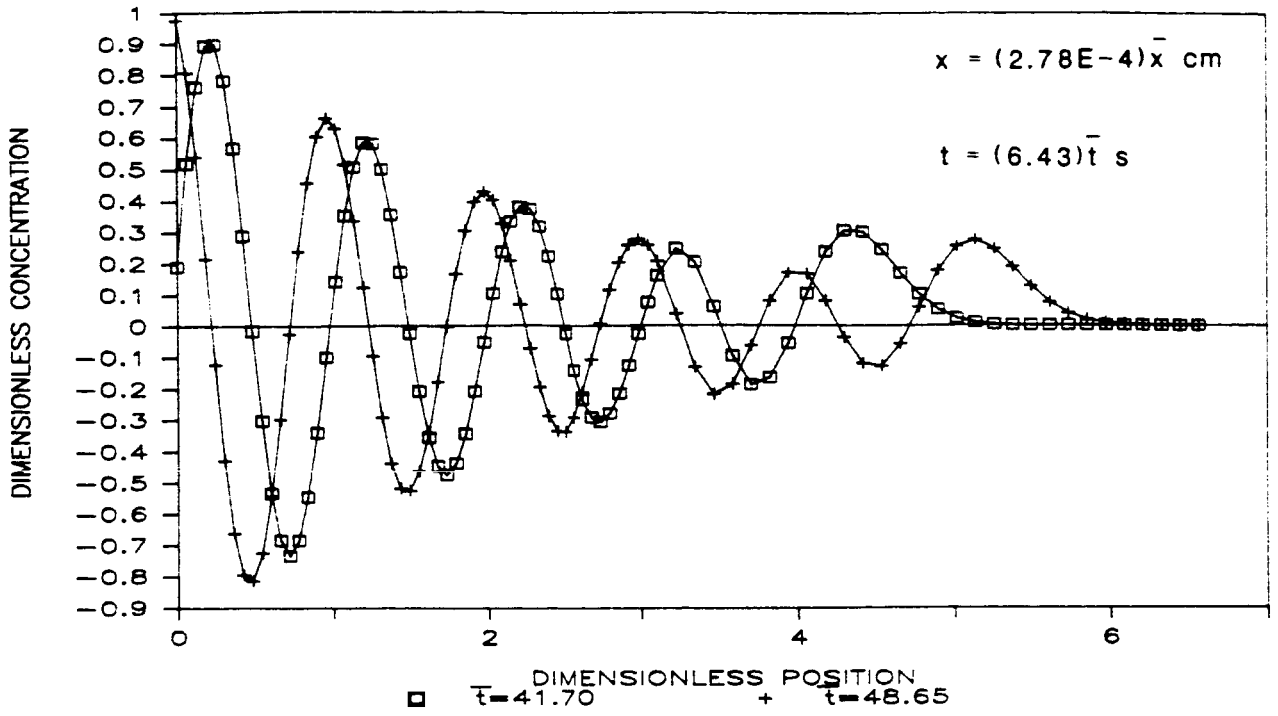


Figure 11: Striation damping for $t_c = 60 \text{ s}$ and $D_o = 1.2E - 8 \frac{\text{cm}^2}{\text{s}}$.

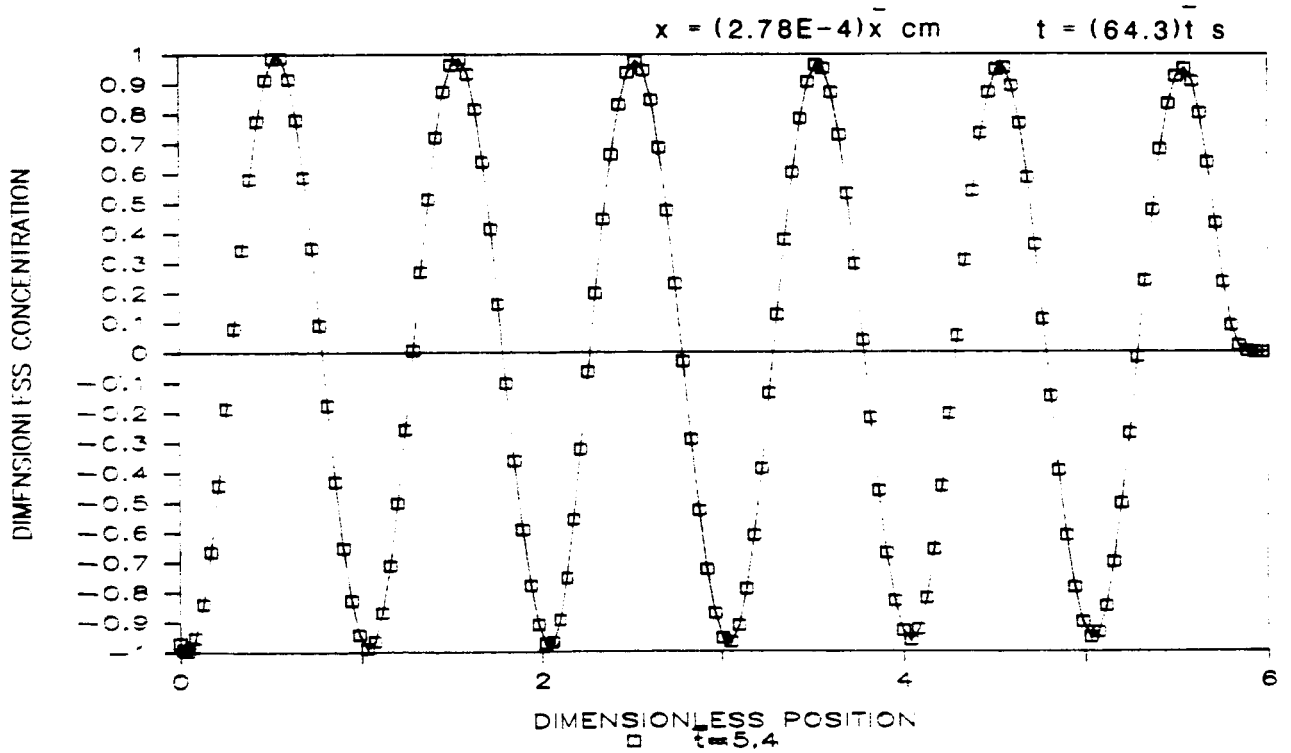


Figure 12: Striation damping for $t_c = 60 \text{ s}$ and $D_o = 1.2E - 9 \frac{\text{cm}^2}{\text{s}}$.

2.4 Twinning

A crystal is said to be twinned if it consists of parts that are joined with a specific mutual orientation. The orientation of the twinned part of the crystal is often a mirror image of the parent crystal across the twinning plane, or an orientation that represents a rotation of the twinned part of the crystal with respect to the parent crystal about the twinning axis [45].

Twin formation requires little energy and twin boundaries generally are not considered to be a grain boundary. Twins are one of the most common defects that occur during crystal growth. They are a major problem in the melt growth of III-V and II-VI alloy semiconductors. In compounds with the zinc-blende structure, like $In_xGa_{1-x}Sb$, the twinning plane is invariably $\{111\}$. These are the closest packed planes in this type of lattice. This twinning corresponds to 180° rotation about the $\langle 111 \rangle$ twinning axis. The twinned part of the crystal is also a mirror image of the parent crystal about the twinning plane.

Mechanical twinning occurs by a shearing process between lattice planes. This provides a mechanism of plastic flow in many metals where each atom shifts a distance proportional to its distance from the twinning plane [45]. The cry of a bar of tin when it is bent is caused by twinning.

Twinning can also occur during the growth of crystals from the melt, solution, or vapor. There are two basic views on the origin of growth twins.

The first view proposes that the solid might grow as a perfect crystal and twinning occurs after growth due to mechanical stress. At temperatures close to the melting point, the resistance of a crystal to deformation is extremely low [46]. Many semiconductors, including $In_xGa_{1-x}Sb$, expand upon freezing. This can cause

large stresses to arise in a crystal as it grows from the melt, especially if growth is conducted inside a crucible as in the vertical Bridgman-Stockbarger growth method. Silicon and germanium are thought to fault during constrained growth [46].

The second view is that twinning occurs directly as the crystal grows from the melt. This implies that twins form during the deposition of individual atomic layers. The bonding in a material such as $In_xGa_{1-x}Sb$ is strongly covalent, and interaction between the atoms can be approximated as being confined to nearest neighbors [46]. Twinning about a $\{111\}$ plane is a simple stacking fault. It leaves a perfect fit of the lattices on either side and leaves all bond angles undisturbed. The only energy required to form a twin is that required to overcome the interaction between second-nearest neighbors [46]. Temperature fluctuations caused by convection in the melt may be sufficient to cause this twinning [11].

Foreign particles at the growth front are also thought to cause twinning during growth [13,46,47]. The argument of Yee et al. [13] in the first section of this chapter was based on the premise that foreign particles on the interface cause twinning. Yee et al. stated that if convection was present in the melt, this would drag particles along the interface and repeatedly cause twinning.

The results of Sen [47] disagree with the above argument. She investigated the effects of impurities, foreign particles, temperature gradient, and growth rate on the twinning of 1,10-dodecanedicarboxylic acid (DDA). DDA is a clear organic and can be viewed under crossed polarizers to determine the microstructure.

Zone-refining the DDA reduced twinning by over an order of magnitude. Impurity molecules contribute to twinning to a greater extent as they approach the size and shape of the freezing organic compound. This suggests that it is necessary for the impurity molecule to be incorporated into the growing crystal if it is to

increase twinning [47]. The number of twins increased linearly as the temperature gradient increased and also as the growth rate increased. The dependence of growth rate on twinning was found to be the same for zone-refined and non zone-refined DDA.

Sen added a number of foreign particles to non zone-refined DDA. Most of these particles had little influence on twinning. Cu, Ni, Pb, and Al appeared to cause a significant decrease in the amount of twinning. However, twins could have been obscured by the many polycrystals which were caused by the presence of these foreign particles. Si and SiO_2 caused about a 25 percent increase in twinning, but twins did not emerge from these particles. The twins still grew from polycrystals as was observed in the DDA with no added foreign particles.

Sen concluded that the effects of constitutional supercooling could not be responsible for the twinning since twinning increased with an increasing temperature gradient and increased with decreasing segregation.

3 EXPERIMENTAL

3.1 Equipment

The furnace necessary for the VBS growth of $In_xGa_{1-x}Sb$ has been designed and assembled as shown in figure 13. The heating element consists of a 12 inch coil of Kanthal wire with an ID of 3 inches, surrounded by Fibrothal insulation of 9 inch OD. This was purchased from the Kanthal Corporation of Bethel, CT. The ends of this cylindrical heating element are covered by two 1/2 inch thick, cylindrical, 12 inch OD pieces of type ZYZ-6 zirconia insulation. These insulating disks were purchased from Zircar Products, Inc., Florida, NY. The purpose of the insulating region between the heater and cooler is to insure a more planar interface during growth [22]. The insulation also reduces the sensitivity of the interface shape to changes in operating conditions.

A small 15 mm ID by 20 mm OD quartz tube is used as a furnace liner and is held in place by the zirconia insulation. This tube, along with many 9 mm ID by 11 mm OD quartz tubes for growth ampoules, were purchased from Quartz Scientific, Inc. of Fairport Harbor, Ohio. A 1/4 inch thick, 12 inch OD copper plate sits on top of the furnace for mechanical stability. The cooler was constructed from two of these copper disks separated by two concentric copper pipes which serve as a double pipe heat exchanger, through which antifreeze is passed. The furnace is enclosed in a 0.016 inch thick piece of aluminum sheet metal.

The control of the temperature in the furnace is achieved by a model 6001K microprocessor based controller manufactured by Omega Engineering, Inc. of Stamford, CT. This is an on-off controller with a PID algorithm that outputs a 120V signal. Since the Kanthal heating element can operate at 60 V maximum, the signal

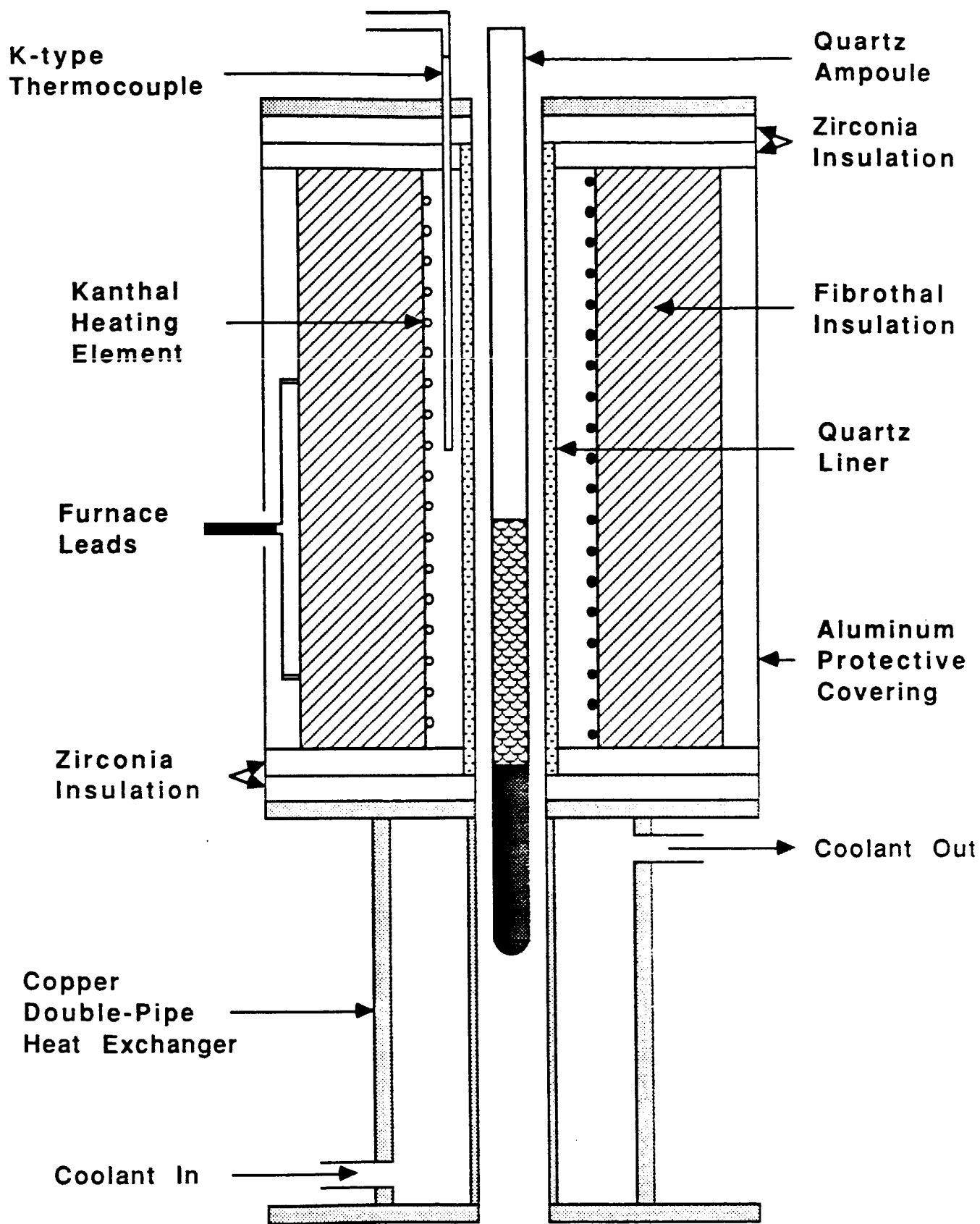


Figure 13: VBS growth furnace and cooler.

from the controller is sent to a model 126 Powerstat variable transformer, where it can be stepped down to the necessary voltage. The input signal to the controller is supplied by an inconel sheathed, K-type thermocouple inserted into the furnace as shown in figure 13. All temperature measuring devices were purchased from Omega Engineering, Inc. The controller was properly tuned and the variable transformer adjusted so that the temperature in the heater could be maintained to $\pm 1^{\circ}\text{C}$. Additional holes were made through the top pieces of copper and insulation on the furnace to allow for the insertion of three more thermocouples. This is to allow for the measurement of furnace temperature at various radial and axial positions in the furnace. These thermocouples are connected to a rotary switch which allows the output of any thermocouple to be read by a model 660 digital thermometer.

The cooling is provided by circulating a 50-50 mixture of antifreeze and water through the double-pipe heat exchanger. This is accomplished by a model RC-6 Lauda Circulator, manufactured by Brinkmann Instruments, Inc. of Westbury, NY. This provides temperature control of $\pm 0.05^{\circ}\text{C}$.

In VBS growth, a motion mechanism is necessary to lower the sealed growth ampoule down the temperature gradient supplied by the heater-cooler combination. Extremely slow translation rates (about $4 \frac{\text{mm}}{\text{day}}$) are necessary to avoid constitutional supercooling. A model 202 Zone Refiner was purchased from Crystal Specialties, Inc. of Portland, OR. This was modified to stand in an upright position and to give the desired translation rates. A Bodine type NSH-12R gearmotor was mounted on the zone refiner to provide the rotation necessary for ACRT. This motor is controlled by a Minarik model SL15 controller which is plugged into a GraLab 625 timer. This allows the ACRT cycle times to be programmed. A 1/2 inch drill chuck was modified and placed onto the gearmotor as a mechanism to hold the ampoule. A block diagram of the basic experimental setup is shown in figure 14.

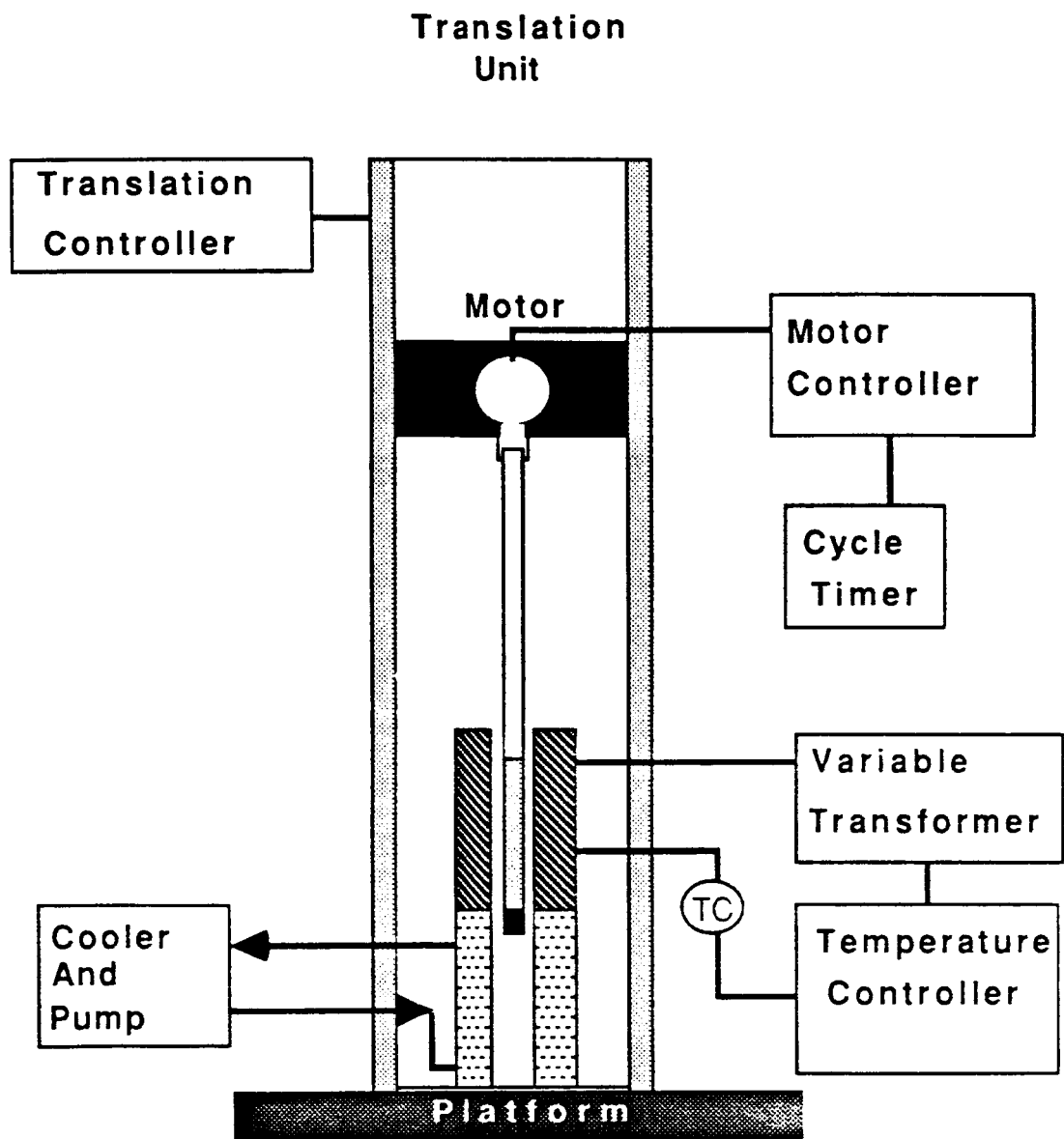


Figure 14: Block diagram of experimental apparatus.

The gallium, indium, and antimony were purchased in 1/8 inch shot form. Purchased from Cerac, Inc. of Milwaukee, WI were 150 *g* of gallium (69s) and 400 *g* of antimony (69s). Also, 100 *g* of indium (59s) were purchased from GFS Chemicals, Columbus, OH.

3.2 Experimental Design

The goal of the experiments is to determine the effect of the ACRT on the microstructure and the axial and radial compositional homogeneity of grown $In_xGa_{1-x}Sb$ ingots. It was decided to investigate the specific influence of the ACRT cycle time and the ACRT rotation rate. These variables have never been studied in detail for a VBS growth system. The number of variables that can be investigated is severely limited by the length of time needed to prepare and grow one ingot. This will be approximately one month for a crystal growth rate of $4 \frac{mm}{day}$. Additional time will be required to analyze the ingots.

The first set of experiments, involving the ACRT cycle time and rotation rate, is shown in table 1. Recent electrochemical experiments performed by Mark Larrousse at Clarkson University have suggested that a critical Ekman number (E) exists [48], below which a type of instability arises leading to improved mixing near the sidewall of the ampoule. The rotation rates of 80 and 300 *rpm* were chosen in order that an Ekman number above and below the critical value could be investigated.

The kinematic viscosity ν of $In_{0.2}Ga_{0.8}Sb$ was necessary to calculate the Ekman number. Jordan [49] estimated the kinematic viscosity of GaSb as a function of temperature, and this was used as an estimate since 80 mol% of the melt will be GaSb.

The ACRT cycle times chosen ($2t_E$ and $0.5t_\nu$) were recommended by Larrousse [48]. Larrousse's experiments suggest that the majority of the mixing is achieved by $0.5t_\nu$, while $2t_E$ is probably not long enough to allow adequate mixing to occur.

From the first set of experiments, the best combination of ACRT cycle time

and rotation rate will be chosen for use in the next set of experiments. This set will be a 2^3 factorial design in which the growth rate and composition will be varied along with whether or not the ACRT is employed. Table 2 depicts this experimental design.

3.3 Experimental Procedure

The correct amounts of indium, gallium, and antimony will be weighed (± 0.005 g) in order to obtain a melt with a composition corresponding to $In_{0.2}Ga_{0.8}Sb$. If necessary, the indium and antimony shot will be soaked in a mixture of $1HCl : 2H_2O$ (by volume) for 10 to 15 minutes in order to remove any oxide. This shot will then be rinsed in methanol and kept in a dessicator prior to weighing.

The ampoules will be thoroughly cleaned before introducing any charge into them. They will be soaked in Micro cleaning solution (International Products Corp., Trenton, N. J.), rinsed in deionized water, soaked in aqua regia, rinsed again in deionized water, rinsed in acetone, and then dried. The ampoules will be chilled in a refrigerator immediately before the charge is introduced. This helps to keep the gallium from melting and wetting the walls of the quartz ampoule. The gallium sticks firmly to the ampoule walls and will not flow to the bottom of the ampoule. Consequently, the stoichiometry of the melt changes. The indium, gallium, and antimony will then be dropped into the ampoule through the open end. It is important to keep the indium and gallium in separate containers before loading the ampoule since they will melt and form a solution near room temperature if kept in contact.

After the ampoule is loaded, it will be evacuated to about 5 to 10 torr and the moisture will be driven out with an oxygen-natural gas torch. The ampoule will then be backflushed twice with a mixture of 90% helium and 10% hydrogen. The ampoule will be sealed to a length of about 20 inches with the oxygen-natural gas torch.

The filled ampoule will be placed in the furnace and the cooler and furnace will

be brought to their operating temperatures. The melt will be left to homogenize in the furnace with the ACRT applied for 48 hours. The translation unit will then be turned on and the ampoule lowered at $4 \frac{\text{mm}}{\text{day}}$.

When the growth period is completed, the translation will be stopped and the furnace temperature will gradually be stepped down. The ampoule will be removed from the furnace and the ingot will be taken out by cracking the ampoule. If this method is unsuccessful, the ampoule will be dissolved from the ingot by soaking in HF overnight.

After the ampoule is removed, it will be sectioned with a diamond saw as shown in figure 15. The sections will then be cast in epoxy resin for ease of handling. The samples will be wet ground and polished with alumina particles suspended in distilled water until a smooth and shiny surface is attained. The samples will then be dipped in a small quantity of etchant to reveal the microstructure. A list of successful etchants used by Sarma [14] is given in table 3.

The longitudinally sectioned samples will be viewed under a scanning electron microscope (SEM) to determine their grain and twin boundary counts per millimeter of distance down the ingot. The energy dispersive X-ray spectrometer attachment on the SEM will be used to determine the compositional homogeneity of both the longitudinally and radially sectioned samples.

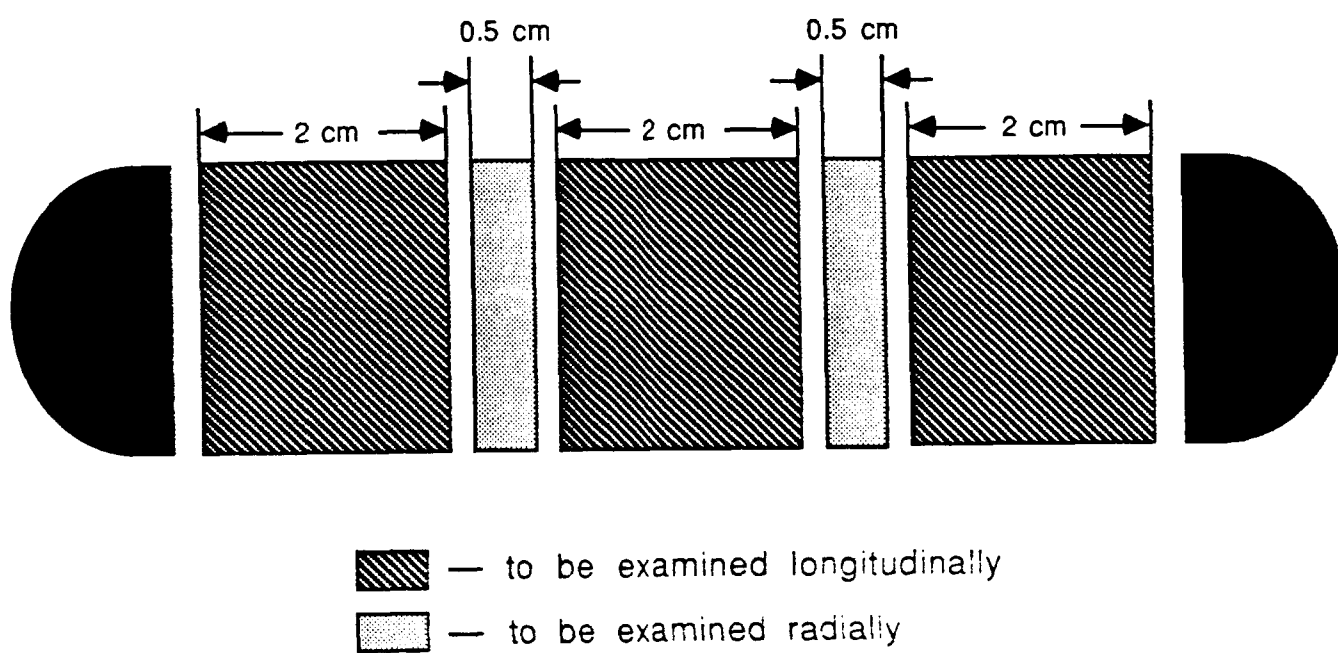


Figure 15: Sectioning of grown ingot for analysis.

Table 3: List of successful etchants [14].

ETCHANT	TIME	DESCRIPTION
$1HF : 1HNO_3 : 1H_2O$	5-10 s	Reveals the microstructure very well. Fresh etchant should be used for each sample. Lower etching times are necessary for higher InSb content alloys. Dissolution rate is approximately $3 \frac{\mu g}{mm^2 s}$.
$1HF : 2HNO_3 : 1HAc$	1-5 s	Reveals the microstructure well on higher InSb content alloys. Dissolution rate is approximately $70 \frac{\mu g}{mm^2 s}$.
$1HF : 1HNO_3 : 1HAc$	1-5 s	Reveals the microstructure well on low InSb content alloys.
$2HF : 4HNO_3 : 9H_2O$		Reveals microstructure of 50% InSb ingots but not 10% or 30% .
$2HF : 3HNO_3 : 2HAc$		Good chemical polish.

Nomenclature

- A = amplitude of the concentration variations at the interface (*mole fraction*).
 C = concentration (*mole fraction*).
 \bar{C} = dimensionless concentration.
 C_a = average concentration (*mole fraction*).
 C_i = concentration in the melt at the interface (*mole fraction*).
 C_L = concentration of the melt at position x (*mole fraction*).
 C_o = concentration of the bulk melt (*mole fraction*).
 C_p = heat capacity ($\frac{J}{g\ K}$).
 C_s = concentration of the solid at the interface (*mole fraction*).
 D = diffusivity ($\frac{cm^2}{s}$).
 D_o = diffusion pre-exponential ($\frac{cm^2}{s}$).
 E = Ekman number.
 \bullet = Rossby number.
 G = temperature gradient in the melt adjacent to the interface ($\frac{K}{cm}$).
 G_s = temperature gradient in the solid adjacent to the interface ($\frac{K}{cm}$).
 h = heat transfer coefficient ($\frac{W}{cm^2\ K}$).
 k = equilibrium distribution coefficient.
 K = thermal conductivity ($\frac{W}{cm\ K}$).
 K^L = thermal conductivity of the melt at the melting point ($\frac{W}{cm\ K}$).
 L = characteristic length scale (cm).
 m = equilibrium slope of the liquidus line ($\frac{K\ cm^3}{g}$).
 ν = kinematic viscosity ($\frac{cm^2}{s}$).
 Ω = angular rotation rate (s^{-1}).
 $\Delta\Omega$ = change in angular rotation rate (s^{-1}).

- Ω_o = initial angular rotation rate (s^{-1}).
 Ω_1 = final angular rotation rate (s^{-1}).
 Q = activation energy for diffusion ($\frac{cal}{mol}$).
 Pe^L = Peclet number for the melt.
 r = radius of ampoule (cm).
 R = gas constant ($\frac{cal}{mol K}$).
 ρ = density ($\frac{g}{cm^3}$).
 t = time (s).
 \bar{t} = dimensionless time.
 t_c = ACRT cycle time (s).
 T_c = temperature in the cooler (K).
 t_E = Ekman spin-up time (s).
 T_h = temperature in the heater (K).
 T_i = temperature at the interface (K).
 T_m = equilibrium melting temperature (K).
 t_ν = characteristic time for diffusion of momentum (s).
 V = crystal growth rate ($\frac{cm}{s}$).
 V_{cr} = crystallization flow velocity ($\frac{cm}{s}$).
 x = mole fraction of InSb in $In_xGa_{1-x}Sb$.
 x = distance into the melt from the interface (cm).
 \bar{x} = dimensionless distance into the melt from the interface.

References

- [1] J. C. McGroddy, M. R. Lorenz, and T. S. Plaskett, *Solid State Communications* 7 (1969) 901-903.
- [2] T. S. Plaskett and J. F. Woods, *J. Crystal Growth* 11 (1971) 341-344.
- [3] A. Joullie, J. Allegre, and G. Bougnot, *Mat. Res. Bull.* 7 (1972) 1101-1108.
- [4] G. B. Blom and T. S. Plaskett, *J. Electrochem. Soc.* 118 (1971) 1831.
- [5] W. A. Tiller, K. A. Jackson, J. W. Rutter, and B. Chalmers, *Acta Met.* 1 (1953) 428-437.
- [6] J. W. Rutter and B. Chalmers, *Can. J. Phys.* 31 (1953) 15-39.
- [7] W. W. Mullins and R. F. Sekerka, *J. Applied Phys.* 34 (1963) 323-329.
- [8] W. W. Mullins and R. F. Sekerka, *J. Applied Phys.* 35 (1964) 444-453.
- [9] R. F. Sekerka, *J. Applied Phys.* 36 (1965) 264-267.
- [10] W. R. Wilcox, *J. Crystal Growth* 12 (1972) 93-96.
- [11] S. Sen, *PhD thesis*, University of Southern California (1976).
- [12] H. Potts and W. R. Wilcox, *J. Crystal Growth* 74 (1986) 443-445.
- [13] J. F. Yee, M. Lin, K. Sarma, and W. R. Wilcox, *J. Crystal Growth* 30 (1975) 185-192.
- [14] K. Sarma, *PhD thesis*, University of Southern California (1976).
- [15] R. A. Lefever, W. R. Wilcox, and K. R. Sarma, *Mat. Res. Bull.* 13 (1978) 1175-1180.

- [16] J. F. Yee, S. Sen, K. Sarma, M. Lin, and W. R. Wilcox, *Proceedings - Third Space Processing Symposium - Skylab Results* **1** (1974).
- [17] S. Sen, W. R. Wilcox, and R. A. Lefever, *Metallurgical Trans.* **9A** (1978) 462-463.
- [18] J. C. Woolley and B. A. Smith, *Proc. Phys. Soc.* **72** (1958) 214-223.
- [19] J. C. Woolley, J. A. Evans, and C. M. Gillett, *Proc. Phys. Soc.* **74** (1959) 244-248.
- [20] V. I. Ivanov-Omskii and B. T. Kolomiets, *Soviet Phys. Solid State* **1** (1959) 834-838.
- [21] C. E. Chang and W. R. Wilcox, *J. Crystal Growth* **21** (1974) 135-140.
- [22] T. Fu and W. R. Wilcox, *J. Crystal Growth* **48** (1980) 416-424.
- [23] T. Jasinski and W. M. Rohsenow, *J. Crystal Growth* **61** (1983) 339-354.
- [24] R. J. Naumann and S. L. Lehoczky, *J. Crystal Growth* **61** (1983) 707-710.
- [25] A. Horowitz and Y. S. Horowitz, *Mat. Res. Bull.* **21** (1986) 1123-1129.
- [26] P. C. Sukanek, *J. Crystal Growth* **58** (1982) 208-218.
- [27] P. C. Sukanek, *J. Crystal Growth* **58** (1982) 219-228.
- [28] T. Fu and W. R. Wilcox, *J. Crystal Growth* **51** (1981) 557-567.
- [29] T. Fu and W. R. Wilcox, *J. Crystal Growth* **57** (1982) 91-93.
- [30] C. J. Chang and R. A. Brown, *J. Crystal Growth* **63** (1983) 343-364.
- [31] F. M. Carlson, A. L. Fripp, and R. K. Crouch, *J. Crystal Growth* **68** (1984) 747-756.

- [32] C. E. Huang, D. Elwell, and R. S. Feigelson, *J. Crystal Growth* 69 (1984) 275-280.
- [33] H. P. Greenspan, *The Theory of Rotating Fluids*, Cambridge at the University Press (1968).
- [34] E. R. Benton and A. Clark, Jr., *Ann. Rev. of Fluid Mech.* 6 (1974) 257-280.
- [35] E. O. Schulz-DuBois, *J. Crystal Growth* 12 (1972) 81-87.
- [36] J. M. Hyun, F. Leslie, W. W. Fowles, and A. Warn-Varnas, *J. Fluid Mech.* 127 (1983) 263-281.
- [37] P. Capper, J. J. G. Gosney, and C. L. Jones, *J. Crystal Growth* 70 (1984) 356-364.
- [38] H. J. Scheel and E. O. Schulz-DuBois, *J. Crystal Growth* 8 (1971) 304-306.
- [39] H. J. Scheel, *J. Crystal Growth* 13-14 (1972) 560-565.
- [40] A. Horowitz, D. Gazit, and J. Makovsky, *J. Crystal Growth* 61 (1983) 323-328.
- [41] J. C. Brice, P. Capper, C. L. Jones, and J. J. G. Gosney, *Prog. Crystal Growth and Charact.* 13 (1986) 197-229.
- [42] M. F. Larrousse, private communication, Clarkson University (1986).
- [43] R. T. Gray, M. F. Larrousse, and W. R. Wilcox, to be published.
- [44] D. L. Kendall, *Semiconductors and Semimetals*, 4, Academic Press Inc., New York (1968) 194.
- [45] C. S. Barrett, *Structure of Metals*, McGraw-Hill Book Company, Inc. (1952) 376-384.

- [46] E. Billig, *J. Inst. Metals* 83 (1954-1955) 53.
- [47] R. Sen and W. R. Wilcox, *J. Crystal Growth* 75 (1986) 323-328.
- [48] M. F. Larrousse, private communication, Clarkson University (1987)
- [49] A. S. Jordan, *J. Crystal Growth* 71 (1985) 551-558.

Diffusional Decay of Striations

R. T. Gray, M. F. Larrousse, and W. R. Wilcox

Department of Chemical Engineering and

Center for Advanced Materials Processing

Clarkson University, Potsdam, N.Y. 13676

August 29, 1987

Abstract

During crystal growth from melts and solutions, compositional striations in the bulk crystal parallel to the growth surface usually result from fluctuations in the growth rate and/or the flow of the growth fluid. This paper presents a one-dimensional analysis of the effect of solid-state diffusion on growth striations. A sinusoidal variation in the solid composition at the interface of a semi-infinite ingot is assumed and the damping behavior of this compositional fluctuation is followed as it moves away from the solid-liquid interface. Numerical results that include the effect of a temperature gradient in the solid are presented as well as an analytical solution that assumes that the solid is isothermal. The only parameter in the analytical solution is the dimensionless frequency $\omega = \frac{D}{V^2 t_e}$. The dimensionless distance \bar{x}_d for 99.9% decay decreases with increasing ω . The relationship between \bar{x}_d and ω has two distinct regions. For $\omega < 0.01$, the dimensional distance x_d for 99.9% decay is proportional to $\frac{V^2 t_e^2}{D}$. In this region, the striations are carried into the solid by crystal growth and damping is achieved by solid-state diffusion. For $\omega > 200$, x_d is proportional to $\sqrt{Dt_e}$. The rate of crystal growth is negligible over this range of ω and the striations are spread into the solid by diffusion. An increase in the diffusivity causes the striations to penetrate deeper into the solid and, consequently, x_d to increase. In general, the application of the ACRT to the vertical Bridgman-Stockbarger growth of concentrated solid solutions is not likely to lead to striations being frozen into the grown ingot.

1 Introduction

Compositional fluctuations parallel to the growth surface are commonly found in bulk crystals grown from melts and solutions. Most, if not all, of these striations result from fluctuations in freezing rate and/or flow of the growth fluid.

One growth technique that would be expected to give rise to striations is the accelerated crucible rotation technique (ACRT) [1,2,3,4]. It has proven to be an effective method of mixing the melt during crystal growth. For example, Capper and co-workers [5,6] showed that the application of the ACRT to the Bridgman growth of $Cd_xHg_{1-x}Te$ results in a much improved axial and radial compositional homogeneity. They did not report on the existence of striations. However, recent experiments conducted by Larrousse confirm the cyclic nature of the mixing directly above the interface [7] and lead one to expect severe striations. These observations led us to examine the possible decay of striations due to solid-state diffusion while the crystal is cooling from the growth temperature to room temperature.

2 Model Development

A model was developed by considering a volume element of differential thickness and unit area in a solidifying ingot, as shown in figure 1. A material balance around this element gives:

$$\frac{\partial}{\partial x} \left(D(x) \frac{\partial C}{\partial x} \right) - V \frac{\partial C}{\partial x} = \frac{\partial C}{\partial t}, \quad \text{where} \quad (1)$$

$$D(x) = D_o \exp \left(-\frac{Q}{R(T_m + G_s x)} \right) \quad (2)$$

- C = impurity concentration
 D_0 = diffusion pre-exponential
 $D(x)$ = diffusivity at position x
 G_s = temperature gradient in the solid
 Q = activation energy for diffusion
 R = gas constant
 t = time
 T_m = equilibrium melting temperature of solid
 V = crystal growth rate
 x = distance into ingot from the interface.

The first term in equation 1 results from the diffusion of impurity through the differential slice of solidified ingot, while the second term containing the growth velocity accounts for the movement of solid through this slice. The remaining term accounts for accumulation of impurity that occurs within the differential slice of solid. Since the diffusivity D varies exponentially with inverse temperature, it decreases rapidly with distance along the ingot. The temperature gradient in the solid G_s is assumed to be constant.

The essential assumptions in the model are:

- a one-dimensional system (i.e. a planar interface)
- a constant temperature gradient G_s
- a constant growth rate V
- a semi-infinite ingot
- a sinusoidal variation in composition at the melt-solid interface.

A one-dimensional system is not a realistic assumption since a planar interface is rarely achieved and mixing is never constant across the entire interface. However, this assumption greatly simplifies the equations, while leaving the essence of the problem intact. This model is focused on the decay of striations that are formed along the growth direction of a solidifying crystal. The assumption of a constant temperature gradient in the solid should be valid close to the interface. In reality, the temperature gradient would decrease with distance, so using a constant temperature gradient would lead to an underestimation of the diffusivity. The actual case would be somewhere between that with a constant temperature gradient and that with an isothermal solid.

Larrousse [7] determined that the variation in mixing near the interface during the ACRT is approximately sinusoidal in behavior. This led us to assume that the concentration of impurity at the interface would vary sinusoidally. Variations in heat transfer, mass transfer, and fluid flow would be expected to lead to variations in the crystal growth velocity V . For simplicity, however, the growth rate was left as a constant.

While the grown ingot is not infinitely long, if damping of the striations occurs within a short distance compared to the length of the ingot, this assumption should not affect the results. Considering the temperature gradient in the solid G_s , if the end of the ingot is at a temperature at which no diffusion occurs, then this assumption will not affect the results. The only case where assuming a semi-infinite ingot could affect the results is when damping does not occur in a short distance and the temperature of the end of the ingot is still high enough so that substantial damping can still occur.

The boundary conditions are:

C-2

$$C(0,t) = C_a + A \sin\left(\frac{2\pi t}{t_c}\right) \quad \text{and} \quad (3)$$

$$C(\infty,t) = \text{bounded}, \quad (4)$$

where t_c is the striation period, C_a is the average concentration in the solid, and A is the amplitude of the concentration variations at the interface. Equation 3 is the mathematical statement of the sinusoidal variation in impurity concentration at the interface, while equation 4 states that the concentration at a position of $x = \infty$ can not grow without bound. The initial condition is:

$$C(x,0) = C_a. \quad (5)$$

This states that the solid is initially homogeneous in concentration at a value of C_a .

The equations are non-dimensionalized as follows:

$$\bar{C} = \frac{C - C_a}{A} \quad (6)$$

$$\bar{x} = \frac{Vx}{D(0)} \quad (7)$$

$$\bar{t} = \frac{V^2 t}{D(0)}. \quad (8)$$

Bars denote dimensionless quantities. The non-dimensionalization changed equation 3 to:

$$\frac{D(\bar{x})}{D(0)} \frac{\partial^2 \bar{C}}{\partial \bar{x}^2} - \frac{\partial \bar{C}}{\partial \bar{x}} = \frac{\partial \bar{C}}{\partial \bar{t}}. \quad (9)$$

The boundary and initial conditions became:

$$\bar{C}(0,\bar{t}) = \sin\left(\frac{2\pi D(0)\bar{t}}{V^2 t_c}\right) \quad (10)$$

$$\bar{C}(\infty,\bar{t}) = \text{bounded} \quad (11)$$

$$\bar{C}(\bar{x},0) = 0. \quad (12)$$

This model was solved by an explicit finite-difference method on a Zenith Z-200 microcomputer. A forward difference approximation was used for the time derivative term and central difference approximations were used for the spatial derivative terms. The initial parameters used in the model were chosen to simulate the vertical Bridgman-Stockbarger growth of $In_xGa_{1-x}Sb$ with use of the ACRT. In subsequent runs, the value of the pre-exponential factor D_o in the diffusivity was varied along with the striation period t_c . The values for the activation energy for diffusion $Q = 12217 \frac{cal}{mol}$ and the diffusion pre-exponential $D_o = 1.2 \times 10^{-7} \frac{cm^2}{s}$ were taken from Kendall [8] and represent the diffusion of In in a $GaSb$ matrix. For all simulations, the growth rate was $4.63 \times 10^{-6} \frac{cm}{s}$. This growth rate corresponds to $4 \frac{mm}{day}$ and has been proven as an effective growth rate for the avoidance of constitutional supercooling in the $In_xGa_{1-x}Sb$ alloy system [9]. The melting temperature was taken to be $923^\circ C$. A very high temperature gradient ($G_s = -150^\circ C/cm$) was used. This reduces the rate at which striations damp, making it a conservative assumption.

In order to check the precision of the numerical solutions, an analytical solution is needed. However, the complex dependence of diffusivity on position prevents an analytical solution from being obtained. For cases where damping occurs in a short distance down the ingot, a solution using a constant diffusivity should be valid because the temperature will not decrease significantly within the region containing concentration gradients. An analytical solution for "quasi-steady state" with a constant diffusivity D is now given. ("Quasi-steady state" refers to the situation which exists after an infinite amount of time has passed. It is not truly steady state since the boundary condition at $\bar{x} = 0$ is time dependent. We will refer to this as the persistent solution.)

The equations are non-dimensionalized similarly to the variable D problem, except that the position and the time are now be scaled by the constant diffusivity D rather than the diffusivity at $x = 0$. The substitution of the new dimensionless variables into equation 1 gives:

$$\frac{\partial^2 \bar{C}}{\partial \bar{x}^2} - \frac{\partial \bar{C}}{\partial \bar{x}} = \frac{\partial \bar{C}}{\partial \bar{t}}. \quad (13)$$

The boundary conditions are:

$$\bar{C}(0, \bar{t}) = \sin(2\pi\omega\bar{t}) \quad \text{and} \quad (14)$$

$$\bar{C}(\infty, \bar{t}) = \text{bounded}. \quad (15)$$

The initial condition is:

$$\bar{C}(\bar{x}, 0) = 0. \quad (16)$$

The only parameter that affects the solution is the dimensionless frequency $\omega = \frac{D}{v^2 t_c}$.

Application of equations 14-16 to the Laplace transform of equation 13 gives:

$$\bar{C}(\bar{x}, s) = \frac{2\pi\omega}{s^2 + 4\pi^2\omega^2} \exp \left[\left(\frac{1}{2} - \sqrt{\frac{1}{4} + s} \right) \bar{x} \right]. \quad (17)$$

The Heaviside inversion technique [10] is used to bring the persistent part of the solution back into the time domain. This is the part of the solution that contains no exponentials that decay with time. The persistent solution is:

$$\begin{aligned} \bar{C}(\bar{x}, \bar{t}) = & \exp \left\{ \left(\frac{1}{2} - \left[\frac{1}{2} \left(\sqrt{\frac{1}{16} + 4\pi^2\omega^2} + \frac{1}{4} \right) \right]^{\frac{1}{2}} \right) \bar{x} \right\} \\ & \times \sin \left\{ 2\pi\omega\bar{t} - \left[\frac{1}{2} \left(\sqrt{\frac{1}{16} + 4\pi^2\omega^2} - \frac{1}{4} \right) \right]^{\frac{1}{2}} \bar{x} \right\}. \end{aligned} \quad (18)$$

3 Results and Discussion

The exponential factor in equation 18 that decays with dimensionless position \bar{x} allows one to map the dimensionless distance \bar{x}_d for 99.9% complete decay against the dimensionless frequency $\omega = \frac{D}{V^2 t_c}$. The formula for the position at which the striations decay to 0.1% of their initial amplitude is:

$$\bar{x}_d = \frac{\ln(0.001)}{\frac{1}{2} - \left[\frac{1}{2} \left(\sqrt{\frac{1}{16} + 4\pi^2 \omega^2} + \frac{1}{4} \right) \right]^{\frac{1}{2}}}. \quad (19)$$

A graph of \bar{x}_d versus ω is shown in logarithmic form in figure 2. As ω increases, the dimensionless decay distance goes down. The dimensionless group ω can be thought of as a driving force for diffusion. As the frequency of the sine wave at the interface increases, the gradients in concentration increase, leading to increased damping.

Two distinct regions of behavior can be identified. For values of $\omega < 0.01$, with an error of less than 2%, the dimensionless decay distance is given by:

$$\bar{x}_d = \frac{-\ln(0.001)}{4\pi^2 \omega^2}. \quad (20)$$

In dimensional form, the distance for 99.9% decay is:

$$x_d = \frac{-\ln(0.001) V^3 t_c^2}{4\pi^2 D}. \quad (21)$$

Thus, the decay distance x_d is directly proportional to the cube of the growth velocity V and the square of the striation period t_c . An increase in the growth rate causes the striations to be carried farther into the ingot before they can damp by diffusion. Also, an increase in the growth rate causes the striations to grow in farther apart. This reduces the concentration gradients in the ingot (the driving force for diffusion) and causes damping to occur in a much longer distance. Increasing the striation period also causes damping to occur in a longer distance by reducing the concentration gradients in the ingot. The decay distance is inversely proportional

to the diffusivity D . An increase in the diffusivity causes damping to occur more readily and, consequently, reduces x_d .

For values of $\omega > 200$, with an error of less than 2%, the dimensionless decay distance is given by:

$$\bar{x}_d = \frac{-\ln(0.001)}{\sqrt{\pi\omega}}. \quad (22)$$

The dimensional decay distance is:

$$x_d = \frac{-\ln(0.001)\sqrt{Dt_c}}{\sqrt{\pi}}. \quad (23)$$

Thus, the decay distance x_d is directly proportional to the square-root of the diffusivity D and the striation period t_c . This is quite different behavior from the case where $\omega < 0.01$. With large values of $\omega = \frac{D}{v^2 t_c}$, diffusion overwhelms convection and the second term (convective term) on the left-hand side of equation 13 can be thrown out. If this modified form of equation 13 is solved along with equations 14-16, equations 22 and 23 can be obtained directly from this result. Diffusion has a totally different role in this problem. Diffusion is the mechanism by which the impurity spreads into the ingot. Thus, the impurity can spread deeper into the ingot for a larger diffusivity.

It should be emphasized that if the dimensional position is large enough to significantly reduce the diffusivity (considering the temperature gradient in the solid), then the analytical result is invalid. On the other hand, if the dimensional position that one calculates is on the same order as the length of the ingot, then one can safely conclude that striations will be seen in the grown ingot.

Capper and co-workers achieved an 8 cm section of crystal of $Cd_xHg_{1-x}Te$ with axial and radial compositional homogeneity of $x \approx 0.21 \pm 0.002$ [5,6]. They used a growth rate of $0.5 \frac{mm}{h}$ ($1.39 \times 10^{-5} \frac{cm}{s}$) and an ACRT sequence of spin-up

for 8 s and spin-down for 1 s. The self-diffusivity of Cd in $Cd_{0.2}Hg_{0.8}Te$ at $500^\circ C$ is $4.41 \times 10^{-11} \frac{cm^2}{s}$ [11]. The freezing point of $Cd_xHg_{1-x}Te$ at a composition that would give rise to a solid of composition $x \approx 0.21$ is slightly above $670^\circ C$. With an ACRT cycle time t_c of 8 s, the above values give a dimensionless frequency of $\omega = 0.0285$. Equation 19 predicts a dimensionless position \bar{x}_d for 99.9% decay of 247. This corresponds to a distance of only $7.84 \mu m$ from the freezing interface. Thus, damping of the striations induced by the ACRT should occur almost immediately in this case, explaining why striations apparently were not observed [5,6].

The results of the numerical and analytical modeling are compared in figures 3-8. The solid lines represent the analytical solution and the squares represent the numerical data. Overall, the numerical results agree quite well with the analytical solution. However, for cases where the dimensionless frequency ω is low and damping occurs slowly, the numerical calculations do not predict the damping behavior well, as evident in figure 8. This is because the finite difference approximations to the spatial derivatives are not adequate at the points where the slope is changing the most. This occurs at the peaks of the striations. Figures 3-8 were compiled by first obtaining the numerical results for a specific combination of diffusion pre-exponential D_0 and striation period t_c while holding the values of G_s , Q , T_m , and V constant at the values already specified. The analytical results were then computed for values of ω and \bar{t} corresponding to the situation for which the numerical results were obtained. Any discrepancy between the analytical and numerical results for concentration at $\bar{x} = 0$ (e.g. figure 4) is due to a slight mismatch in the values of \bar{t} used in each case.

The numerical results in figure 3 are for $D_0 = 1.2 \times 10^{-7} \frac{cm^2}{s}$ and $t_c = 60 s$. These values closely approximate those being used to grow $In_xGa_{1-x}Sb$ by the vertical Bridgman-Stockbarger technique at Clarkson University. The dimensional

time t of the simulation was 450 s. In this time, 7.5 full striations grow in. The figure shows that all of these striations do not remain, i.e. complete damping occurs. The extremely broad peak at the extreme right of the figure is the “start-up” peak. This peak is slow to decay because it suffers from a lack of driving force on its right-hand side. Every other peak has a negative peak on either side of it, while this peak does not have a negative peak on its right since it is the first to grow in. The start-up peak does not appear in the analytical solution because the analytical solution is only the persistent part of the total solution. This is the reason for the difference between the analytical and numerical results at the right side of the figure. The dimensionless wavelength at which the striations grow in in figure 3 is $\frac{1}{\omega}$ or about 8.4 dimensionless units. Thus, we can see that the striations have spread out upon damping. Complete (99.9%) damping occurs in a dimensionless distance of 31.3 in figure 3. This corresponds to a position of only 10.4 μm for the values of the parameters used in calculating the numerical solution.

The value of t_c is reduced to 6 s and D_0 remains at $1.2 \times 10^{-7} \frac{cm^2}{s}$ for the numerical results in figure 4. In the 20.1 s simulated time period, 3.4 full striations grow in. Again we see that complete damping occurs. The initial wavelength of the striations in this case is 0.84. Note that the striations have spread to a wavelength of about 3.2. The start-up peak effect gives rise to the discrepancy between the analytical and numerical results since, at this early time, the first peak has not propagated far into the ingot. Complete damping occurs at $\bar{x}_d = 4.71$. This corresponds to 1.56 μm for the parameters used in the numerical solution. This is a shorter distance than it takes for complete damping to occur when the striation period is ten times larger. For a given growth rate, a shorter cycle time causes the striations to grow in closer together. This increases the driving force for diffusion (concentration gradients) in the solid.

The numerical results in figure 5 are for an increased t_c of 100 s with D_o remaining $1.2 \times 10^{-7} \frac{cm^2}{s}$. As expected because of the above argument, increasing the striation period causes complete damping to require a longer distance (19.4 μm). The original dimensionless wavelength of the striations for this case is 14. Considerably less spreading of the striations occurs and more cycles remain before damping. The simulated time is 1000 s so that 10 full striations have grown in and 3 remain.

Figure 6 is for D_o increased by a factor of ten to $1.2 \times 10^{-6} \frac{cm^2}{s}$ and t_c returned to 60 s in the numerical solution. After 450 s only about 1.5 out of 7.5 full striations remain and they have spread out to a large extent. Complete damping occurs at a position of 15.6 μm , a longer distance than it takes for damping to occur in figure 3 where D_o is ten times smaller. Complete damping takes longer for a larger D_o , exactly opposite from what intuition would lead one to believe. The value of ω is 0.119 in figure 3 and is 1.19 in figure 6. These numbers fall in the intermediate region between the two limiting behaviors of x_d described by equations 21 and 23. However, a close examination of figure 2 reveals that these values of ω are in a region that more closely follows the limiting case of $\omega > 200$ than the limiting case of $\omega < 0.01$. Equation 23 predicts that x_d should increase with the \sqrt{D} as explained in the beginning of this section.

Figure 7 is for a D_o of $1.2 \times 10^{-8} \frac{cm^2}{s}$ with t_c remaining at 60 s. After 313 s each of the 5.2 striations that have grown in remain. The start-up peak at the far right of the figure is the only significant deviation between the analytical and numerical results. From the figure, one can not notice any spreading of the striations. Although the position where complete damping occurs does not appear on figure 7, it was determined from the analytical solution to be 42.1 μm . The diffusivity only decreases by 0.46% in this distance. Therefore, the analytical solution should provide a realistic result.

In figure 8, the diffusion pre-exponential is reduced by another factor of ten to $1.2 \times 10^{-9} \frac{\text{cm}^2}{\text{s}}$ and the striation period is left at 60 s. Damping occurs slowly for this case and no spreading of the striations from their original wavelength of 840 dimensionless units can be seen. The analytical solution gives 410 μm for the value of the complete decay distance. The diffusivity decreases by 4.4% in this distance so the analytical solution should provide a complete decay distance that is very close to the actual value. A decrease in diffusivity by a factor of ten below the value used in figure 7 causes complete damping to take longer. This is expected since the values of ω in these two graphs fall into the region where the behavior of x_d can be explained quite well by equation 21. The numerical solution is completely inadequate in providing a good estimate of the decay distance in this case. With the low diffusivity, the solid can support large concentration gradients at great depths in the ingot. These large gradients require extremely small step sizes for calculating the finite difference approximations accurately at their peaks. The error at the peaks builds up as one goes deeper into the ingot because each successive time step is calculated from the one directly preceding it and extremely long times must be simulated to get striations which penetrate deeply into the solid.

The difference between the analytical and numerical results in figures 3-8 was not attributed to the lack of a temperature gradient in the solid. The maximum position shown on any of the figures is 17 μm . The diffusivity only decreases by 0.18% in this distance, therefore, the analytical solution represents an accurate picture of the striation damping behavior. Increasing the value of the temperature gradient in the solid G_s , or the activation energy for diffusion Q would increase the difference between the analytical and numerical results.

4 Conclusions

The amount of damping of striations that are solidified into a growing ingot is determined primarily by one dimensionless group, $\omega = \frac{D}{V^2 t_c}$. The larger the value of ω , the shorter the dimensionless distance that complete damping will occur in. The dimensional decay distance x_d is described for values of $\omega < 0.01$, with an error of less than 2%, by equation 21. This shows that $x_d \propto \frac{V^3 t_c^2}{D}$. For this range of ω , the striations are carried into the solid by crystal growth at velocity V and are damped by solid-state diffusion. Equation 23 describes the behavior of x_d for values of $\omega > 200$ with an error of less than 2%. This shows that $x_d \propto \sqrt{D t_c}$. For this range of ω , the growth rate is negligible (there is no dependence of x_d on V) and the striations are carried into the solid by diffusion only. A larger diffusivity allows the striations to penetrate a greater depth into the solid. Thus, two distinct regions exist that possess totally different mechanisms for the decay of striations. In both regions an increase in the striation period causes decay to take longer. When $\omega < 0.01$, increasing the striation period hinders decay by causing the striations to grow in farther apart, consequently, reducing the concentration gradients in the solid (i.e. the driving force for diffusion). For $\omega > 200$, the mechanism by which the striation period affects the decay distance changes. Increasing the striation period increases the amount of time that the interface concentration is above the average impurity concentration in the solid C_a before going below. This gives the diffusivity a longer time to spread the striation into the solid before the concentration at the interface begins to decrease and fall below C_a .

In general, the application of the ACRT to the vertical Bridgman-Stockbarger growth of concentrated solid solutions is not likely to lead to striations being frozen into the grown ingot. The low growth rates necessary to avoid constitutional su-

percooling in alloy systems help promote the decay of striations in two ways. First, a low growth rate causes the grown-in striations to remain at temperatures near the melting point for long periods of time. The diffusivity of the solute is greater at these higher temperatures and this promotes decay for low values of ω (i.e. where damping of striations is more difficult). Second, at lower growth rates the striations grow in closer together for a fixed striation period. This increases the concentration gradients in the solid and promotes decay for low values of ω . If ω is high, the growth rate has no effect, but damping occurs quickly in this case anyway.

5 Acknowledgements

The authors wish to thank NASA for their support of this work under grants NAG8-480 and NAG8-541.

References

- [1] H. J. Scheel and E. O. Schulz-DuBois, *J. Crystal Growth* 8 (1971) 304-306.
- [2] E. O. Schulz-DuBois, *J. Crystal Growth* 12 (1972) 81-87.
- [3] H. J. Scheel, *J. Crystal Growth* 13-14 (1972) 560-565.
- [4] J. C. Brice, P. Capper, C. L. Jones, and J. J. G. Gosney, *Prog. Crystal Growth and Charact.* 13 (1986) 197-229.
- [5] P. Capper, J. J. G. Gosney, and C. L. Jones, *J. Crystal Growth* 70 (1984) 356-364.
- [6] P. Capper, J. J. Gosney, C. L. Jones, and I. Kenworthy, *J. Electronic Materials* 15 (1986) 371-375.
- [7] M. F. Larrousse, *PhD thesis*, Clarkson University (1987).
- [8] D. L. Kendall, *Semiconductors and Semimetals*, 4, Academic Press Inc., New York (1968) 194.
- [9] S. Sen, *PhD thesis*, University of Southern California (1976).
- [10] D. L. Powers, *Boundary Value Problems*, 2nd Ed., Academic Press, New York (1979) 254-261.
- [11] D. Shaw, *Phil. Magn. A*, 53 (1986) 727-737.

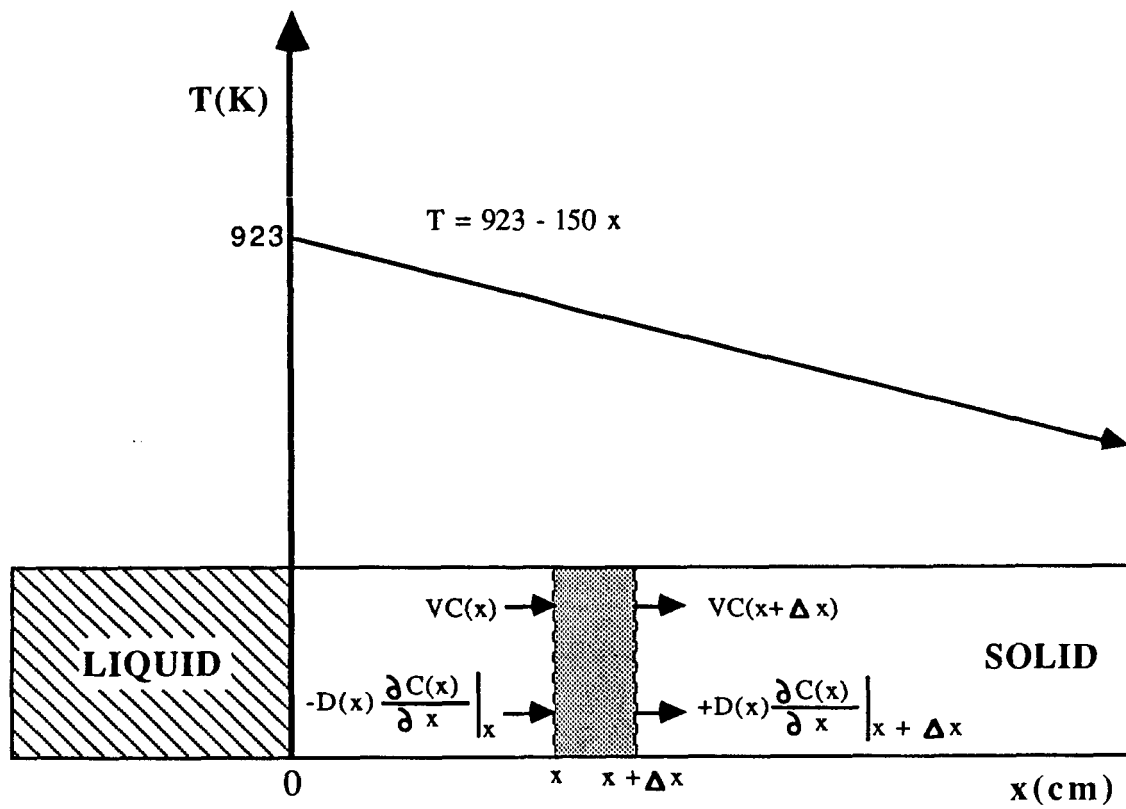


Figure 1. Differential slice of solidified ingot used in the model development.

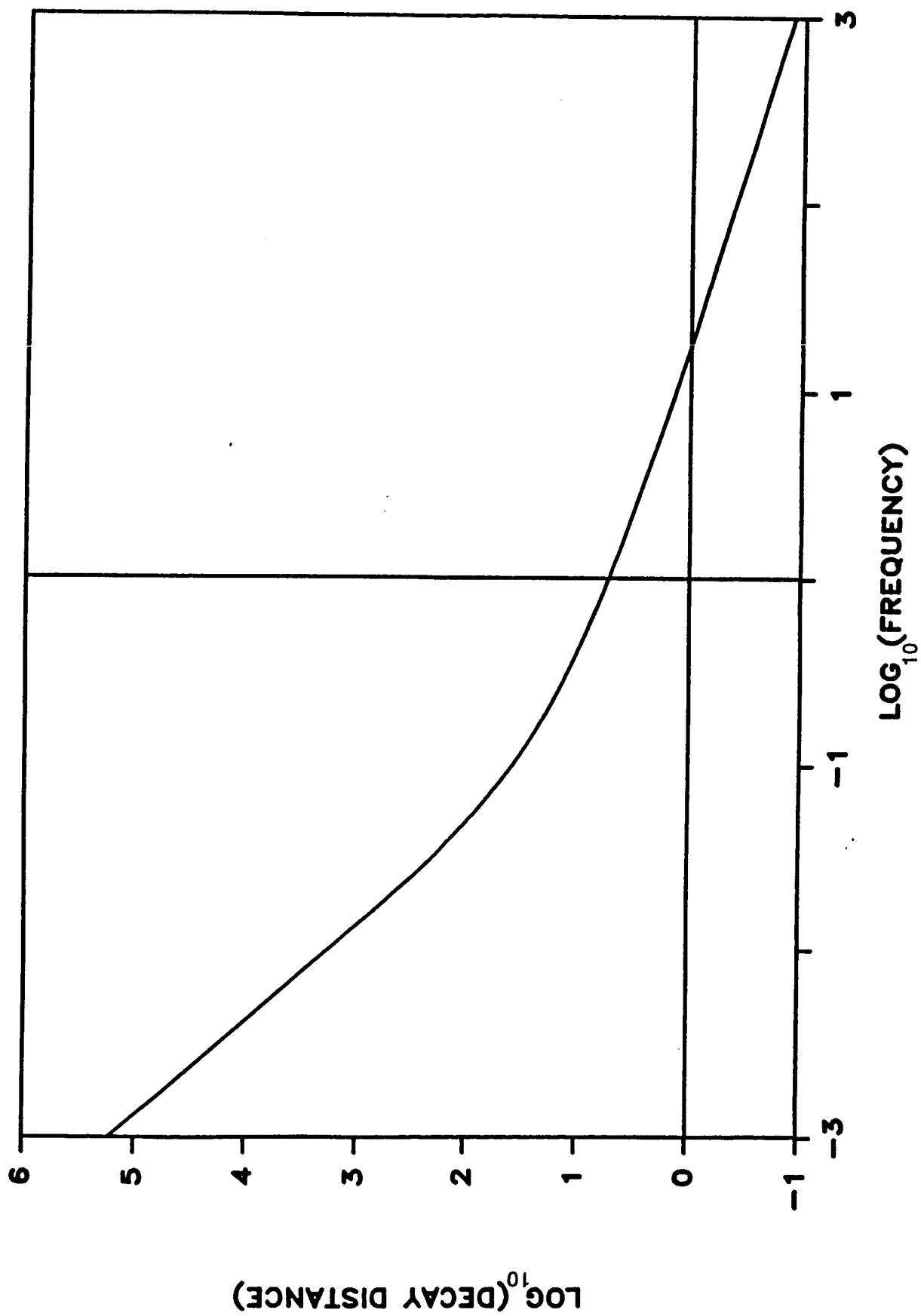


Figure 2. Dimensionless position for 99.9% decay \bar{x}_d vs. the dimensionless frequency ω (Equation 19).

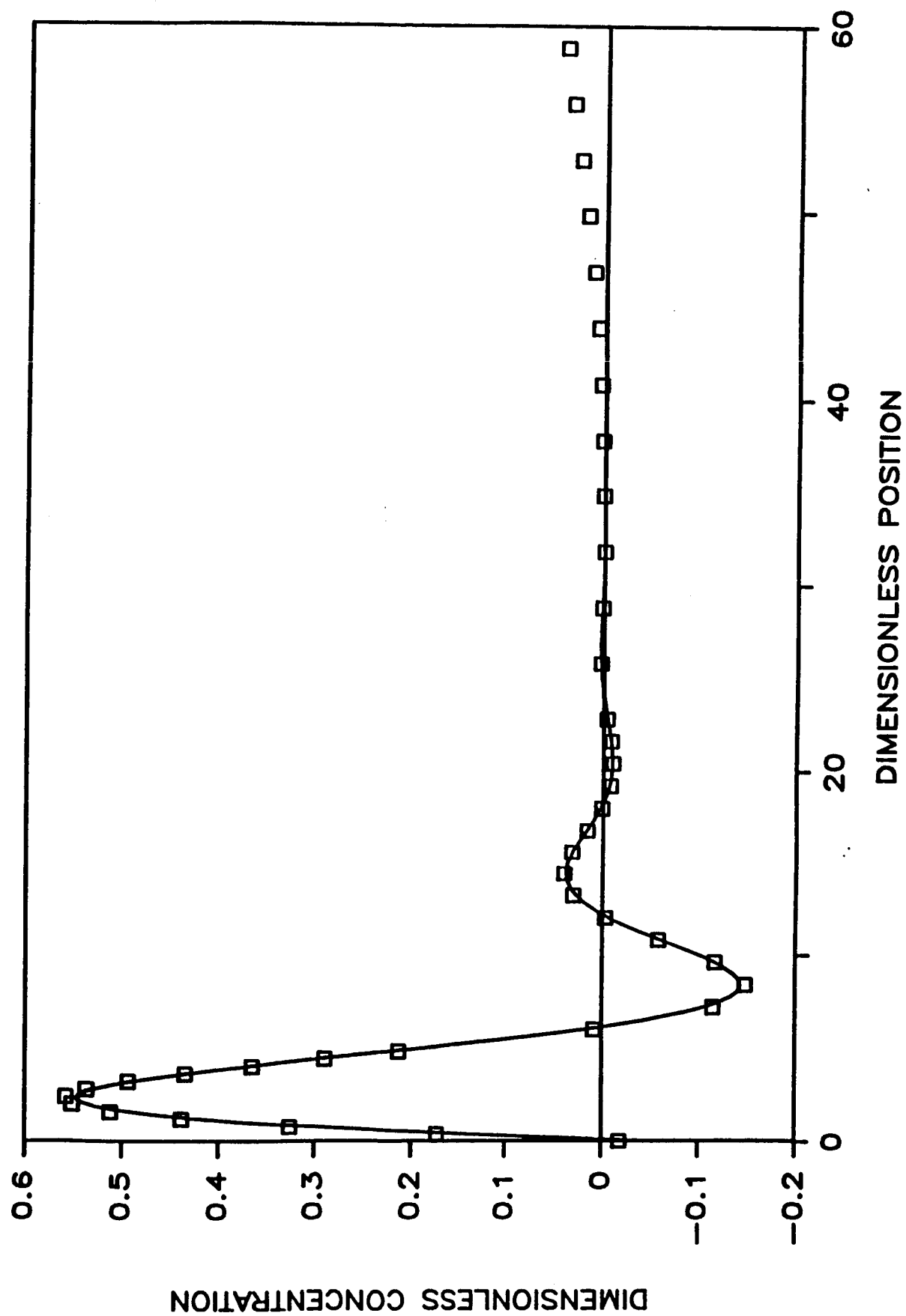


Figure 3. Striation damping (\square = numerical results for $D_o = 1.2 \times 10^{-7} \frac{cm^2}{s}$ and $t_c = 60 s$, — = analytical solution for $\omega = 0.119$).

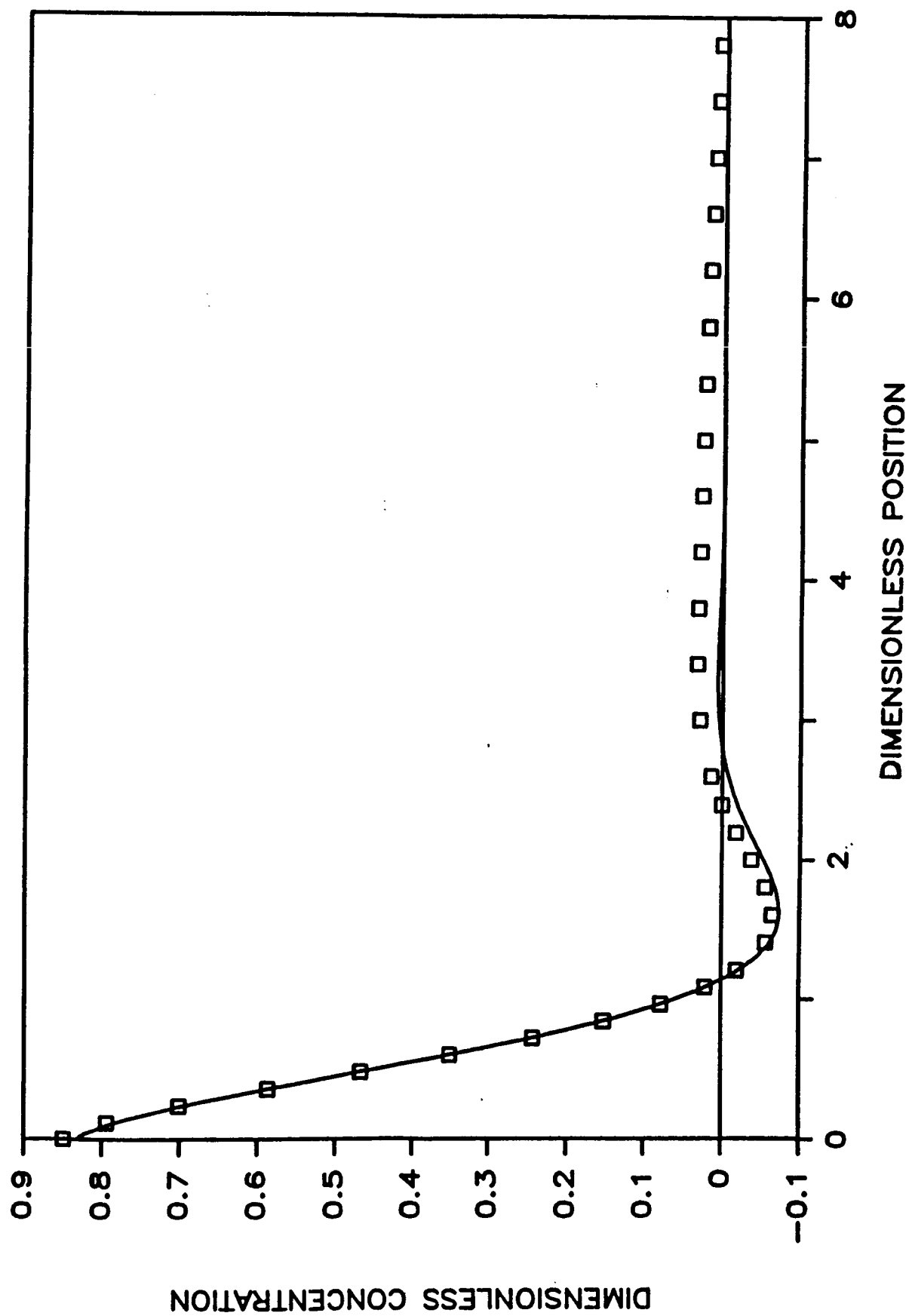


Figure 4. Striation damping (\square = numerical results for $D_o = 1.2 \times 10^{-7} \frac{cm^2}{s}$ and $t_c = 6 s$, — = analytical solution for $\omega = 1.19$).

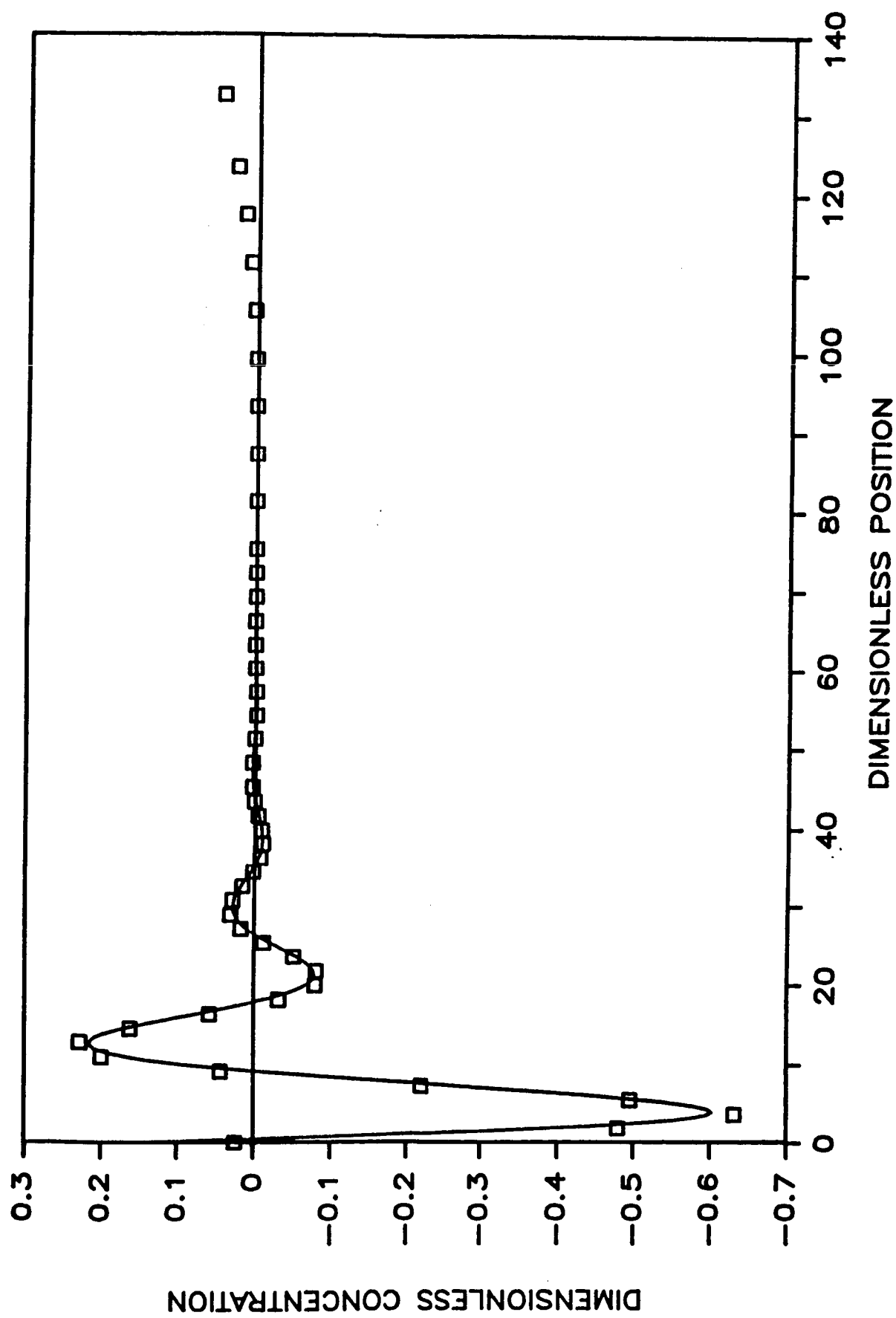


Figure 5. Striation damping (\square = numerical results for $D_o = 1.2 \times 10^{-7} \frac{cm^2}{s}$ and $t_c = 100 s$, — = analytical solution for $\omega = 0.0714$).

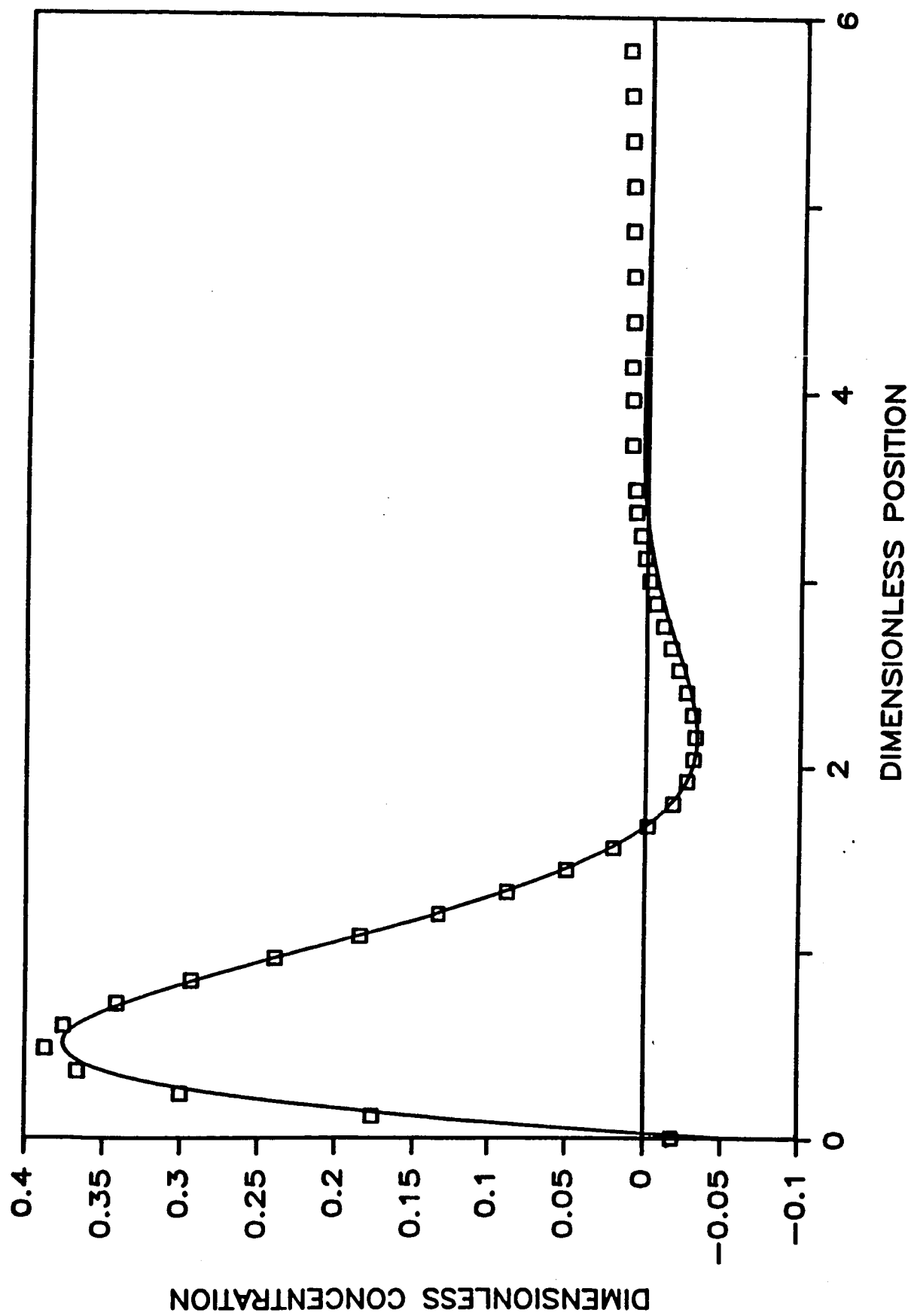


Figure 6. Striation damping (\square = numerical results for $D_o = 1.2 \times 10^{-6} \frac{cm^2}{s}$ and $t_c = 60 s$, — = analytical solution for $\omega = 1.19$).

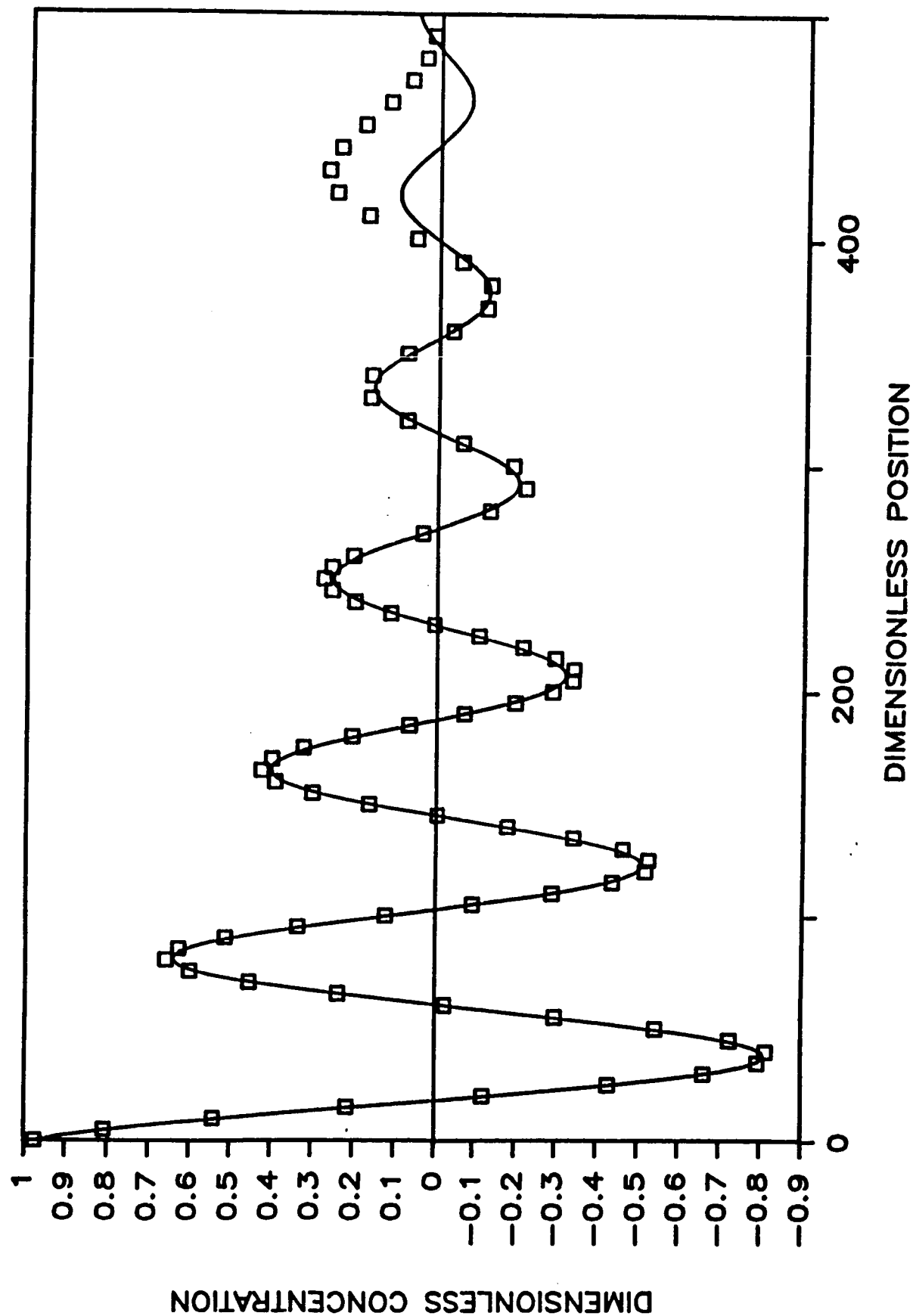


Figure 7. Striation damping (□ = numerical results for $D_0 = 1.2 \times 10^{-8} \frac{cm^2}{s}$ and $t_c = 60 s$, — = analytical solution for $\omega = 0.0119$).

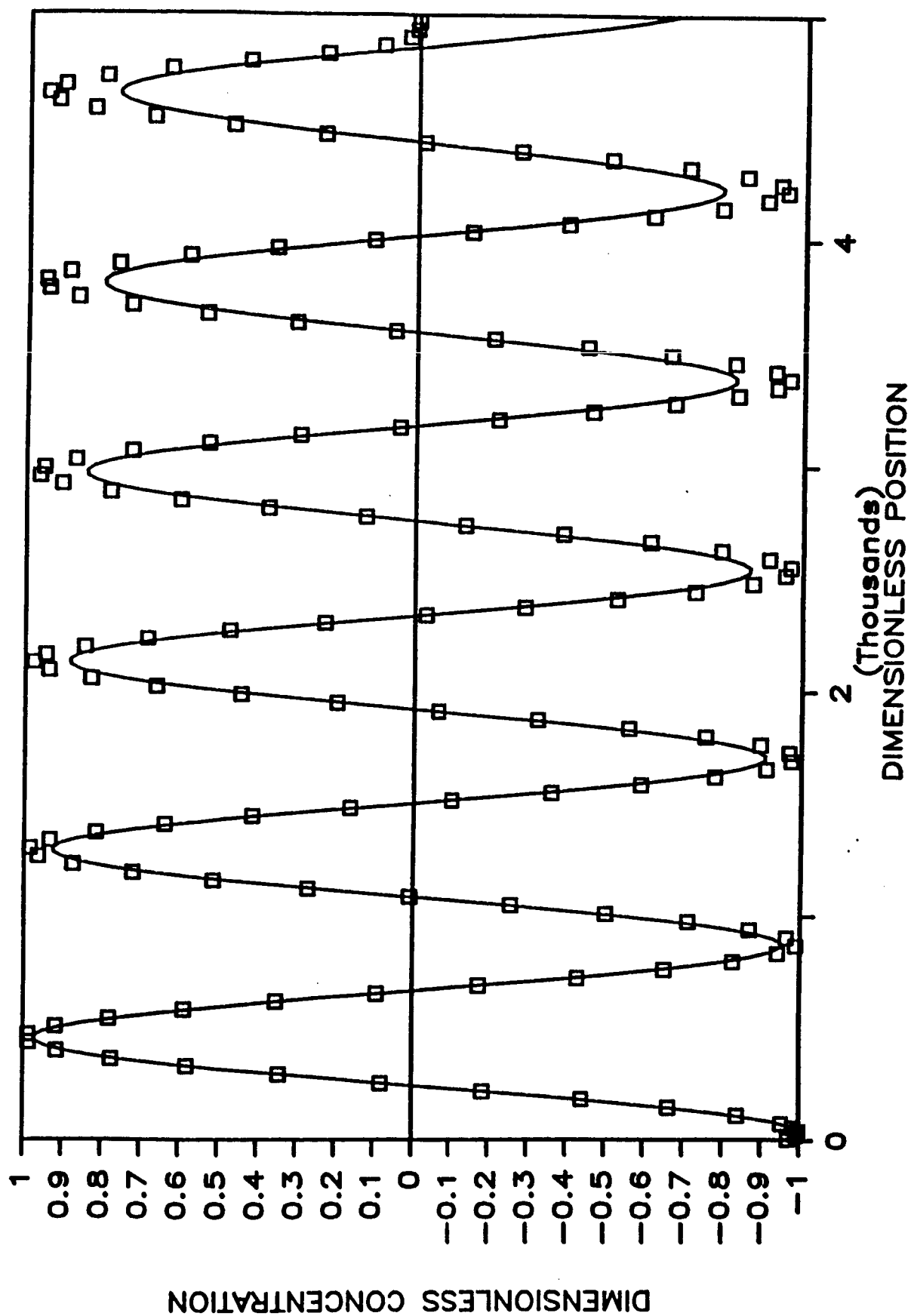


Figure 8. Striation damping (\square = numerical results for $D_o = 1.2 \times 10^{-9} \frac{\text{cm}^2}{\text{s}}$ and $t_c = 60 \text{ s}$, — = analytical solution for $\omega = 0.00119$).